



JOHANNES GUTENBERG  
UNIVERSITÄT MAINZ

# **Computer simulations of active Brownian particles**

Dissertation

zur Erlangung des Grades

„Doktor der Naturwissenschaften“

am Fachbereich Physik, Mathematik und Informatik  
der Johannes Gutenberg-Universität in Mainz

vorgelegt von

**Jonathan Tammo Siebert**

geboren am 19.04.1991

in Bad Nauheim

Mainz, den 26. Juni 2018

**Jonathan Tammo Siebert**

*Computer simulations of active Brownian particles*

Submitted: June 26, 2018

Oral examination: November 6, 2018

**Johannes Gutenberg-Universität Mainz**

Institut für Physik

Staudingerweg 7

55128 Mainz

# Abstract

In recent years, active particles have received significant attention. Their defining property to convert (free) energy into some form of directed motion inherently drives them out of equilibrium. For interacting particles, this driving leads to a variety of collective behaviors. Active Brownian particles are a simplified model system that allows to study such collective behavior by numerical simulation or analytic theory. They extend the overdamped dynamics of nearly hard disks by introducing an additional self-propulsion velocity. At sufficient propulsion strength, active Brownian particles show a motility induced phase separation, a phenomenon known from other active systems in both experiment and theory. This phase separation closely resembles a gas-liquid transition in equilibrium, which raises the question how far concepts of equilibrium statistical physics and thermodynamics can be applied to this system far from equilibrium.

In this thesis, we study said analogy by employing large-scale computer simulations. Through the application of methods known from equilibrium physics, we extract precise, finite-size independent estimates for the phase boundaries. Furthermore, we examine the influence that other parameters, namely anisotropic particle shapes and the dimensionality of the system, have on the position of the phase boundaries, also known as binodal lines. Additionally, we study a proposed definition of an active pressure, that extends the concept of pressure for active Brownian particles. We verify the thermodynamical intensiveness of this active pressure, supporting its validity. Nonetheless, we also find limits for the analogy to equilibrium physics, as the resulting interfacial tension in the phase separated state turns out to be negative. Finally, the main part of the thesis is dedicated to finding the position of the critical point using a subsystem distribution method. By improving this scheme known from equilibrium, we determine the critical point to be at  $Pe_{cr} = 40(2)$  and  $\phi_{cr} = 0.597(3)$ . Based on this estimate for the position of the critical point, we find critical exponents by studying different scaling laws close to the critical point. The extracted exponents  $\beta$ ,  $\gamma$ , and  $\nu$  indicate that active Brownian particles do not follow 2D Ising universality, thus raising the question of the existence of an active universality class far from equilibrium.

# Zusammenfassung

Aktive Teilchen haben in den letzten Jahren erhebliche Aufmerksamkeit erregt. Sie sind über ihre Fähigkeit definiert, (freie) Energie in eine gerichtete Bewegung umzuwandeln. Dadurch werden sie zwangsläufig aus dem Gleichgewicht getrieben. Interagierende Teilchen zeigen hierbei eine Vielfalt kollektiven Verhaltens. Aktive Brownsche Teilchen sind ein vereinfachtes Modellsystem, welches die Untersuchung solchen kollektiven Verhaltens mit Hilfe von Computersimulationen oder analytischer Theorie ermöglicht. Übersteigt ihr Vortrieb eine gewisse Stärke, separieren sie in zwei Phasen. Ein ähnliches Verhalten ist sowohl im Experiment als auch in der Theorie bei anderen aktiven Systemen ebenfalls beobachtet worden. Die Phasenseparation ähnelt stark dem bekannten Gleichgewichtsphasenübergang von Gas zu Flüssigkeit. Dies wirft die Frage auf, inwiefern Konzepte der Gleichgewichtsphysik auf das System der aktiven Brownschen Teilchen angewandt werden können.

Im Rahmen dieser Arbeit wird diese Frage mit Hilfe großangelegter Computersimulationen untersucht. Aus der Gleichgewichtsphysik bekannte Methoden werden angewandt um präzise und von der endlichen Systemgröße unabhängige Abschätzungen der Phasengrenzkurven zu bestimmen. Darüber hinaus wird auch der Einfluss anderer Systemparameter untersucht, indem anisotrope Teilchen sowie Systeme mit anderer Dimensionalität simuliert werden. Anschließend wird eine Druckdefinition für aktive Teilchen, die in den letzten Jahren vorgeschlagen wurde, getestet. Durch Untersuchung eines phasenseparierten Systems wird die thermodynamische Intensivität dieser Definition verifiziert. Es werden jedoch auch die Grenzen der Analogie zum Gleichgewicht aufgezeigt, da die aus dieser Druckdefinition resultierende Oberflächenspannung negativ ist. Im letzten und größten Teil der Arbeit wird die Position des kritischen Punktes bestimmt. Hierzu wird eine erweiterte Version der Subsystem-Verteilungsmethode, die auch im Gleichgewicht angewandt wird, verwendet. Das Ergebnis für die Position des kritischen Punktes ist  $Pe_{cr} = 40(2)$  und  $\phi_{cr} = 0.597(3)$ . Auf Basis dieser Abschätzung werden kritische Exponenten bestimmt, indem Skalierungsverhalten in der Nähe des kritischen Punktes untersucht werden. Anhand der Resultate für die Exponenten  $\beta$ ,  $\gamma$  und  $\nu$  wird gezeigt, dass aktive Brownsche Teilchen nicht in die Universalitätsklasse des zweidimensionalen Isingmodells fallen. Dies wirft die Frage auf, ob es eine aktive Universalitätsklasse fernab des Gleichgewichts gibt.



# Contents

<b>1</b>	<b>Introduction</b>	<b>1</b>
<b>2</b>	<b>Theoretical background</b>	<b>7</b>
2.1	Brownian dynamics simulations . . . . .	7
2.1.1	Langevin equation . . . . .	7
2.1.2	Overdamped limit . . . . .	8
2.1.3	Rotational diffusion . . . . .	9
2.1.4	Numerical integration . . . . .	9
2.1.5	Unit system . . . . .	10
2.2	Phase transitions . . . . .	10
2.2.1	The gas-liquid transition . . . . .	11
2.2.2	Order parameter . . . . .	12
2.2.3	Classification of phase transitions . . . . .	13
2.2.4	Scaling laws and universality . . . . .	13
2.3	Finite size scaling . . . . .	16
2.3.1	Binder cumulant . . . . .	17
2.4	Software . . . . .	19
<b>3</b>	<b>Active Brownian particles</b>	<b>21</b>
3.1	Equation of motion for active Brownian particles . . . . .	21
3.2	Effect of the propulsion . . . . .	21
3.3	Self-trapping and motility induced phase separation . . . . .	23
3.4	Interaction potential and effective diameter . . . . .	26
3.5	Numerical integration . . . . .	28
3.5.1	Euler . . . . .	28
3.5.2	Predictor-corrector method . . . . .	28
<b>4</b>	<b>Phase behavior in two dimensions</b>	<b>31</b>
4.1	Finite size transitions . . . . .	31
4.2	Determination of binodal densities . . . . .	32
4.3	Rectilinear diameter . . . . .	35
<b>5</b>	<b>Pressure and interfacial tension</b>	<b>37</b>
5.1	Definition of an active pressure . . . . .	37
5.2	Simulations . . . . .	40

5.3	Interfacial tension . . . . .	43
<b>6</b>	<b>Influence of shape and dimensionality on the phase behavior</b>	<b>45</b>
6.1	Active Brownian dimers . . . . .	45
6.1.1	Dimer models . . . . .	46
6.1.2	Phase diagram . . . . .	47
6.1.3	Mapping onto active disks . . . . .	48
6.2	Active Brownian spheres in three dimensions . . . . .	52
6.2.1	Phase diagram . . . . .	52
<b>7</b>	<b>Determination of the critical point using the original subsystem distribution method</b>	<b>55</b>
7.1	Original subsystem distribution method . . . . .	55
7.2	Results along constant density . . . . .	59
7.3	Locus of maximum $Q_\ell$ . . . . .	63
7.4	Results along the locus $Q_{\ell,\max}$ . . . . .	65
7.5	Problems of the original subsystem distribution method . . . . .	69
<b>8</b>	<b>Improving the subsystem distribution method</b>	<b>73</b>
8.1	Idea of the improved subsystem distribution method . . . . .	73
8.2	Test on the 2D Ising model . . . . .	75
8.3	Test on the 2D Lennard-Jones model . . . . .	76
8.4	Determination of the critical point in active Brownian particles (ABPs)	78
8.5	Alternative bounds on the critical point . . . . .	86
8.5.1	Cluster size distribution . . . . .	86
8.5.2	Static structure factor . . . . .	87
<b>9</b>	<b>Critical exponents</b>	<b>93</b>
9.1	Order parameter exponent $\beta$ . . . . .	93
9.2	Correlation length exponent $\nu$ . . . . .	96
9.3	Another quotient of critical exponents $\gamma/\nu$ . . . . .	98
9.4	Consistency checks and outlook . . . . .	99
<b>10</b>	<b>Conclusion and outlook</b>	<b>101</b>
	<b>Appendix A Additional Material</b>	<b>103</b>
A.1	Supplementary Figures . . . . .	103
A.2	Static structure factor and correlation length . . . . .	105
	<b>Bibliography</b>	<b>109</b>

# List of Publications

This thesis is in parts a recapitulation of ideas published in the following articles by the author during the course of the PhD program:

- [11] J. Bialké, **J. T. Siebert**, H. Löwen, and T. Speck. “Negative Interfacial Tension in Phase-Separated Active Brownian Particles”. In: *Physical Review Letters* 115, 098301 (2015).

*Author contributions:* The article was written mainly by T. Speck and J. Bialké. Following preliminary studies by J. Bialké, the presented results for the pressure distribution and the interfacial tension were produced and analyzed by the author. The numerical results for the phase diagram were obtained by J. Bialké and the author independently. Determination of interfacial widths was done by J. Bialké. All authors worked on the interpretation of the results. The outline of the paper was conceived by T. Speck, H. Löwen, and J. Bialké.

- [121] **J. T. Siebert**, J. Letz, T. Speck, and P. Virnau. “Phase behavior of active Brownian disks, spheres, and dimers”. In: *Soft Matter* 13, 1020–1026 (2017).

*Author contributions:* The article was written mainly by the author with input from P. Virnau and T. Speck. Simulations of the monomeric particles were performed by the author. The corresponding simulations for dimeric systems were done by J. Letz under the supervision of P. Virnau and the author. The corresponding simulation routines were implemented by the author. The mapping theory was developed by the author in coordination with T. Speck. The general outline was conceived by P. Virnau with input by the author.

- [143] B. Trefz, **J. T. Siebert**, T. Speck, K. Binder, and P. Virnau. “Estimation of the critical behavior in an active colloidal system with Vicsek-like interactions”. In: *The Journal of Chemical Physics* 146, 074901 (2017).

*Author contributions:* The article was written by B. Trefz with input from all authors. The numerical results, as well as their analysis, and the corresponding figures were produced by B. Trefz with small contributions by the author. The general outline of the study was conceived by P. Virnau with input from all authors.

- [120] **J. T. Siebert**, F. Dittrich, F. Schmid, K. Binder, T. Speck, and P. Virnau. “Critical behavior of active Brownian particles”. In: *Physical Review E* 98, 030601(R) (2018).

*Author contributions:* The article was written by the author and T. Speck with input by the other authors. The qualitative justification in the SI was provided by K. Binder. The improved subsystem method was developed for the Ising model by F. Dittrich under the supervision of P. Virnau and F. Schmid. The application to the Lennard-Jones fluid and active Brownian particles were done by the author. The results on critical exponents and of the original subsystem method were also produced and analyzed by the author. The general outline of the study was conceived by P. Virnau with input by K. Binder and the author.

Additionally, the following articles of the author that are unrelated to the content of this thesis have been published during the PhD program:

- D. Richard, S. Stalter, **J. T. Siebert**, F. Rieger, B. Trefz, and P. Virnau. “Entropic Interactions between Two Knots on a Semiflexible Polymer”. In: *Polymers*, 9, 55 (2017).

*Author contributions:* D. Richard performed and analyzed the simulations of the confined chains and S. Stalter of the free chains. The author, B. Trefz and F. Rieger wrote analysis tools and contributed to the knot analysis. F. Rieger wrote the Monte Carlo code, P. Virnau and F. Rieger wrote the knot detection code. The author, D. Richard, and P. Virnau wrote the paper. P. Virnau conceived the study.

- **J. T. Siebert**, A. N. Kivel, L. P. Atkinson, T. J. Stevens, E. D. Laue, and P. Virnau. “Are There Knots in Chromosomes?”. In: *Polymers*, 9, 317 (2017).

*Author contributions:* P. Virnau wrote the knot analysis code and suggested the project. T. J. Stevens, L. P. Atkinson, and E. D. Laue performed the original experiments, structural analysis and provided additional structures for knot analysis. The author performed the knot analysis. A. N. Kivel performed the knot stability analysis and wrote the corresponding code. All authors were

involved in the discussion of results. The author, E. D. Laue, and P. Virnau wrote the paper.

- J. I. Sulkowska, S. Niewieczeral, A. I. Jarmolinska, **J. T. Siebert**, P. Virnau, and W. Niemyska. “KnotGenome: A server to analyze entanglements of chromosomes”. In: *Nucleic Acids Research*, gky511 (2018)

*Author contributions:* The author contributed mostly by extensive revision of the article and the information provided on the web page, as well as by testing the server. Additionally, minor data conversion tools were provided by the author.

Prior to the PhD program, the following publication of the author was published:

- B. Trefz, **J. Siebert**, and P. Virnau. “How molecular knots can pass through each other”. In: *Proceedings of the National Academy of Sciences*, 111, 7948-7951 (2014).



# List of Figures

2.1	Sketch of a simple phase diagram . . . . .	11
2.2	Sketch of a cumulant intersection . . . . .	19
3.1	Exemplary trajectories showing the influence of propulsion . . . . .	22
3.2	Sketch of the mechanism behind cluster formation in ABPs . . . . .	24
3.3	Polarization of ABPs at an interface . . . . .	25
3.4	WCA potential . . . . .	27
4.1	Snapshots of finite size transitions . . . . .	33
4.2	Packing fraction distribution in a slab geometry . . . . .	34
4.3	Phase diagram of ABPs in 2D . . . . .	35
5.1	Distribution of the virial pressure . . . . .	38
5.2	Distributions of pressure components perpendicular to a slab . . . . .	41
5.3	Distribution of the total pressure in a phase separated state . . . . .	43
6.1	Sketch of the dimer models . . . . .	46
6.2	Phase diagram of active Brownian dimers . . . . .	47
6.3	Phase diagram mapping of dimers onto monomers . . . . .	49
6.4	Phase diagram of active Brownian spheres (3D) . . . . .	52
7.1	Sketch of the system geometry used in the original subsystem distribution method . . . . .	56
7.2	Pe-Evolution of the packing fraction probability distribution for different $\ell$	57
7.3	Infinite system size limit $Q_\infty(\bar{\phi})$ in the two phase region [66] . . . . .	60
7.4	Illustration of $Q_\ell(\text{Pe} \approx 39.85)$ 's dependence on $\bar{\phi}$ . . . . .	61
7.5	$Q_\ell$ vs. Pe for a large system along a constant density locus . . . . .	62
7.6	Illustration of $Q_\ell(\text{Pe} \approx 33.21)$ 's dependence on $\bar{\phi}$ . . . . .	64
7.7	Course of the locus of maximum $Q_\ell$ for different subsystem sizes . . .	65
7.8	Course of $Q_{\ell,\text{max}}(\text{Pe})$ . . . . .	68
7.9	Packing fraction probability distribution far above the critical point ( $\text{Pe} \approx 55.35$ ) . . . . .	71
8.1	Sketch of the system geometry used in the improved subbox distribution method . . . . .	74

8.2	Test of the improved subsystem distribution method on the 2D Ising model (Data by Florian Dittrich) . . . . .	75
8.3	Test of the improved subsystem distribution method on the 2D Lennard-Jones (LJ) model . . . . .	77
8.4	Exemplary snapshots demonstrating the application of the improved subsystem distribution method for ABPs . . . . .	79
8.5	Distribution of the packing fraction in the new method . . . . .	81
8.6	Effect of the new method on the packing fraction distribution $p(\phi)$ . . .	82
8.7	$Q_\ell$ vs. $Pe$ in the improved method . . . . .	83
8.8	Phase diagram of ABPs including the critical point . . . . .	85
8.9	Cluster size distribution close to the critical point . . . . .	87
8.10	Static structure factor for different $Pe$ . . . . .	89
8.11	Static structure factor assuming different values for the anomalous dimension . . . . .	89
8.12	Radial distribution function for different $Pe$ . . . . .	90
9.1	Scaling plot of the order parameter against $\tau$ . . . . .	94
9.2	Phase diagram of ABPs including a fit of the binodals close to $Pe_{cr}$ . . .	95
9.3	Linear fit of $Q_\ell(\tau)$ at the crossing point to extract $dQ_\ell/d\tau _{\tau \approx 0}$ . . . . .	97
9.4	Scaling plot of $dQ_\ell/d\tau _{\tau \approx 0}$ against $\ell$ . . . . .	97
9.5	Scaling plot of $\chi_\ell$ vs. $\ell$ . . . . .	99



# List of Symbols

$\eta$  Anomalous dimension.

$Q$  Binder moment ratio.

$\xi$  Correlation length.

$\alpha, \beta, \gamma, \delta, \nu$  Critical exponents.

$\rho$  Density.

$D$  Diffusion constant.

$d$  Dimensionality.

$F$  Free energy.

$\sigma$  Lennard Jones unit for length/Stress tensor.

$\phi$  Packing fraction.

$p(\phi)$  Packing fraction probability distribution.

$\varphi$  Particle angle.

$r$  Particle distance.

$m$  Particle mass/Order parameter.

$N$  Particle number.

$\hat{e}$  Particle orientation.

$\mathbf{x}$  Particle position.

$v_0$  Propulsion velocity.

Pe Peclet number.

$U$  Potential energy.

$g(r)$  Radial distribution function.

$\tau$  Relative distance from the critical point.

$D_r$  Rotational diffusion constant.

$S(q)$  Static structure factor.

$\ell$  Subsystem dimension.

$\chi$  Susceptibility.

$L$  System dimension.

$T$  Temperature.

$t$  Time.

# Abbreviations

**ABDs** active Brownian dimers.

**ABPs** active Brownian particles.

**BD** Brownian dynamics.

**COM** center of mass.

**FENE** finite extensible nonlinear elastic.

**GC** grand canonical.

**HCSW** hard core square well.

**LJ** Lennard-Jones.

**MC** Monte Carlo.

**MD** molecular dynamics.

**MIPS** motility induced phase separation.

**RPM** restrictive primitive model.



# Introduction

*“A theory is the more impressive the greater the simplicity of its premises is, the more different kinds of things it relates, and the more extended is its area of applicability. Therefore the deep impression which classical thermodynamics made upon me. It is the only physical theory of universal content concerning which I am convinced that, within the framework of the applicability of its basic concepts, it will never be overthrown.”*  
– Albert Einstein [32]

Already in 1949, Albert Einstein, as quoted above, states that classical thermodynamics as a theory will stand the test of time. More generally, equilibrium thermodynamics as well as statistical physics are far from being studied exhaustively. Nonetheless, the underlying principles seem to be understood, forming a comprehensive theory based on few simple premises [117]. However, equilibrium is, to some extent, only an idealization. While its approximative application works well for a wide range of systems, it does not hold true in all cases. Generally, the world is not in equilibrium and the properties of those non-equilibrium systems where the approximation of equilibrium fails are distinctly less understood. Certainly, the behavior of some non-equilibrium systems still can be described rather well. Especially those that are still close to equilibrium, meaning those in the so-called linear response regime, are rather well studied. Their theoretical description based on fluctuation-dissipation theorems, Onsager’s reciprocal relations, and Green-Kubo relations is well founded [117]. However, sufficiently far from equilibrium, this approach breaks down. In this case, there are still some theoretical tools at our disposal, such as the Boltzmann transport equation, and stochastic thermodynamics [117, 118]. Nonetheless, no comprehensive theory similar to equilibrium physics exists. Therefore, especially in recent years, a major focus of research in statistical physics has been on studying non-equilibrium systems, working towards a better understanding of the underlying laws and principles.

One such group of systems, which has attracted significant attention in the last decade, has been active particles. The common, name-giving feature of these particles is that they exhibit some mechanism to convert (free) energy into directed propulsion [145, 129], which drives the system out of equilibrium. Obviously, this definition is very broad. For example, it is shared by many biological systems, such as polymer networks driven by actomyosin [72, 115, 113], mobile bacteria [171,

156], sperm cells [2, 82], or on macroscopic length scales, schools of fish [65] or flocks of birds [4]. Apart from these biological examples, active particles can also be produced artificially. Especially during the last decade, several mechanisms have been found to produce self-propelled colloidal particles [7]. By coating one end of a rod-like particle or one hemisphere of a bead with a different material, the symmetry of the particle is broken. Depending on the coating material, catalytic reactions [97, 55, 95], self-thermophoresis [59], or demixing of a surrounding supercritical fluid [148, 19, 20] can lead to self-propulsion of a suspended particle. Other possible propulsion mechanisms include electro-osmotic flows [106], Marangoni flows [98, 54], or artificial flagella [30]. One exemplary experimental realization, that is particularly close to the model system studied in this work, are active Janus particles. Experimentally, they can for example be realized by coating one hemisphere of silica particles with gold [148] or carbon [19] as shown in Figure 1.1a). These particles can then be placed in a water-lutidine mixture, whose critical temperature is at  $T_{cr} = 307K$  [148]. For a system just below this temperature, this leads to normal Brownian motion of the Janus particles. However, if they are illuminated with a laser of sufficient intensity, the particles begin to also self-propel [148]. The two hemispheres of the particles have distinctly different absorption rates. Consequently, only the coated hemisphere is heated up sufficiently, to cause a local demixing of the surrounding solvent, which causes the propulsion along the direction broken symmetry axis (cf. Figure 1.1a)). This director changes slowly in time via rotational diffusion of the particle, thus leading to a directed motion over a significant time [148].

Even though, the individual propulsion mechanisms are interesting in and of themselves, studying a collective of interacting active particles reveals fascinating collective behavior including swarming [151], turbulent motion [29], giant number fluctuations [102, 89], and clustering [9, 27, 142, 121]. In case of active Janus spheres, clustering is caused by self-trapping [20]. Due to collisions between particles, their paths can become blocked. This is shown in Figure 1.1b), where multiple particles are blocking each other. Separation of these particles can only occur by sufficient rotation of the particles via (slow) rotational diffusion. During this time, additional particles can arrive and crash into the building cluster. Eventually, a large cluster is formed that is stabilized by particles on its surface pointing inwards [20]. The close resemblance of this phase-separation to an equilibrium gas-liquid transition raises the question to what degree concepts of equilibrium thermodynamics can be applied to this non-equilibrium system.

The exact individual and collective behavior of active particles depends on the specific system that is studied, e.g. the underlying propulsion mechanism and the form of interactions between individual particles. Nonetheless, on a more general scale, it is of great interest to find commonalities between systems, ultimately aiming to un-

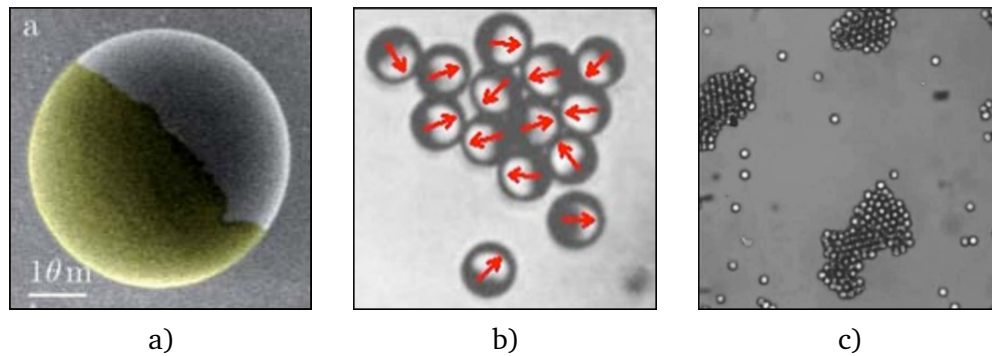


**Fig. 1.1.:** a) Scanning electron microscopy image of a Janus particle (Reproduced from Reference [148] with permission of The Royal Society of Chemistry). One hemisphere of the silicate bead is coated with gold, breaking the symmetry of the particle. Subsequently, such particles are placed in a water–lutidine mixture just below its critical point. Illumination with a laser now leads to a local heating of the coated hemisphere and consequently to a local demixing of the surrounding solvent which results in a propulsion of the particle [148]. b) Experimental snapshot of a small cluster (Reprinted excerpt of Figure 5a) with permission from [Buttinoni et al., *Physical Review Letters*, 110, 238301, 2013]. Copyright 2013 by the American Physical Society). The particles orientations are indicated by red arrows. Colliding particles block each others path. Only due to (slow) rotational diffusion, the particles can separate again. During this time other particles can arrive and crash into the building cluster [20]. c) Experimental snapshot of multiple larger clusters (Reprinted Figure 4c) with permission from [Buttinoni et al., *Physical Review Letters*, 110, 238301, 2013]. Copyright 2013 by the American Physical Society). Self-trapping can lead to macroscopic clusters that are stabilized by particles on the surface pushing inwards and eventually phase-separation [9, 20].

derstand the underlying non-equilibrium physics that arise when particles are driven out of equilibrium by directed propulsion. Similarly to statistical mechanics in equilibrium, studying such underlying mechanisms is often facilitated by examination of simplified model systems, that, in a generalized fashion, incorporate the important common features of the class of systems one is interested in. E.g. the understanding of the gas-liquid transitions in equilibrium greatly benefited from studies on the Ising-model in its lattice gas interpretation or the off-lattice Lennard-Jones model. Both models are very simple but still show a gas-liquid transition, which allows to study its properties without complications and interference by more realistic fluid models. To that end, active Brownian particles (ABPs) arose as a minimal model system for active matter that still encompasses its main features, specifically the name-giving propulsion or activity as well as interactions, which are implemented in form of excluded volume interactions [42]. The details of the model are presented in Chapter 3. Besides ABPs, other simple model systems describing self-propelled particles have been both proposed and studied. These include lattice models [127, 125, 157], but also other off-lattice models such as run-and-tumble particles motivated by the behavior of *E. coli* [137, 22], or the Vicsek model describing cooperative movement e.g. for flocks of birds [146]. However, ABPs have proven very successful in recent years and were studied extensively by several different groups [42, 104,

125, 11, 134, 167, 121] thus serving as a quasi-standard of minimal models for active particles.

Despite their simplicity, ABPs show a fascinating collective behavior. Even though there are only repulsive interactions between particles, at sufficiently high propulsion strengths, they exhibit clustering and phase separation which closely resembles a gas-liquid transition in equilibrium [42, 104, 10]. In this analogy, the propulsion strength plays the role of an inverse temperature. While this behavior has been observed previously, no quantitative study of the phase boundaries and the position of the analogue of binodal lines has been done. The phase diagram has only been studied by using methods that are expected to be finite size dependent [104, 134]. Therefore, the resulting phase boundaries have to be interpreted with caution. Consequently, this work's first focus is to provide high-accuracy, quantitative estimates of the phase boundaries that do not suffer from finite size effects. The corresponding results are shown in Chapter 4.

By design, ABPs sacrifice most individual properties of real self-propelled particles for the sake of generality as well as simplicity. Nonetheless, it is of great interest how these details influence their behavior. For example, the effect of anisotropic shapes has been studied in form of dumbbells [136, 48, 25], more complicated active colloidal molecules [128, 79] or even polymer-like chains consisting of explicitly self-propelled beads [64, 33] or with effective activity introduced in form of an increased local temperature [124]. Especially for microswimmers, the explicit inclusion of hydrodynamics, which are included only effectively and incompletely in ABPs, can have an impact on the specific phase behavior [85, 173, 15]. Furthermore, ABPs are typically studied in two dimensions. In addition to easier implementation, this is caused by the fact, that many experimental realizations of microswimmers are also in quasi two dimensions, either because they rely on the surface chemistry [106], they are not density matched and thus sink to the bottom [94] or because a single particle layer simplifies the supply with fuel or energy through illumination [148, 19, 20]. Nonetheless, three-dimensional microswimmers are not impossible and also from a purely theoretical point of view, the influence of dimensionality is interesting in and of itself [134, 167]. Based on our estimates of the binodal lines in standard ABPs, Chapter 6 studies some of these effects. In particular, we study the influence of anisotropic particle shape and dimensionality, which in turn might foster the understanding of corresponding effects in experimental systems.

However, our main goal in studying ABPs is not to allow for quantitative comparison with experimental results, but to understand the underlying principles of the non-equilibrium effects seen in active matter. Another key part in improving our understanding of these is to examine apparent analogies of concepts in these system far from equilibrium with laws known from equilibrium thermodynamics. Finding



proper analogues for thermodynamic quantities in ABPs, but also understanding their limits might enable us to gain insight not only into this specific model system, but to more generally examine to what extent concepts of standard thermodynamics can be applied in non-equilibrium systems. Recently, large advances have been made in that regard [138, 129]. Especially, the analogue of a thermodynamic pressure has been studied extensively, as pressure in equilibrium contexts can be derived not only from a free energy but also via mechanical forces on surrounding walls, which should be well-defined even far from equilibrium [76, 166, 83, 169, 139, 49, 125, 126, 91, 163]. To that end, Chapter 5 verifies the intensiveness of the pressure as defined by Takatori et al. [139] and Yang et al. [169]. Furthermore, it presents results on the interfacial tension in ABPs stemming from that pressure definition. Going beyond the pressure, the question remains, if and how other analogues to thermodynamic quantities such as a chemical potential might be defined [133, 138, 131, 125]. A proper definition of a chemical potential would be of particular interest, as it might allow for simulations with fluctuating particle numbers, analogous to grand canonical (GC) simulations in equilibrium.

So far, the focus has been mainly on the phase separated region at high propulsion strengths. Even though significant questions remain unanswered, impressive advances have been made in understanding the properties of ABPs in this regime (as referenced above). However, the region of the phase diagram around the critical point is severely understudied. Both the exact position of the critical point, but also whether the system follows any known or unknown universality class, remain undetermined. Some works using either an effective mean field equation of state [138] or fits to the binodal lines [131] have given some rough estimates of the position of a putative critical point, but a rigorous determination of said position and of corresponding critical exponents, analogously to finite-size scaling evaluations in equilibrium, are still unavailable. So far, mainly the influence of activity on systems with underlying equilibrium phase transitions, such as Lennard-Jones particles [101], or a variant of the Asakura-Oosawa model [141, 143] have been studied before. In a system with an activity induced, pure non-equilibrium transition, such as ABPs, no quantitative estimate of the critical point's position by direct simulation is available.

A major part of this work is therefore focused on finding the exact position of the critical point in ABPs. Subsequently, said determination even allows first studies of associated scaling laws and to what extent they hold far from equilibrium. The obtained corresponding exponents are compared to those known for equilibrium universality classes, to again test the limits of the analogy between the propulsion induced phase transition and a gas-liquid transition in equilibrium. The influence of driving a system out of equilibrium has been examined before, e.g. in the driven lattice gas [6], the Ising model under shear [164], or an active variant of the

Lennard-Jones gas [101]. However, in case of ABPs, we study a pure non-equilibrium transition, which raises the question if scaling laws still hold and how far they follow universality classes known from equilibrium. Chapters 7, 8, and 9 aim to answer these questions.

# Theoretical background

In this introductory chapter, we will recapitulate basic concepts that are used throughout the rest of the thesis. This is exclusively background information, and thus nothing presented here is a new result. Unless referenced otherwise everything can be found in standard textbooks on either statistical physics or computer simulations. Further details can be found in the textbooks, that were followed here [74, 86, 117, 1].

## 2.1 Brownian dynamics simulations

Computer simulations in general and molecular dynamics (MD) simulations in particular have emerged as a convenient tool in addition to analytical theory and experiments. As they allow direct inspection and control over all degrees of freedom, they facilitate fascinating insights into the simulated systems. Here, we will give a very short recapitulation of the basic ideas behind molecular dynamics simulations in general and the specialized Brownian dynamics (BD) simulations that are used throughout this thesis.

### 2.1.1 Langevin equation

In principal, MD simulations solve Newton's equations of motion:

$$m\ddot{\mathbf{x}}_i(t) = -\nabla_i U(\{\mathbf{x}_i\}) \quad (2.1)$$

via numerical integration. This results in a trajectory of particle positions  $\mathbf{x}_i(t)$  (and velocities  $\mathbf{v}_i(t)$ ) which allows to compute the time evolution of quantities we are interested in. Based on the hypothesis of ergodicity, the time average of said property is equal to the ensemble average. Thus, we can compute ensemble averages of quantities of interest by sufficiently sampling the time evolution of the positions  $\mathbf{x}_i(t)$  of all particles in our system.

However, in many cases we are not interested in all degrees of freedom of the system. More specifically, in a lot of cases we only want to study a very small subset of them. One example are large particles that are suspended in a liquid. Typically, we are

interested in the properties of those particles and not in the fast dynamics of the atoms or molecules in the liquid. Nonetheless, our time step would be bound by the dynamics of these atoms or molecules and even worse we would be forced to keep track of all their positions and velocities. This very quickly becomes completely unfeasible. Dropping the liquid from the equations is also unsatisfactory as it has a significant impact on the dynamics of the suspended particles. To solve this problem, we study only the interesting degrees of freedom, namely the positions and velocities of the large particles while treating the influence of the fast degrees of freedom, namely the liquid's atoms or molecules, stochastically.

The influence on the suspended particles is caused by collisions with the solvent's atoms or molecules. On average, this slows down the velocity of the suspended particles which can be modeled by a friction term. Nonetheless, there are additional fluctuations of the particles' movements due to the collisions, which results in the need for a stochastic force. This treatment gives rise to a second order ordinary stochastic differential equation, called the Langevin equation:

$$m\ddot{\mathbf{x}}_i(t) = -\nabla_i U(\{\mathbf{x}_i\}) - \gamma m \dot{\mathbf{x}}_i(t) + \lambda \mathbf{R}_i(t), \quad (2.2)$$

where  $\gamma$  is the friction coefficient and the components of  $\mathbf{R}_i(t)$  are uncorrelated random variables with unit variance. Under the assumption that the collision time of the liquid's atom with the large particle is negligible, we can assume that this random variable is uncorrelated in time and between particles. The variance of the stochastic term  $\lambda^2$  is given by the Einstein relation:

$$\lambda^2 = 2\gamma m k_B T. \quad (2.3)$$

### 2.1.2 Overdamped limit

Particles described by the models in this work are typically suspended at low Reynolds numbers, meaning that the inertial forces acting on them are negligibly small compared to the viscous forces caused by the liquid. This overdamped limit is effectively given by  $m \xrightarrow{\gamma m = \text{const.}} 0$ . In this limit, it is more meaningful to express the equation in terms of the free particle diffusion constant  $D$  instead of the friction strength  $\gamma m$ . The relation between these parameters is:

$$D = \frac{k_B T}{\gamma m}. \quad (2.4)$$

In the overdamped limit, the equations of motion simplify to a first order ordinary stochastic differential equation:

$$\dot{\mathbf{x}}(t) = -\frac{D}{k_{\text{B}}T} \nabla_i U(\{\mathbf{x}_i(t)\}) + \sqrt{2D} \mathbf{R}_i(t). \quad (2.5)$$

### 2.1.3 Rotational diffusion

So far, only the translational degrees of freedom have been considered. Additionally, there are rotational degrees of freedom. In this work, only spherically symmetric particles are considered, e.g. disks in two dimensions and spheres in three dimensions. Therefore, all particles are assumed to undergo free rotational diffusion with rotational diffusion constant  $D_r$  without any torques acting on them. Their orientation is described by a unit vector  $\hat{\mathbf{e}}$ . In two dimension, the situation is simple as this vector is fully determined by its angle  $\varphi$  with the positive  $x$ -direction. The time evolution of  $\varphi$  due to free rotational diffusion is then given by Gaussian white noise with variance  $2D_r$ :

$$\begin{aligned} \hat{\mathbf{e}}(t) &= \begin{pmatrix} \cos \varphi(t) \\ \sin \varphi(t) \end{pmatrix} \\ \dot{\varphi}(t) &= \sqrt{2D_r} R_r(t), \end{aligned} \quad (2.6)$$

where  $R_r(t)$  is Gaussian distributed, has unit variance, and is uncorrelated in time and between different particles. The situation in three dimensions is more complicated. The description we settled for is given by [61, 134]:

$$\dot{\hat{\mathbf{e}}}(t) = \sqrt{2D_r} (\hat{\mathbf{e}}(t) \times \mathbf{R}_r(t)) \quad (2.7)$$

Here, the components of  $\mathbf{R}_r(t)$  are Gaussian distributed, unit variance random variables. Again the components are uncorrelated among themselves as well as between particles and for different times.

### 2.1.4 Numerical integration

To compute ensemble averages of quantities of interest, we have to numerically integrate these equations of motion. However, due to their stochastic nature, we cannot simply apply the velocity-Verlet integrator that is commonly used in MD simulations. The simplest way to numerically solve Eq. (2.5) is via an Euler-scheme,

which in this context is attributed to Ermak [35]. It results in the following update rules for two-dimensional systems:

$$\begin{aligned}\mathbf{x}(t + \delta t) &= \mathbf{x}(t) - \frac{D}{k_{\text{B}}T} \nabla_i U(\mathbf{x}(t)) \delta t + \sqrt{2D\delta t} \mathbf{R}(t), \\ \phi(t + \delta t) &= \phi(t) + \sqrt{2D_r\delta t} R_r(t).\end{aligned}\tag{2.8}$$

In three dimensions, the update of the orientation has to be modified:

$$\hat{\mathbf{e}}(t + \delta t) = \frac{\hat{\mathbf{e}}(t) + \sqrt{2D_r\delta t} (\hat{\mathbf{e}}(t) \times \mathbf{R}_r(t))}{|\hat{\mathbf{e}}(t) + \sqrt{2D_r\delta t} (\hat{\mathbf{e}}(t) \times \mathbf{R}_r(t))|}.\tag{2.9}$$

Naively, one might be tempted to use only the simple approach given by the numerator of the equation above. This, however, would not conserve the unit length of the orientation but lead to a systematic increase of its absolute value at every step. The problem can be solved by normalizing the vector again after every step [61], which is achieved by the denominator in Equation (2.9).

### 2.1.5 Unit system

In computer simulations, it is common to express quantities not in SI units but in a reduced unit system. First of all, this simplifies equations significantly. Furthermore, it allows to choose a unit system in which all quantities have near-unit values. Measuring lengths in meter or times in seconds would lead to values smaller than  $10^{-9}$ , which are difficult to handle by both, humans and computers. Choosing relevant scales as units avoids this and also facilitates comparisons between different systems. In this work the usual set of units for an overdamped system of spherically symmetric particles is used. The length scale is set by the diameter of the particles  $\sigma$ . For the time scale, we choose the diffusion time  $\sigma^2/D$ . Energies are measured in units of the thermal energy  $k_{\text{B}}T$ . This unit system will be used throughout this work and to simplify notation the respective units will not be written out explicitly, meaning that e.g. the specification of a box length  $L = 100\sigma$  will be shortened to  $L = 100$ .

## 2.2 Phase transitions

Depending on thermodynamic variables such as temperature, density, and pressure, systems of matter can be in different phases of similar properties. The most common examples are gases, liquids, and crystalline solids. Upon changes of the thermodynamic parameters, systems can also change from one of those phases into another. In

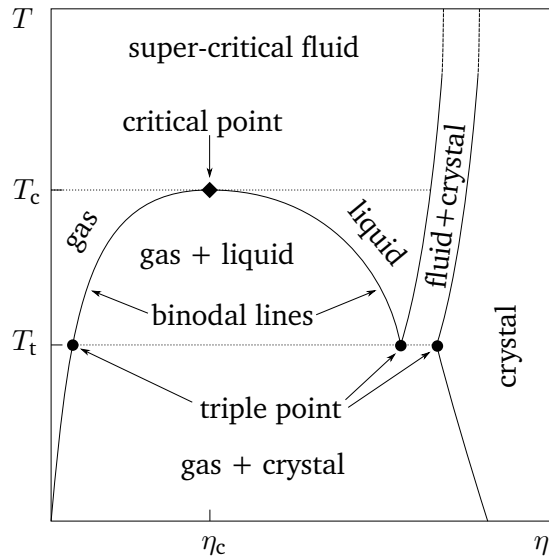


**Fig. 2.1.:** Sketch of a simple phase diagram: The sketch shows phase boundaries of gas, liquid and crystalline phases in the density/packing fraction ( $\phi$ ) vs. temperature ( $T$ ) plane. At low temperatures there are two distinct phases, namely gas at low densities and a solid at high densities. In between, there is coexistence of those two phases. At the triple point temperature  $T_t$ , all three phases coexist. Above this temperature but below the critical temperature, all three phases can arise, depending on the density of the system. At low densities the system is in the gas phase. At intermediate densities, there is a liquid phase. The homogeneous gas and liquid regions are separated by an area that is bounded by binodal lines and in which there is coexistence of the gas and liquid phases. Further increase of the density leads to liquid-crystal coexistence and finally to a homogeneous crystalline phase. The binodal lines meet at the critical point. For  $T \geq T_{cr}$ , the difference between gas and liquid phases vanish continuously such that there is no more gas-liquid phase transition but only a super-critical fluid phase. At high densities, there is still the phase transition to a crystalline solid, though.

many cases, rather than occurring gradually, these changes happen at specific values of the thermodynamic variables. These changes are then called a phase transition.

### 2.2.1 The gas-liquid transition

Figure 2.1 shows a sketch of a generic phase diagram for a system exhibiting three different phases: gas, liquid, and crystal. The state parameters are the packing fraction ( $\phi$ ) or density on one axis and the temperature ( $T$ ) on the other. While it is more common to present the phase diagram using different state parameters, namely pressure and temperature, density instead of pressure is chosen here, as both temperature and density can be set directly in a BD simulation.

At low temperatures, there are two distinct phases. At low densities the system is in the gas phase. For high densities, the system is in a crystalline state. At intermediary

densities, there is coexistence of gas and crystal. This phase transition is not the one we are interested in though. Only for temperatures above the triple point ( $T = T_t$ ) a liquid phase arises. Exactly at the triple point temperature, all three phase can coexist, hence its name. Above the triple point temperature, all three phases can arise in isolation. At high densities, there is still a crystalline solid. Lowering the density results in liquid-crystal coexistence until eventually only liquid is left. For even lower densities, the phase transition we are interested in arises, namely the gas-liquid transition. While at very low densities, there is a homogeneous gas, and at intermediary densities a pure liquid state occurs, there is a coexistence region in between, which is bounded by the so-called binodal lines. Systems in a state in the coexistence region will phase separate into a gas and a liquid state, each with the respective binodal density. For higher temperatures, the coexistence region becomes narrower and thus the densities of the coexisting liquid and gas states become more similar. Eventually, the binodal lines join at the critical point  $T = T_{cr}$ . For  $T \geq T_{cr}$  there is no discontinuous difference in the densities of gas and liquid states. For temperatures above  $T_{cr}$ , there is only one super-critical fluid state. Consequently, there is no phase transition but a continuous shift from a more gas- to a more liquid-like state. While the systems that will be studied in this work are in non-equilibrium, their phase behavior shows a striking likeliness to the gas-liquid transition up to the critical point. Properties of a system in the vicinity of a critical point will be studied in the following in greater detail.

## 2.2.2 Order parameter

Especially in systems featuring a critical point, the corresponding phase transition is commonly parametrized by a so called order parameter  $m$ . It is defined in a way, that it is zero in the unordered phase where there is no transition and then starts to continuously grow going into the ordered phase along some control parameter. In case of the equilibrium gas-liquid transition, a good control parameter is the temperature, or more commonly, the relative distance from the critical point along the temperature direction:

$$\tau = \frac{T - T_c}{T_c}. \quad (2.10)$$

A good order parameter is the difference in densities between the gas and the liquid phase at the transition:

$$m = \phi_{liq} - \phi_{gas}. \quad (2.11)$$

Being defined like this, we can directly see from the phase diagram (cf. 2.1), that indeed for  $T < T_{cr}$ , corresponding to  $\tau < 0$ , the order parameter  $m$  is non-zero. Going towards criticality ( $\tau = 0$ ), the order parameter continuously vanishes, becoming zero exactly at the critical temperature. Above criticality ( $\tau > 0$ ), there is only the supercritical fluid, and thus the order parameter remains zero. The concept of an



order parameter is not solely associated with a gas-liquid transition, but different order parameters can be defined in other systems that feature a critical point (at non-zero temperature). Another well known example for a phase transition and its respective order parameters is the Ising model in two or more dimensions, featuring the scalar magnetization as a (one dimensional) order parameter in its para- to ferro-magnetic transition. While the order parameter is scalar and real in case of the gas-liquid transition of a simple liquid as well as in the Ising model, it can also be of higher dimensionality and complex.

### 2.2.3 Classification of phase transitions

Following the convention of Ehrenfest, phase transitions can be classified to be of a certain order. This classification is based on the fact that the free energy is a non-analytic function of the control parameter at the transition point. If there the lowest derivative with respect to some thermodynamic variable, that is not continuous, is the  $n$ th, the transition is classified to be of  $n$ th order. Transitions between the same phases can change order at different points in the phase diagram. E.g., while the transition from a gaseous state to a liquid state is of second order at the critical point, it is of first order for all temperatures below the critical temperature. For  $\beta < \beta_{\text{crit}}$ , one first derivative of the free energy, namely the volume being the first derivative of the free energy with respect to the pressure, undergoes a discrete jump at the transition, whereas at the critical point, first derivatives are still continuous. However, susceptibilities are discontinuous at the critical point. The other transitions (gas-crystal, liquid-crystal, and supercritical fluid-crystal) are all of first order.

### 2.2.4 Scaling laws and universality

As mentioned above, at the critical point, the phase transition between gas and liquid is of second order and thus, the free energy and its first derivatives are continuous. As defined above, though, at the point of second order phase transition, the susceptibilities diverge. It turns out that these divergences are algebraic (or logarithmic) in nature. This has been verified both in experiments and theory [63]. It is by no means their unique property, but these algebraic (or logarithmic) divergences can be observed in systems featuring a critical point in general, e.g. the Ising model's para- to ferro-magnetic transition shows an analogous behavior. Additionally to the susceptibilities, also correlation lengths and times diverge algebraically. To summarize, following the notation introduced by Fisher [45], these power laws can be written as follows:

- **Heat capacity exponent  $\alpha$ :**

Approaching the critical point both from above and below, the specific heat diverges following a power law

$$C \propto |\tau|^{-\alpha}. \quad (2.12)$$

Note, that here, but also for all other power laws, an exponent of 0 is usually attributed to a logarithmic divergence.

- **Order parameter exponent  $\beta$ :**

Per definition, the order parameter is zero in the disordered phase. In the ordered phase its growth is governed by a power law

$$m \propto |\tau|^\beta. \quad (2.13)$$

- **Susceptibility exponent  $\gamma$ :**

Similarly to the specific heat, the susceptibility diverges when approaching the critical point from both the ordered and the disordered phase. This power-law divergence follows

$$\chi \propto |\tau|^{-\gamma}. \quad (2.14)$$

- **Exponent  $\delta$ :**

At the critical point, the order parameter's value follows a power law when applying an external field  $H$

$$m \propto H^{1/\delta}. \quad (2.15)$$

- **Anomalous dimension  $\eta$ :**

Away from criticality, the order parameter correlations decay exponentially with increasing distance defining the correlation length  $\xi$ . At criticality the decay becomes algebraic

$$\langle m(0)m(x) \rangle \propto x^{-d+2-\eta}, \quad (2.16)$$

where  $d$  is the dimensionality of the system.

- **Correlation length exponent  $\nu$ :**

As mentioned above the order parameter correlations decay exponentially. The resulting correlation length itself diverges when approaching the critical point

$$\xi \propto |\tau|^{-\nu}. \quad (2.17)$$

**Tab. 2.1.:** The table shows the critical exponents of the Ising universality class in two and three dimensions as well as for the mean field universality class. While the exponents for two-dimensional Ising [92, 168] and mean field universality [75] can be determined analytically, the results for the three-dimensional Ising model have to be computed numerically via Monte Carlo simulations [53] or conformal bootstrap [34, 73] by which the results cited here were computed.

	<b>2D Ising</b>	<b>3D Ising</b>	<b>MF</b>
$\alpha$	0	0.110 08(1)	0
$\beta$	1/8	0.326 419 0(3)	1/2
$\gamma$	7/4	1.237 075(10)	1
$\delta$	15	4.789 84(1)	3
$\eta$	1/4	0.036 298(2)	0
$\nu$	1	0.629 971(4)	1/2
$\omega$	2	0.829 66(9)	0

It should be noted, that this list is slightly simplified, assuming that the exponents  $\alpha$  and  $\gamma$  are the same in the ordered and disordered phase. While this holds true for all universality classes that are referenced herein (i.e. 2D-, 3D-Ising, and mean field), generally this is not necessarily true. Multiple more or less simple models in which for example the susceptibility exponent  $\gamma$  differs between high and low temperature phases were presented in the literature (e.g. in [90, 78]). Nonetheless, we will only refer to one exponent  $\gamma$  and  $\alpha$  here, as such differences do not arise in any of the models relevant here.

The observation of scaling laws in various different systems is already fascinating. The divergent correlation length gives rise to an even more profound similarity. Essentially, as nicely explained in [86, 117], the correlation length grows indefinitely and thus eventually becomes much larger than all other length scales of the system (e.g. the extent of the attractive range of the potential in a gas-liquid transition). Therefore, the correlations associated with this length scale start to dominate over all other scales and this causes the system's behavior to only depend on global properties such as dimensionality of the system and the order parameter as well as symmetries of the system. This property is called universality. Systems sharing the same global parameters belong to one universality class and share the same set of critical exponents. For example, short ranged systems with a one-dimensional order parameter typically fall into the Ising universality classes. Their respective exponents are shown in Table 2.1 for reference. They are valid for a variety of systems such as for the gas-liquid critical point in a Lennard-Jones (LJ) fluid [18, 160], the hard core square well fluid [93] and even the long-ranged restrictive primitive model [77].

It turns out, though, that not all of these exponents are independent. Rather, there are a variety of thermodynamic inequalities, which can be proven analytically [112, 46]. Some of these inequalities actually turn out to hold as equalities in exper-

iments, simulations and exactly solved models. One example is the Rushbrook (in)equality [112, 36]:

$$\alpha + 2\beta + \gamma = 2. \quad (2.18)$$

Other equalities that will be used in this thesis are

$$\gamma = \nu(2 - \eta), \quad (2.19)$$

and one hyper-scaling relation [158]

$$2 - \alpha = d\nu. \quad (2.20)$$

In case of the Ising universality classes, there are five independent equations, which thus reduce the set of independent exponents to two [86].

## 2.3 Finite size scaling

Based on the scaling laws, in particular on the scaling of the free energy, additional insights can be drawn with respect to the behavior of a finite system. This is known as finite size scaling theory [44, 58, 47, 13]. Studying a finite system of size  $L$ , the scaling dependence of the free energy can be derived by observing that the diverging correlation length will be eventually bounded by the system size  $L$ . As explained in [74], this results in an effective scaling in terms of  $L/\xi \propto \tau^\nu L$  or, more conveniently in terms of the scaling variable  $\tau L^{1/\nu}$ :

$$F(L, \tau, H) = L^{-(2-\alpha)/\nu} \mathcal{F} \left( \tau L^{1/\nu}, HL^{(\gamma+\beta)/\nu} \right). \quad (2.21)$$

Thermodynamic properties can now be derived starting from this free energy via differentiation. By also applying the scaling relations 2.18, 2.19, and 2.20, one arrives at the following simple scaling laws for thermodynamic quantities, which describe the scaling of said quantities with changing box dimension  $L$ :

$$\begin{aligned} \langle m \rangle &= L^{-\beta/\nu} \mathcal{M} \left( \tau L^{1/\nu}, HL^{(\gamma+\beta)/\nu} \right), \\ \langle \chi \rangle &= L^{\gamma/\nu} \chi \left( \tau L^{1/\nu}, HL^{(\gamma+\beta)/\nu} \right), \\ \langle C \rangle &= L^{\alpha/\nu} \mathcal{C} \left( \tau L^{1/\nu}, HL^{(\gamma+\beta)/\nu} \right). \end{aligned} \quad (2.22)$$

Here,  $\mathcal{M}$ ,  $\chi$ , and  $\mathcal{C}$  denote appropriate universal scaling functions. These types of laws form the basis of finite size scaling, allowing to systematically study the influence of the finite size of a system on its properties [74].

So far, the derivation of scaling laws was based on an underlying well-defined free energy (see Eq. (2.21)). This becomes problematic in case of active Brownian

particles. They are driven far out of equilibrium and there is no free energy that governs the whole system. Nonetheless, it seems that analogous scaling laws remain valid in this non-equilibrium case. Instead of formulating the finite size scaling hypothesis in terms of the free energy, it can instead be laid out in terms of the order parameter probability distribution [109]. In case of the gas-liquid like transition studied in this work, it takes the following form:

$$p(\phi) = L^{-\beta/\nu} \mathcal{P}((\phi - \phi_{\text{cr}})L^{\beta/\nu}, L^{1/\nu}\tau). \quad (2.23)$$

This scaling ansatz reproduces the same scaling law as its free energy-based analog in Equation (2.22). Generally, we will assume that the usual finite size scaling relations known from equilibrium physics remain valid even in our system far from equilibrium and thus even in absence of a well-defined free energy. Based on this assumption we will apply many of the well-developed methods to determine critical points and critical exponents, which were originally developed for equilibrium systems. In particular, we can apply the crossing of Binder cumulants to determine the position of the critical point.

### 2.3.1 Binder cumulant

Motivated by the scaling hypothesis, we define the Binder cumulant [13] which allows to pinpoint the position of the critical point

$$Q(L, \tau, H) = \frac{\langle m^2 \rangle^2}{\langle m^4 \rangle} = \mathcal{Q}(\tau L^{1/\nu}, HL^{(\gamma+\beta)/\nu}). \quad (2.24)$$

This quantity's direct dependence on  $L$  cancels out, leaving only the dependence on  $L$  of the scaling function  $\mathcal{Q}(\tau L^{1/\nu}, HL^{(\gamma+\beta)/\nu})$ . In this function,  $L$  only arises in terms of the parameters  $\tau L^{1/\nu}$  and  $HL^{(\gamma+\beta)/\nu}$ . At criticality,  $\tau$  and  $H$  are zero and thus the cumulant does not depend on the system size:  $Q(L, 0, 0) = Q(0, 0) = \text{const.}$ . Therefore, the cumulant is defined as a well-accessible quantity that is independent of the system size at criticality but system size dependent away from the critical point, which allows us to determine the critical point's position by finding the parameters for which the cumulant's values for different system sizes coincide.

As explained in [13], while the form of the order parameter's probability distribution is non-trivial close to criticality and thus the value of the cumulant cannot be easily predicted, the high- and low-temperature limits of both the probability distribution and consequentially of the cumulant are known.

- For a system at high temperatures and thus far in the disordered region, the order parameter's probability distribution can be well approximated by a Gaussian distribution:

$$P_L(m) = \frac{L^{d/2}}{\sqrt{2\pi k_B T \xi_L}} \exp\left(-m^2 L^d / 2k_B T \xi_L\right). \quad (2.25)$$

The moments of a Gaussian distribution are known and thus the cumulant  $Q(L)$  can be easily computed to be

$$\lim_{\tau \rightarrow \infty} (Q(L)) = \frac{1}{3}. \quad (2.26)$$

So in the high temperature limit, the cumulant will go toward  $1/3$  for all system sizes. As the Gaussian distribution is approached much faster for a larger system containing more particles or spins, we expect the limit to be approached faster for these systems.

- At low temperatures which correspond to a system that is far in the ordered region, the order parameter's probability distribution can be approximated by a bimodal Gaussian with maxima at the binodal values of the order parameter  $M_{\pm}$ :

$$P_L(m) = \frac{L^{d/2}}{\sqrt{2\pi k_B T \xi_L}} \cdot \frac{1}{2} \left( \exp\left(-\frac{(m - M_+)^2 L^d}{2k_B T \xi_L}\right) + \exp\left(-\frac{(m - M_-)^2 L^d}{2k_B T \xi_L}\right) \right). \quad (2.27)$$

Again, the moments of the distribution and therefore the cumulant  $Q(L)$  can be computed. While it does not generally have a simple form, it simplifies in the limit of low temperature where the width of the Gaussians becomes small compared to the difference between  $M_+$  and  $M_-$ :

$$\lim_{\tau \rightarrow -1} (Q(L)) = 1. \quad (2.28)$$

This behavior is also shown in the sketch of cumulant behavior for different system sizes in Figure 2.2. While all curves converge to the same limiting values 1 and  $1/3$  in the low and high temperature limit respectively, they show a different behavior in the intermediary region around the critical temperature. For small system sizes,  $Q(L)$  changes between the limiting values over a rather large range. The slope of the cumulant is comparably small. For increasing system size, the change gets more and more rapid, leading to a steeper slope and approaching a diverging derivative in the infinite system size limit.

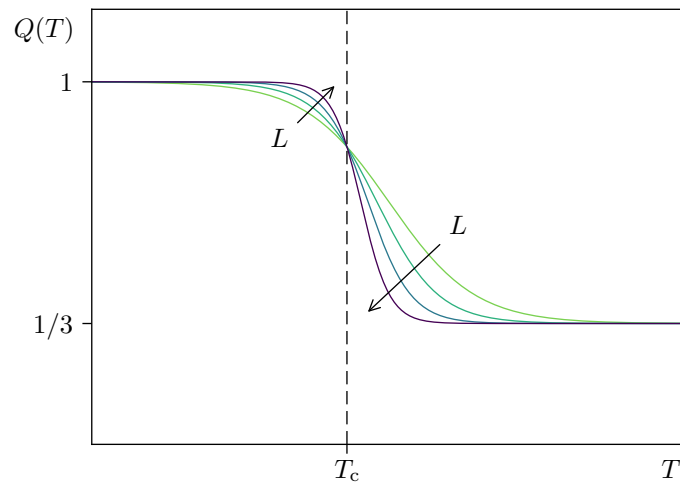


**Fig. 2.2.:** Sketch of a cumulant intersection:  $Q(T)$  curves for different  $L$  are shown in different colors. All curves converge towards 1 in the limit of  $\tau \rightarrow -1$  and to  $1/3$  for  $\tau \rightarrow \infty$  corresponding to  $T \rightarrow 0$  and  $T \rightarrow \infty$  respectively. In the vicinity of the critical point, the curves depend on the system size  $L$ . Small systems change over the largest area and with the smallest slope. Systems of increasing size change more and more quickly and thus with a steeper slope as indicated by the arrows. Still, notably all curves intersect in a single point. This behavior allows to determine the position of the critical point by evaluating  $Q(T)$  for different system sizes.

Regardless of the difference in slopes, as predicted by the scaling analysis, all curves intersect at the critical point. This behavior allows to predict the critical temperature with good accuracy. Note, though that this analysis presumes that  $Q(L)$  is evaluated along a path going through the critical point. This is simple in some cases like the Ising model, where the order parameter is given by the average magnetization along which the system is symmetric and thus the critical magnetization is known to be zero. In other cases such as the gas-liquid transition in a simple fluid, the critical density a priori is not known. But here, as in most cases in equilibrium systems, the critical point turns out to be located on the extension of the rectilinear diameter, which is the mean of binodal densities for corresponding points on said binodal lines. In that case, the rectilinear diameter can be used as the path along which  $Q(L)$  is evaluated [152].

## 2.4 Software

All simulations for active particles and dimers that are shown in this work were done using a MPI-parallelized C++ simulation package developed by the author based on a code base available in the KOMET work group. The original author of the code was Alexander Winkler. The code's MD-package was subsequently extended and

maintained by Benjamin Trefz and the author. Among others, active and passive BD simulations, the implementation of bonds as well as the code's ability to perform simulations in two dimensions were written by the author.

In addition to the code's on-the-fly analysis capabilities, a Python-wrapper adding several analysis tools was developed by the author in collaboration with Benjamin Trefz. In particular the number of available tools for analysis was heavily extended by the author. Furthermore, Python and its packages NumPy [149], SciPy [60, 149], and Pandas [87] were used extensively. All plots in this work were done using the Python package Matplotlib [57]. 3D renderings were done using povray [99].

The predominant part of the computations were done on the supercomputer clusters Mogon I and II, operated by the ZDV of Johannes Gutenberg University Mainz.



## Active Brownian particles

### 3.1 Equation of motion for active Brownian particles

The focus of this work are ABPs [42, 104, 125, 11, 134, 167, 121]. The particles in this very simple model system are described as hard and spherically symmetric. Dynamics are assumed to be overdamped. Their defining property, namely their activity, is described by a propulsion of constant magnitude along their orientation  $\hat{e}(t)$ , which undergoes free rotational diffusion. This results in an additional term in the standard equation of motion of Brownian dynamics given in Eq. (2.5) that is highlighted in red:

$$\dot{\mathbf{x}}_i(t) = -\frac{D}{k_B T} \nabla_i U(\{\mathbf{x}_i(t)\}) + v_0 \hat{e}_i(t) + \sqrt{2D} \mathbf{R}_i(t). \quad (3.1)$$

### 3.2 Effect of the propulsion

As one might expect, driving the system out of equilibrium via this active propulsion can change the particles' dynamics drastically. In the passive case, which is being recovered for vanishing propulsion strength  $v_0$ , free particles move diffusively. This corresponds to a linear increase of the mean square displacement as a function of the time difference  $\langle (\mathbf{x}_i(t + \delta t) - \mathbf{x}_i(t))^2 \rangle = 2d\delta t$ . In the active case, however, particles move not only diffusively but also due to their directed propulsion. Consequently, isotropy is broken as there is now a preferred direction, which also greatly effects the mean square displacement. As studied in great detail by ten Hagen et al. [140], there are three regimes, that differ depending on the relative angle to the particle's orientation at time  $\hat{e}(t)$ . While their work includes analyses for a variety of particle geometries, we will quickly recapitulate their results for active disks in the following. We assume, without loss of generality, that the particle starts out oriented parallel to the  $x$ -axis. Regardless of the studied direction, in the beginning, the mean-square displacement is dominated by the free particle diffusion which results in a linear increase for very small times. Due to its directed nature, the propulsion eventually starts to dominate over the undirected diffusive motion though. As soon as  $v_0 \cdot \delta t$

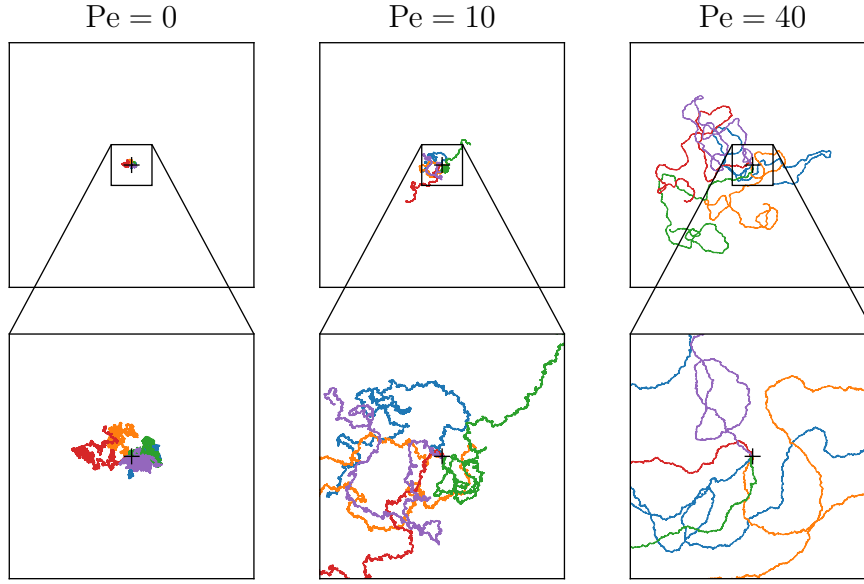


**Fig. 3.1.:** Exemplary trajectories for single free particles with differing propulsion strengths: The three columns show trajectories of five particles each, plotted in different colors. All trajectories are started at the black + and are run for  $\delta t = 10$ . The upper row shows a 120 by 120 box, while the lower row shows a blow-up of size 20 by 20. The columns show different propulsion strengths starting at zero propulsion (passive particle) on the left, increasing the propulsion strength going to the right. All passive particles undergo a purely diffusive motion and thus do not travel large distances. With increasing propulsion strength, the length of quasi-ballistic motion increases such that they travel much farther and in a directed way over long distances.

exceeds  $\sqrt{2d\delta t}$ , there is a crossover in the mean square displacement along the  $x$ -axis towards a ballistic regime ( $\langle (x(t + \delta t) - x(t))^2 \rangle \propto (\delta t)^2$ ). Ultimately, the particle's rotation starts to significantly turn the average orientation ( $\delta t \approx D_r^{-1}$ ). This leads to a second crossover of the mean-square displacement in the  $x$ -direction back to a linear increase in  $\delta t$ . For the MSD in  $y$ -direction there is a crossover towards superballistic motion ( $\langle (y(t + \delta t) - y(t))^2 \rangle \propto (\delta t)^3$ ). Due to the rotation, the particle tends to become more aligned with the  $y$ -axis and thus the effective propulsion in  $y$ -direction becomes larger. However, this will eventually give way to an again diffusive regime as soon as the orientation is sufficiently decorrelated. Averaging over all directions, finally shows that the mean-square displacement undergoes diffusive, then ballistic and ultimately again diffusive regimes. While the power-law dependence thus shows the same exponent as that of a passive particle at high  $\delta t$ , the corresponding prefactor is much higher in case of active diffusion. In this limit ( $\delta t \gg \tau_r = D_r^{-1}$ ), the effective diffusion constant becomes [56]:

$$D_{\text{eff}} = D + \frac{v_0^2}{4D_r}. \quad (3.2)$$

The final two regimes as well as the general effect of the propulsion on a particle's trajectory are illustrated in Figure 3.1. The three columns show the trajectories of five independent active particles distinguished by different colors, each starting at the black + with a random orientation. The run time is  $\delta t = 10$  for each trajectory. The propulsion strength increases going from the passive limit ( $Pe = 0$ ) on the left to a strong active propulsion ( $Pe = 40$ ) on the right. The upper row shows a  $120 \times 120$  box. Especially in the passive case, on that scale, the particle's movement is barely visible. Therefore, the lower row shows a blow-up of size  $20 \times 20$ . The strongly active particle on the right, in turn, travels much farther than what can be captured by the blow-up. While on the large length-scale the trajectories still look rather chaotic (corresponding to the diffusive limiting case), the blow-up shows that for extended stretches, the particles actually travel more or less along straight lines (corresponding to the intermediary ballistic regime). While this single particle behavior in itself is already fascinating, the main focus of this work lies on the collective behavior of many interacting active particles, specifically on their motility induced phase separation (MIPS), which will be introduced in the next section.

### 3.3 Self-trapping and motility induced phase separation

ABPs serve as one particular example of an active system that undergoes phase separation at intermediary packing fractions and sufficient propulsion strengths. At first, this seems peculiar as there are no attractive interactions between particles that could drive phase separation analogously to an equilibrium gas-liquid transition. Rather the propulsion in combination with the interactions between particles (in the case of ABPs the excluded volume interactions) causes this behavior.

The corresponding mechanism is called self-trapping [20]. Following the explanation in [20], we illustrate this mechanism of cluster formation in ABPs using a simplified sketch, ignoring among others the passive diffusion, which is shown in Figure 3.2. The active motion of the particles is directed on time scales of the rotational diffusion time  $\tau_r = D_r^{-1}$ . If two particles happen to collide head on, they will block each other due to the volume exclusion. These particles can only move freely again when their orientation has changed sufficiently via rotational diffusion or when they escaped each other through passive translational diffusion. As these time scales are rather long compared to the propulsion time scale  $\sigma/v_0$  at sufficient propulsion strengths, other particles can in the meantime reach the building cluster and thus further obstruct the motion of the already trapped particles. At some point the orientation of the particles inside the cluster becomes irrelevant, as it is blocked from all sides by other particles which are either trapped themselves or if they are on the surface

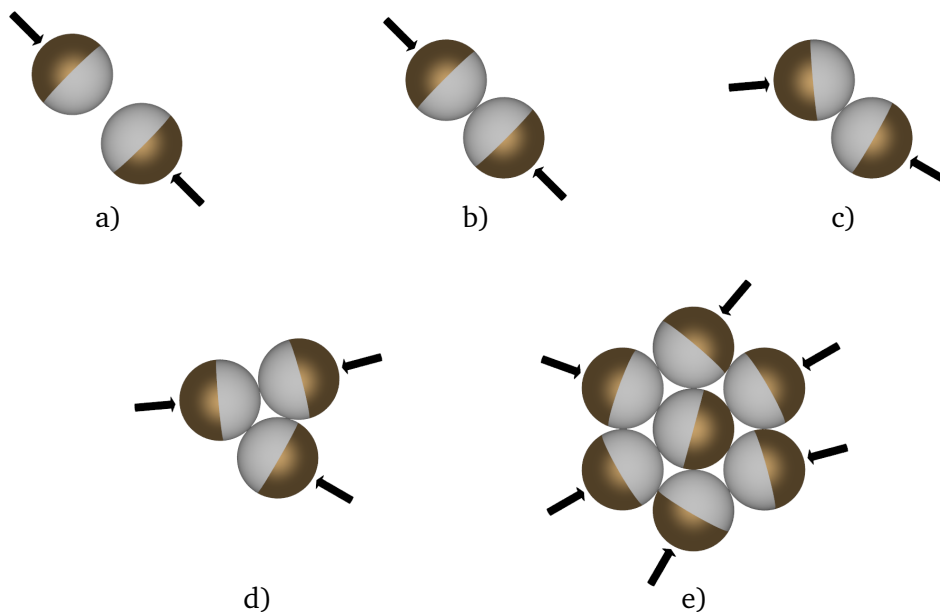


**Fig. 3.2.:** Sketch of the simplified mechanism behind cluster formation in ABPs [20]: Due to their persistent directed motion, two particles colliding head on (panel a)) will get trapped, pressing against each other (panel b)) until their propulsion direction and/or position has sufficiently changed via diffusion that they can escape (panel c)). However, in the meantime the blocked particles can work as a seed for a cluster, that can grow by other particles colliding with the building cluster (panel d)). If a cluster has grown sufficiently, there will be particles trapped inside the cluster by a shell of particles on the outside that is pushing inwards (panel e)).

are pushing inwards. The dependence on packing fraction and active propulsion becomes obvious, considering that the likelihood of other particles arriving at the cluster is dependent on the propulsion strength as well as the overall packing fraction of active particles in the system.

The surface polarization is demonstrated using a zoom of simulation snapshot in Figure 3.3. The snippet shows the interfacial region between a dense and a dilute phase. Orientations of particles are indicated both by arrows and by color code. Due to the orange coloring as well as by inspecting the individual arrows, one can easily see that there is a net orientation of the particles at the surface of the dense phase pointing inwards [42]. This layer of particles keeps the other particles inside the dense phase. It is also notable that other than on the surface there seems to be no orientational correlations but the orientations are random for particles not at the interface [42]. Obviously, the cluster will not grow indefinitely. Even though at finite packing fractions of the dilute phase, some particles will always crash into the interface thus adding to the dense phase, particles at the interface undergo rotational diffusion and by sufficiently changing their direction move away from the interface into the dilute phase. A steady state is reached if the rate of particles joining and escaping the cluster by those mechanisms offset. Assuming a straight

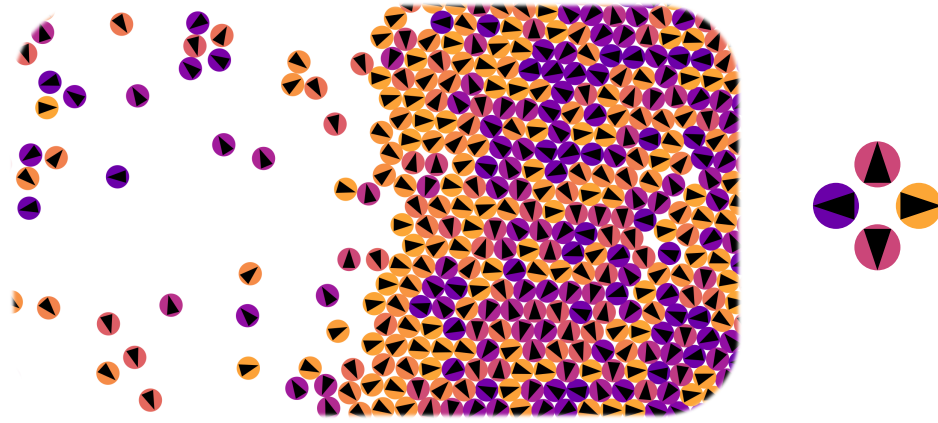


**Fig. 3.3.:** Polarization of ABPs at an interface: ABPs in the phase separating regime (i.e. at sufficiently high propulsion strengths and at intermediary packing fractions) form macroscopic clusters. These clusters are stabilized by an interfacial layer of particles whose orientation is polarized pointing inward. This can nicely be seen in this section of a simulation snapshot. The ABPs are shown as disks with the color code shown on the right and individual arrowheads indicating their orientation. While there is no preferred orientation in either bulk phase, there is a net polarization pointing towards the dense phase at the interface.

interface, Redner et al. [104] showed that for active particles with attraction this theoretical argument indeed matches their numerical results at least qualitatively.

In addition to these more qualitative considerations, there have been studies trying to understand nucleation in ABPs more quantitatively. Applying an approach analogous to classical nucleation theory, Redner et al. [103] tried to understand the dynamics of how dense clusters and eventually the dense phase form. Their theory is able to predict the dilute binodal and the density dependence of the cluster size distribution at least to some degree. Richard et al. [107] also studied the kinetics of nucleation as well as the microscopic pathway that is involved in nucleation after a quench starting in a homogeneous system. Complementing brute force BD simulations with forward flux sampling, they determined precise nucleation rates even for comparably small supersaturations. Consequently, they were able to determine, that the cluster size is not sufficient as a reaction coordinate but that the surface polarization plays a non-negligible role as well.

In general, both self-propulsion and some form of interaction are needed for collective behavior to arise. Phase separation in self-propelled particles cannot only arise due to excluded volume interactions. Rather, a density dependent swimming speed of otherwise ideal self-propelled agents can already give rise to phase separation into a dense and a dilute phase [133, 22, 138]. In fact the effective velocity of ABPs, meaning the average distance traveled per time projected onto each particle's respective orientation, has been shown to decay roughly linearly with increasing density [133]. Qualitatively, the two mechanisms, namely explicitly reducing the

propulsion strength at increased local density, as well as blocking via excluded volume interactions, seem to match [133, 22, 138]. The phase separation arising due to aggregation of particles in the dense areas with effectively reduced swimming speed is called MIPS [94]. Such a MIPS is present not only in ABPs but also in a variety of other systems. Regardless of the qualitative similarities between ABPs and ideal active particles with an artificial density dependent swim speed, they do not produce the same phase behavior quantitatively. This can be easily understood, as the density dependent swim speed effectively reduces the pair-wise interactions of ABPs to a mean-field type of interaction with the averaged density field [22]. Therefore, even introduction of additional terms, such as density gradients, will not quantitatively reproduce the phase behavior of standard ABPs. We thus have to numerically solve the equations of motions for ABPs to obtain accurate results for their phase behavior.

### 3.4 Interaction potential and effective diameter

There exist several concrete implementations of ABPs in literature differing in the specific details of the model [42, 104, 20, 125, 11, 134, 167, 121]. One of the distinctions between implementations lies in the interaction potential which models the (nearly) hard core repulsion between different particles. Generally, the interaction is a simple, isotropic pair potential acting on all pairs of particles:

$$U(\{\mathbf{x}_i\}) = \sum_{i < j} u(|\mathbf{x}_j - \mathbf{x}_i|). \quad (3.3)$$

While some studies use a steep and shifted potential of a Yukawa type [9, 167], the most common choice is to use a potential of LJ type that is cut at its minimum and shifted to zero at the cut-off, which is named after Weeks, Chandler, and Anderson [153]:

$$u(r) = \begin{cases} 4\epsilon \left( \left(\frac{\sigma}{r}\right)^{12} - \left(\frac{\sigma}{r}\right)^6 + \frac{1}{4} \right) & r < 2^{1/6}\sigma \\ 0 & \text{otherwise.} \end{cases} \quad (3.4)$$

The diameter of the particles is then of the order of the parameter  $\sigma$ , which is thus customary used as the unit of length. The other parameter  $\epsilon$  sets the strength of the repulsion. Its effect is demonstrated in Figure 3.4. In the case of  $\epsilon = 1$ , shown in blue, the repulsion is still comparably weak and allows for a significant overlap. Therefore, in this work a value of  $\epsilon = 100$  is used. Here, the possible overlap is drastically reduced, cf. Figure 3.4 (orange curve).

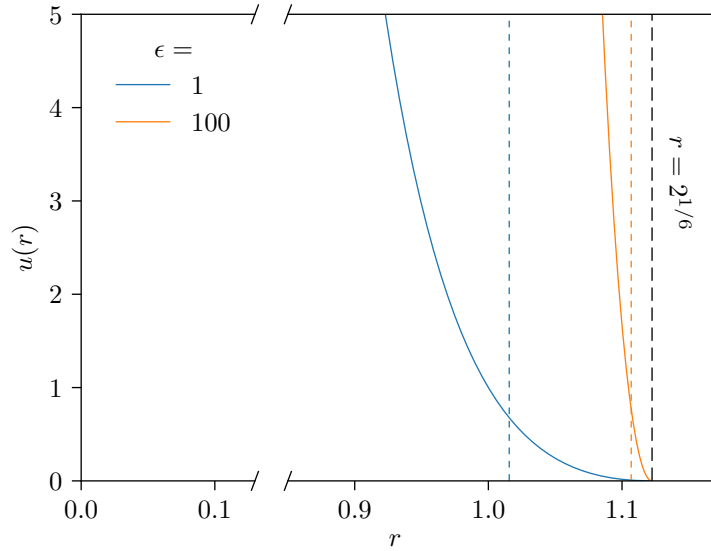


**Fig. 3.4.:** Plot of the WCA potential [153] for different values of interaction strength  $\epsilon$ . The potential and the corresponding effective diameter are shown as full and dotted lines respectively. The cutoff radius  $r_{\text{cut}} = 2^{1/6}$  is indicated by a dashed vertical black line. In this work, particles are modeled as nearly-hard disks and spheres. To prevent large overlaps,  $\epsilon = 100$  is chosen.

Obviously,  $\sigma$  cannot correspond to the true diameter of the particles, mapping them onto hard disks, as potentials differing in the energy scale  $\epsilon$  allow for significantly different overlaps. To allow for a more general description and comparison between different parameter sets and even potential forms, it is instructive to compute an effective diameter of the particles. In thermodynamic equilibrium, such a mapping on actual hard disks can be done via the Barker-Henderson diameter [5], which is computed as:

$$d_{\text{BH}} = \int_0^{2^{1/6}} dr (1 - \exp(-u(r))). \quad (3.5)$$

Figure 3.4 shows the effective diameters for the different parameter sets as dashed vertical lines using the same colors as for the respective potential. In case of the potential used in this work ( $\epsilon = 100$ ), the resulting effective diameter is given by  $d_{\text{BH}} \approx 1.10688$ . Fundamentally, this effective diameter is only valid in the equilibrium case of passive particles ( $v_0 = 0$ ) where only thermal fluctuations can cause particle overlap, whereas it does not hold generally in the more intense active case ( $v_0 \gg 0$ ) in which particles can be driven into each other by opposing active propulsions [134]. In our case of the strongly repulsive WCA potential, we neglect the resulting deviations in the non-equilibrium case, as the repulsive force  $-\partial_r u(r)$  balances out a high active propulsion (e.g.  $v_0 = 160$ ) already for distances  $r \approx d_{\text{BH}}$ .

Other groups have chosen a different approach, e.g. Stenhammar et al. [134]. Due to the much weaker repulsion ( $\epsilon = 1$ ) in their model, a high active propulsion would

distort the diameter drastically. They thus chose to vary the propulsion not via its strength but by tuning the temperature  $k_B T$  and thus  $D_r$  while keeping  $v_0$  fixed. To allow for comparison between those different cases, we measure the propulsion's strength not by its absolute value  $v_0$  but by the dimensionless Peclet number

$$\text{Pe} = \frac{3v_0}{d_{\text{BH}}D_r}. \quad (3.6)$$

## 3.5 Numerical integration

In Section 2.1.4 an integration scheme for passive BD was introduced. In case of ABPs, this scheme cannot be applied directly, as it does not account for the active propulsion. In this work, the following integration schemes were applied.

### 3.5.1 Euler

The simplest way to numerically solve Eq. (3.1) is via an Euler-scheme. The passive version shown in Equation (2.8) has to be extended to account for the active propulsion, though. This results in the following update rules:

$$\mathbf{x}(t + \delta t) = \mathbf{x}(t) + \left( -\frac{D}{k_B T} \nabla V(\mathbf{x}(t)) + v_0 \hat{\mathbf{e}}(t) \right) \delta t + \sqrt{2D\delta t} \mathbf{R}(t), \quad (3.7)$$

where the highlighted term (cf. Eq (2.8)) adds the active propulsion. As the rotational dynamics remain unchanged in between active and passive Brownian particles, the passive version of the update rules for  $\hat{\mathbf{e}}(T)$  remain valid.

### 3.5.2 Predictor-corrector method

The Euler-scheme is of low order of convergence [71, 17, 16]. As the potentials  $U(\mathbf{x})$  used in this work are very steep which results in very large forces, a very small time step  $\delta t$  has to be used to even reach stability and eventually convergence. To achieve this without the necessity of such very small time steps, in some parts of this work a weak second order predictor corrector scheme [71, p. 505f] is used instead of the Euler scheme. Specifically, it is applied in Chapter 7, Section 8.5, and in Appendix A.2. Comparably to Runge-Kutta schemes for non-stochastic differential equations, the force  $\nabla U(\mathbf{x}(t))$  is not assumed to be approximately constant between



$\mathbf{x}(t)$  and  $\mathbf{x}(t + \delta t)$  but its value is corrected by computing the mean of the force  $\nabla U(\mathbf{x}(t))$  and the force at a predictor position  $\bar{\mathbf{x}}(t + \delta t)$ ,  $\nabla U(\bar{\mathbf{x}}(t + \delta t))$ :

$$\begin{aligned}\mathbf{x}(t + \delta t) &= \mathbf{x}(t) + \left( -\frac{D}{2k_{\text{B}}T} (\nabla U(\mathbf{x}(t)) + \nabla U(\bar{\mathbf{x}}(t + \delta t))) + v_0 \hat{\mathbf{e}}(t) \right) \delta t + \sqrt{2D\delta t} \mathbf{R}(t), \\ \phi(t + \delta t) &= \phi(t) + \sqrt{2D_r \delta t} R_r(t).\end{aligned}\tag{3.8}$$

The predictor  $\bar{\mathbf{x}}(t + \delta t)$  is computed using the average of the original force  $\nabla U(\mathbf{x}(t))$  and the force at another predictor value of the positions  $\tilde{\mathbf{x}}(t + \delta t)$ :

$$\bar{\mathbf{x}}(t + \delta t) = \mathbf{x}(t) + \left( -\frac{D}{2k_{\text{B}}T} (\nabla U(\mathbf{x}(t)) + \nabla U(\tilde{\mathbf{x}}(t + \delta t))) + v_0 \hat{\mathbf{e}}(t) \right) \delta t + \sqrt{2D\delta t} \mathbf{R}(t).\tag{3.9}$$

This predictor  $\tilde{\mathbf{x}}(t + \delta t)$  is then simply determined by using the Euler scheme:

$$\tilde{\mathbf{x}}(t + \delta t) = \mathbf{x}(t) + \left( -\frac{D}{k_{\text{B}}T} \nabla U(\mathbf{x}(t)) + v_0 \hat{\mathbf{e}}(t) \right) \delta t + \sqrt{2D\delta t} \mathbf{R}(t).\tag{3.10}$$

At first glance, this scheme may seem much more expensive than its Euler counterpart as it is necessary to compute all forces at three different sets of positions, namely  $\mathbf{x}(t)$ ,  $\bar{\mathbf{x}}(t + \delta t)$ , and  $\tilde{\mathbf{x}}(t + \delta t)$  for every pair of interacting particles at every time step. Force computation is the computational bottle neck in our and for that matter also in most other simulations, such that a predictor-corrector step will take roughly three times as long as an Euler step. However, in many cases, especially if we are interested in rather slow converging properties, the predictor-corrector scheme allows for much larger time steps than the Euler scheme. As long as the factor in the time step at least counter balances the increase in computational time per step in the predictor-corrector integrator, it will actually run faster than the simple Euler integration. Unfortunately, no significant speed-up is gained in case of active Brownian particles though. Throughout the thesis,  $\delta t_{\text{Euler}} = 1 - 2 \cdot 10^{-6}$  is used as a time step for the Euler integrator. This step is sufficient to reach convergence for all quantities that were evaluated in this thesis. The only quantity for which convergence was not fully reached was the configurational temperature which especially for high propulsion strengths was particularly sensitive to the time step due to its dependence on the specific overlap of particle pairs. For the predictor-corrector scheme,  $\delta t_{\text{PC}} = 5 \cdot 10^{-6}$  is used. For this time step even the configurational temperature is well converged for sufficiently low Pe. In conclusion, the computational effort for both schemes is very similar, possibly even being slightly in favor of the Euler scheme for all quantities that are studied in this work. Therefore, this scheme is used in all but the three sections listed above.



## Phase behavior in two dimensions

Phase separation in ABPs, as described in Section 3.3, closely resembles a gas-liquid transition in an equilibrium fluid [133, 8]. Rather than to rely on this qualitative observation, we want to quantify the transition and determine whether concepts known from the corresponding equilibrium phase transitions still hold in this setting far from equilibrium. As a first step, it is imperative to study the exact position of the transition region in the phase diagram. There have been some previous studies, that have studied this question [104, 134, 43, 125]. Nonetheless, additional work is needed, as none of the previous studies examined the influence of finite system size on their estimates for the transition region. In this chapter, we will discuss our high-accuracy estimates for the position of the non-equilibrium analog of binodal lines in ABPs. The contents of this chapter are mainly a recapitulation of material published in Refs. [11, 121].

### 4.1 Finite size transitions

In the analogy of the phase separation of ABPs to a gas-liquid transition in equilibrium, the propulsion strength plays the role of inverse temperature [133]. Above a certain critical propulsion strength  $Pe > Pe_{cr}$  there is a region at intermediary packing fractions, i.e. between the binodal lines, where a system of infinite size phase separates into a dense (liquid-like) and a dilute (gas-like) phase. In a finite size system such as the ones that can be studied by computer simulations the situation becomes more complicated. The transition packing fractions lie inside the binodal lines with positions depending on both boundary condition and system size. In the most commonly used geometry, namely a rectangular box with periodic boundary conditions, the system undergoes a series of finite size transitions for increasing the density at constant  $Pe > Pe_{cr}$  that very closely match those seen in an equilibrium evaporation-condensation transition [80, 165, 116, 14].

Exemplary snapshots of the finite size transitions in ABPs are presented in Figure 4.1. Starting in the dilute gas-like phase, an increase in packing fraction even above the binodal line does not directly lead to a phase separated steady state. The system rather stays homogeneous to avoid the creation of interfaces. At a sufficiently high (system-size and geometry dependent) packing fraction, the system phase

separates by forming a finite liquid droplet. Further increase of the packing fraction leads to growth of the droplet until it connects with itself over one of the periodic boundaries, which leads to the formation of a slab geometry. Symmetrically but with inverted roles of the dense and dilute phase, a continued increase of the packing fraction results in a dense liquid-like system containing a dilute gas-like bubble. The bubble's size shrinks now for increasing packing fraction until the system becomes homogeneous (again inside of the binodal line).

The dilute phase very closely resembles an equilibrium gas phase. The dense phase on the other hand is extremely dense, nearly reaching close packing at high velocities. Also, the particles in the dense phase show a high degree of local hexagonal order. Still it is more appropriate to talk about a liquid-like and not about a solid-like phase, as the locally ordered grains (cf. Figure 4.1) do not show a tendency to merge but have a rather short lifetime while constantly reorganizing.

## 4.2 Determination of binodal densities

Our goal is to determine the exact position of the binodal lines. Obviously, the simple detection of nucleation events does not allow to determine the boundaries within which phase separation is stable in a bulk system as their occurrence depends on system size and geometry. Even the system-size dependent boundaries are hard to determine, as nucleation events will depend on the waiting time as well. We thus employ the method of choice from equilibrium physics, namely the determination of coexisting densities in a phase separated state [152]. To apply this method, it is important, though, to ensure that the system is in a slab geometry. In the case of droplet and bubble the curved interfaces cause a Laplace pressure which in turn causes the packing fractions to differ from those in a bulk system. The straightness of the interfaces in a slab geometry mitigates this problem such that the measured densities inside of a slab at sufficient distance of the interfaces converge to the bulk densities that we are interested in [152, 142].

To ensure stability of the slab and its orientation, we simulate an elongated box of side length ratio 1 : 2. Minimization of the interface then results in the slab always aligning with the short axis of the system. Aside from being beneficial by stabilizing the slab, the fact that its orientation is also fixed is another important upside as it causes the system to keep a continuous symmetry along the short axis throughout the simulation. This results in a greatly simplified methodology to extract the coexisting densities and thereby the determination of the binodal lines which will be explained below. We simulate at an intermediate overall packing fraction of  $\phi = 0.5$ . Note, however, that this value, as long as it is well within the stability region of the slab

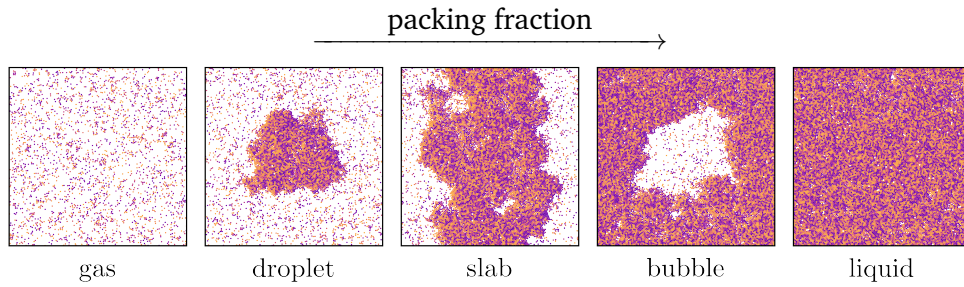


**Fig. 4.1.:** Snapshots of finite size transitions: In the phase separating regime (i.e. at sufficiently high propulsion strength), ABPs in a finite system with periodic boundary conditions undergo finite size transition similar to an equilibrium phase transition when the packing fraction is increased. Starting in the gaseous phase, at first a liquid droplet will appear. When the droplet is connecting with itself over the periodic boundary, a slab is formed. For sufficiently high packing fractions, this will turn into a gaseous bubble that shrinks until only pure liquid is left. (Parameters:  $Pe \approx 111$ ,  $\phi = 0.15, 0.3, 0.6, 0.75, 0.9$  going from left to right, Adapted from Figure 2 of Reference [121] for ABPs)

geometry, is not important. It does not affect the bulk densities but only the relative widths of the dense and dilute slab.

By measuring the coexisting densities in the resulting slab geometry at different propulsion strengths  $Pe$ , we can then extract the binodal densities. Each simulation is used to determine the densities of the dense and the dilute slab which, in turn, both give one point on the respective binodal at the simulated  $Pe$ . An exemplary snapshot is shown in the upper panel of Figure 4.2. By shifting the COM to zero along the elongated direction, the coexisting densities can simply be extracted by determination of the density distribution along this direction in form of a histogram with bins perpendicular to said direction and thus parallel to the slab. Note, that in computing the COM, the periodicity of the system has to be accounted for [3]. In the lower panel of Figure 4.2 the resulting averaged density distribution is shown as open blue circles. The dense phase even in the homogeneous region shows large fluctuations which result in bubbles and small rifts. In case of the slab geometry this can even lead to the slab ripping open especially close to the critical region. As these features arise not because of the slab geometry but are inherent properties of the dense phase, they are not excluded from the analysis but simply averaged over as part of the bulk-like dense phase. Nonetheless, this increases the need for additional sampling as the impurities can be comparably long-living.

For systems far from criticality, such as the one shown in the lower panel of Figure 4.2, the packing fractions can basically be read of as the plateau values that are constant over wide intervals along the  $x$  direction. Closer to criticality, the width of the interfacial regions increases and thus the width of the plateau intervals decreases. To allow for a more reliable extraction of the plateau values, which also makes use

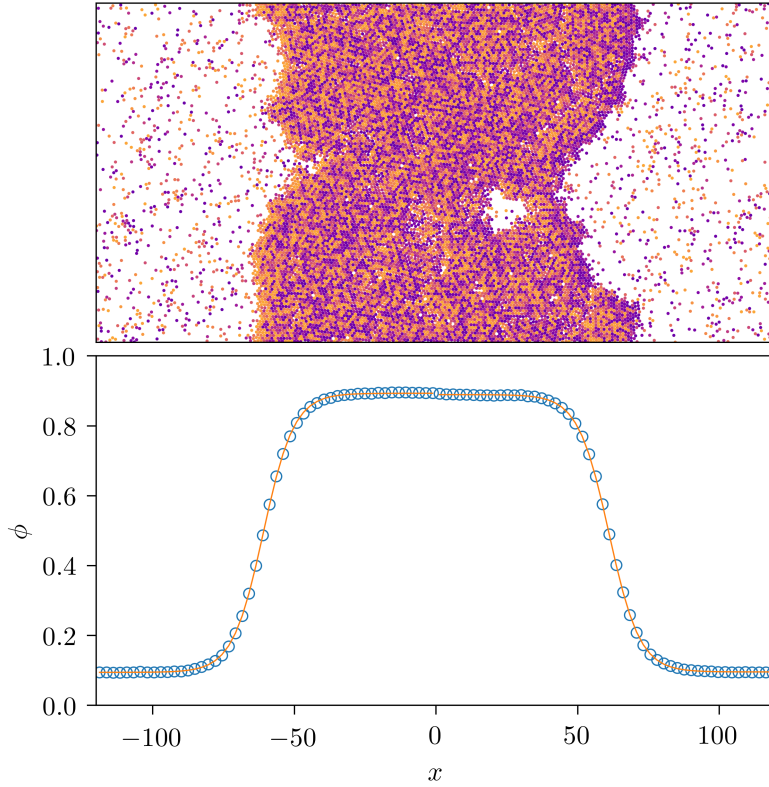


**Fig. 4.2.:** Packing fraction distribution in a slab geometry (Adapted Fig. 3 of Ref. [121] for ABPs): *Top:* To extract binodal packing fractions, a system at intermediary packing fraction is simulated in an elongated box, which will result in a slab geometry. *Bottom:* The packing fraction's distribution in bins perpendicular to the longer axis is averaged over time, always shifting the center of mass (COM) along said axis to 0. The resulting curve is shown as open circles. By fitting both the positive and the negative branch of the distribution with a hyperbolic tangent (cf. Eq. (4.1)), the coexisting bulk packing fractions can be extracted. ( $Pe \approx 177$ )

of the information of the interfacial region, we fit the distributions with a hyperbolic tangent (which already proved very successful in equilibrium systems [152]):

$$\phi(x) = \frac{\phi_{\text{liq.}} + \phi_{\text{gas.}}}{2} + \frac{\phi_{\text{liq.}} - \phi_{\text{gas.}}}{2} \tanh\left(\frac{x - x_0}{2\omega}\right). \quad (4.1)$$

The density distribution is then fitted with this function for the positive and negative  $x$  interval independently. For each side one has to determine four fit parameters. Aside from the coexisting densities  $\phi_{\text{liq.}}$  and  $\phi_{\text{gas.}}$ , that we extract, the position of the interface  $x_0$  and the width of the interface  $\omega$  have to be fitted. The fitting procedure, as well as the comparison of the results of the positive and negative sides for each distribution, can already give some indication of associated uncertainties. Nonetheless, it is much more reliable to do multiple independent runs and then to determine the uncertainty of the resulting mean by their spread. By doing so for propulsion strengths  $55 < Pe < 180$  the phase diagram was extracted. The result can be seen in Figure 4.3.

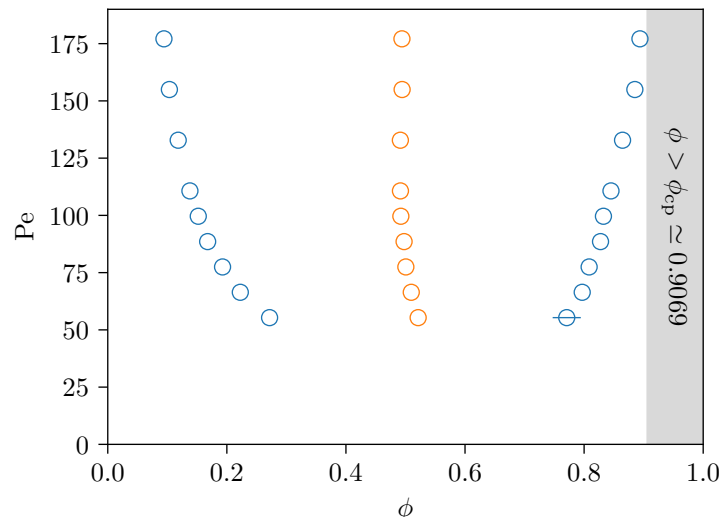


**Fig. 4.3.:** Phase diagram of ABPs in 2D: The binodals (open blue circles) are determined by extracting coexisting densities from a slab geometry [11]. Packing fractions that are bigger than close packing are obviously geometrically impossible (indicated by the shaded grey area [37]). Even though for high propulsion strengths the binodals approach this limit, it is never reached. Due to an increase of the interfacial width as well as more drastic fluctuations, the uncertainties especially of the dense branch grow for propulsion strengths closer to the critical point. The uncertainties are only explicitly shown if they exceed the symbol size though. The empirical law of rectilinear diameter (open orange circles) seems to be valid only far from criticality ( $Pe \gtrsim 100$ ) where the midpoints start to deviate from a line closer to criticality. This is in accordance with other active systems [101, 141, 143].

The extracted binodal densities are shown as open blue circles. The corresponding uncertainties are only indicated if they are larger than the symbol size. The range of possible values for the packing fraction ranges from 0 to close packing ( $\phi_{cp} = 0.9069$  [37]), which is the highest packing fraction of hard disks that can be achieved on an infinite surface. The claim that true binodal densities can be extracted by this method is corroborated by the study of different system sizes, shown in Reference [11] using data provided by Julian Bialké. For all propulsion strengths, a decrease in system size by a factor of two does result in the same phase boundaries. Larger systems are needed though, to reach smaller propulsion strength because of the increased interfacial widths in that regime.

### 4.3 Rectilinear diameter

In equilibrium gas-liquid transitions, the binodal densities have been observed to follow the empirical law of rectilinear diameter, which states that the mean packing

fractions for pairs of points on the binodal lines at different temperatures fall onto a line [105, 152, 24]:

$$\frac{\phi_{\text{liq.}} + \phi_{\text{gas.}}}{2} \propto T. \quad (4.2)$$

Even though the law is only empirical, lacking a strict theoretical derivation, it has been observed to at least approximately hold even for points close to criticality in a variety of different systems undergoing a gas-liquid transition. The examples range from various experimental measurements in different systems [24, 172] to a variety of model systems that are studied via computer simulations [66, 152]. In non-equilibrium, the situation is different. Studies for active systems undergoing gas-liquid transitions but featuring an underlying equilibrium phase transition, e.g. active LJ [101] or Asakura-Osawa [141, 143] systems have shown that for increasing activity, these systems show growing deviations of the linear behavior especially in the vicinity of the critical point. Subtle deviations from the linear behavior in close vicinity to the critical point are found in equilibrium systems as well [172, 155]. However, the deviations found in the referenced non-equilibrium systems are much more pronounced and persist farther from criticality.

For our system, featuring a purely non-equilibrium transition without a passive counterpart, we also see a rather large deviation of the linear behavior close to the critical point. The mean of coexisting densities for all pairs of points on the binodal lines, that were computed, are shown as orange circles in Fig. 4.3. For large propulsion strengths and thus far away from the critical region, the linear approximation in Eq. (4.2) still holds very well. But for smaller propulsion strengths, the mean strongly shifts towards higher packing fractions, indicating a violation of the law of rectilinear behavior in ABPs. This fact is not only interesting in its own right, but it also hints at additional difficulties in determining the critical packing fraction, as it will not simply lie on the extension of the diameter (see Chapter 7).



## Pressure and interfacial tension

In the previous chapter, the binodal densities of ABPs have been determined. In this chapter, we will turn towards another important quantity, namely the pressure. Mechanically, pressure can be defined as the force per area on a wall that is confining a system. But whereas this definition coincides with its definition as a derivative of a free energy with respect to the system's volume in equilibrium, this does not necessarily hold true in our non-equilibrium setting [130]. Nonetheless, the availability of a mechanical definition makes the pressure an excellent quantity to study in systems far from equilibrium. As a result there have been several studies trying to quantify and understand the behavior of the pressure in active systems [76, 166, 83, 169, 139, 49, 125, 126, 91, 163]. One of the important properties of the pressure in equilibrium is that it is intensive. Therefore, in equilibrium, it is constant throughout a large system. It is the goal of this chapter to check whether versions of an active pressure that have been recently defined [169, 139, 49, 125, 126] show a similar behavior and by that can be considered to be analogous to pressure definitions in equilibrium. For the most part, the content of this chapter has been published in Ref. [11].

### 5.1 Definition of an active pressure

In equilibrium, the pressure tensor in a system with periodic boundaries and thus without confining walls can be measured as (using the conventional unit system introduced in Section 3.4):

$$p_{\text{eq.}} = \rho \cdot \mathbb{1} + \sigma_{\text{eq.}}, \quad (5.1)$$

where  $\rho$  is the number density and  $\sigma_{\text{eq.}}$  is the (equilibrium) diagonal stress tensor of an unshered system, which in turn can be computed by measuring the virial:

$$\sigma_{\text{eq.}} = - \frac{\langle \sum_{i < j} \mathbf{r}_{ij} (\nabla U(r_{ij}))^T \rangle}{A}. \quad (5.2)$$

Here, the sum iterates over all pairs of particles. Their respective distances are given by  $r_{ij}$ , the system's area is denoted as  $A$ . In an isotropic system, the stress tensor and thus the pressure tensor is diagonal and all diagonal components share the same value. Said value corresponds to the virial part of the pressure, which together with the ideal part of the pressure is the full thermodynamic pressure in equilibrium.

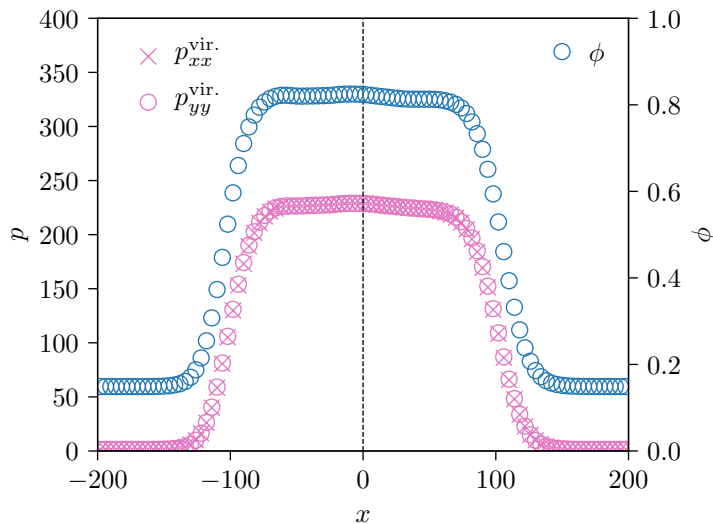


**Fig. 5.1.:** Distribution of the virial pressure in a phase separated slab geometry: The blue curve shows the distribution of the packing fraction in bins parallel to the slab (equivalent to Figure 4.2). Studying the  $xx$  and  $yy$  components of the virial pressure tensor known from equilibrium gives the pink curves. Obviously, there is a large imbalance between the high virial pressure within the dense region and the negligible pressure in the dilute slab. Intuitively, there has to be another pressure contribution counterbalancing the differences in the virial pressure, as otherwise the phase separation should not be stable.

In a phase separated system, isotropy is broken. Nonetheless, in the bulk parts of the system, locally, there is no anisotropy and thus only in the interfacial region there exists a direction dependence and hence difference between the diagonal components of the pressure tensor, which is linked to the interfacial tension.

The simple pressure definition given in Eq. (5.1) is not intensive in the case of ABPs though. Studying the pressure in a phase separated system, yields decidedly different results in the dense and dilute phases. While it is negligible in the dilute gas-like phase due to the few interactions between the freely moving particles, the particles in the dense liquid-like phase are interacting heavily with their neighbors resulting in a large virial pressure. To verify and highlight this imbalance, Figure 5.1 shows the distribution of the virial contribution to the pressure in a phase separated slab geometry. In this system with a geometry equivalent to that used in the determination of the binodal densities, the figure shows the average packing fraction and the diagonal components of the virial pressure, measured in bins that are aligned parallel to the slab. Each pairs' contribution is assigned half to the bins in which the monomers are located. While this assignment to bins is somewhat arbitrary and in fact might influence the result, it does not distort the qualitative effect and more importantly, does not change the integrated pressure, which we will study later [150]. Therefore, we do not further study the influence of the binning method but directly turn to the results shown in Figure 5.1. Unsurprisingly, both

diagonal components lie on top of each other and show a drastic difference between a near zero value in the dilute region ( $|x| \gtrsim 150$ ) and a large value within the bulk of the dense slab ( $|x| \lesssim 50$ ). Obviously, there has to be another contribution counteracting this drastic imbalance. Without that, such a large inhomogeneity in the pressure would otherwise lead to an instable system. A non-zero pressure gradient would cause a force, which in turn would drive particles from the dense high-pressure into the dilute low-pressure region and thus would obstruct the phase separation. This is prevented by an additional stress contribution caused by the active propulsion of the particles. As pointed out in Reference [139], the existence of such a contribution becomes evident considering the effect of confining a system of self-propelled particles by walls. By exerting a pressure, the walls prevent the particles from being propelled out of the box. This pressure corresponds to the swim pressure of the particles [139].

In recent literature, there have been several different approaches to derive the form of this stress and pressure contribution caused by the activity. Takatori et al. [139] and Yang et al. [169] based their definition on the observation, that the propulsion velocity can be interpreted as a propulsion force instead:

$$\mathbf{F}_{\text{act}} = \underbrace{\left(\frac{k_{\text{B}}T}{D}\right)}_1 v_0. \quad (5.3)$$

In principle, microswimmers at low Reynolds numbers are force free, meaning that there is no net force causing them to swim. This active force, however, would correspond to the force that would be needed to prevent an active swimmer from moving, e.g. by fixing it using an optical tweezer [139]. Furthermore, ABPs themselves do not obey the momentum conservation, that is basis of the force free swimming anyway, as the solvent and in turn hydrodynamic interactions are not considered. Thus, in some publications, ABPs have been described as “dry” active matter [85] even though they strive to describe particles moving in a solvent nonetheless [129]. Regardless of this question, one can derive an active stress for the non-equilibrium model system of ABPs as the first moment of the active force as defined in Eq. (5.3) [169, 139]:

$$\sigma_{\text{act.}} = -\frac{\langle \sum_i \mathbf{x}_i \cdot (v_0 \hat{\mathbf{e}}_i)^T \rangle}{2V}. \quad (5.4)$$

This definition of an active stress has a striking structural resemblance to the equilibrium part (see Eq. (5.2)). Note, however, that here the summation is done not over pairs of particles, but over single particles instead. Furthermore,  $\mathbf{x}_i$  corresponds to the absolute position of the particles, meaning that it is not reset when crossing a periodic boundary. Analogously to the equilibrium stress, the active stress is diagonal and in a homogeneous system the diagonal entries share the same value. Adding this

active contribution to the pressure results in the following definition of the pressure in an active system:

$$p_{\text{act.}} = \rho + \sigma_{\text{eq.}} + \sigma_{\text{act.}} \quad (5.5)$$

An alternative derivation of the active pressure by Solon et al. [125] focuses on the force, a system of active particles would exert on a wall by studying the time evolution of the fluctuating distribution function. Nonetheless, this derivation, which more closely follows the idea of the mechanical definition of the pressure, gives the same result.

## 5.2 Simulations

To check the validity of this pressure definition, namely its intensiveness, computer simulations are performed. Equivalently to the previous simulations, WCA-particles with  $\epsilon = 100$  are studied. However, for consistency with previous publications of the other authors of the corresponding paper [11], a different unit of length is chosen. Lengths are measured in units of the cut-off radius, which is much closer to the effective diameter than  $\sigma$ . This results in  $\sigma = 2^{-1/6}$  and an effective diameter of  $d_{\text{BH}} = 0.986$ . Also, the rotational diffusion constant is chosen to be  $D_r = 3$ . Note, that these model parameters and this unit system are only used in this chapter of the thesis.

To study the pressure distributions in a phase separated state, we again simulate an elongated box. It turns out that especially the active pressure relaxes to its bulk value very slowly in the vicinity of interfaces. Therefore, a large system with side lengths  $L_x = 2L_y = 400$  containing  $N = 52386$  particles was chosen. After relaxation, the system was binned along the  $x$ -axis. The resulting bins are thus parallel to the slab. Again, before particles are assigned to bins, the center of mass is shifted to zero such that as far as the binning is concerned the position of the slab is always at the same position. Analogously to the density distributions used for the determination of the binodals, the pressure distributions can thus be averaged over to get the distribution in both phases as well as the interface area.

The virial pressure tensor's distribution is measured as:

$$p^{\text{vir.}}(x) = \frac{1}{2A} \langle r_{ij} (-\nabla U(r_{ij}))^T \rangle_x \quad (5.6)$$

As already pointed out above, there exists a certain ambiguity here, as the virial pressure is given by an average over pairs of particles and it is not well-defined to which bin each contribution should be assigned. As all possible assignments effectively result in the same integrated pressure [150], the specific choice is not too

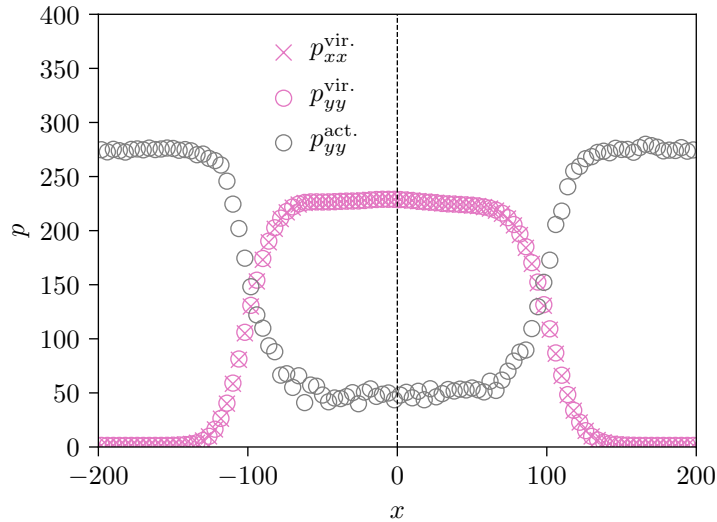


**Fig. 5.2.:** Plot of the pressure component distributions in bins parallel to the slab (Adapted from Figure 3a) of Reference [11]): As shown in Figure 5.1, the virial pressure shows a large imbalance between the dense and the dilute region. In grey, the active pressure as defined in Eq. (5.5) is shown. As particles can move nearly unobstructed in the dilute region, whereas they are strongly hindered to propel in the dense region, it shows the opposite tendency. The activity's contribution to the pressure is very large in the dilute region and strongly dampened in the dense slab. Therefore, this contribution offsets the imbalance in the virial pressure contribution.

important, though. Here, each pair's contribution is assigned in equal parts to the bins containing the two endpoints. Therefore,  $\langle \cdot \rangle_x$  denotes an average over all pairs of particles  $i, j$  where either particle  $i$  or particle  $j$  lies within the respective bin. The factor  $\frac{1}{2}$  accounts for the fact that otherwise, each pair of particles would be counted twice.

In case of the active pressure, no such ambiguity arises. As it is given by a sum over single particles, the assignment to bins is straightforward:

$$p^{\text{act.}}(x) = \frac{1}{A} \left\langle \sum_{\text{bin}} \mathbf{x}_i (v_0 \hat{\mathbf{e}}_i)^T \right\rangle. \quad (5.7)$$

Here, the summation runs over all particles in the respective bin. As in equation (5.4)  $\mathbf{x}_i$  represents the absolute position (disregarding periodic boundaries). Essentially, for computing the active pressure, the winding number along each periodic boundary has to be stored and used for “unwrapping” the coordinates before the active pressure is computed.

Figure 5.2 shows the distribution of the diagonal components of the virial as well as the  $yy$  component of the active pressure contribution. In addition to those contributions, there is still an ideal gas contribution. It is of order one though and

thus very small in comparison to the other parts that are of order 300. Therefore, it would overlap with the  $x$ -axis of the plot and thus is not shown. Studying the distributions of the different contributions, we can see that the active pressure as defined by [169, 139, 49, 125, 126] indeed counterbalances the large differences in the virial pressure between the dense and the dilute phase. Due to their nearly unhindered motion in the dilute region, the particle's position is strongly correlated to the direction of their propulsion, leading to a high active pressure  $p_{yy}^{\text{act.}} \approx 275$ . In the dense phase, the particles are frequently blocked and thus the correlation between orientation and position is strongly diminished. Therefore, the activity's contribution to the pressure is much smaller  $p_{yy}^{\text{act.}} \approx 50$ .

Independently of the absolute values, one notes that the relative fluctuations of the active pressure contribution especially in the dense but also in the dilute region are much larger than those of the virial contribution. Additionally, the variance is not constant during the simulation. Due to the dependence on the absolute position, the variance of each particles contribution and thus of the active component of the pressure grows with growing mean square displacement of the particles. Furthermore, the exact growth rate of the variance is unknown, as it strongly depends on the history of the particle's movements, e.g. the time it spend in the dense and the dilute regions. This does both increase the simulation time needed to enhance the statistical accuracy and make the estimation of an associated uncertainty difficult. As gathering statistics is becoming more and more difficult with increasing simulation time, data averaged over 25 independent runs is taken to investigate the pressure distributions. While this is giving sufficiently accurate results in our case, there is recent work by others to find a local definition of the pressure that is independent of the absolute position [130] or an equation of state relating the pressure to bulk properties of the system [139, 126, 138] and thus to allow for easier measurement.

Regardless of those difficulties, the distributions of the pressure components and consequently the total pressure could be determined with sufficient accuracy. The total pressure's  $yy$  (e.g. tangential) component  $p_{yy}^{\text{tot.}}$  including all three contributions (ideal, virial, and active) is shown in Figure 5.3. The open circles indicate the results in the respective bins, while the horizontal line gives our estimate for the bulk pressure. The corresponding average is taken over all bins considered to be in the bulk regions of both slabs. To be sufficiently sure that the interfacial region is excluded, we only took the areas indicated by gray shading into account. This results in half of the box being considered to be bulk whereas the other half being considered to contain the interface.

The first thing to note is that the total pressure as defined in Equation (5.5) coincides in both the dense and the dilute region. The averaged bulk pressure of  $p_{yy}^{\text{tot.}} \approx 276$

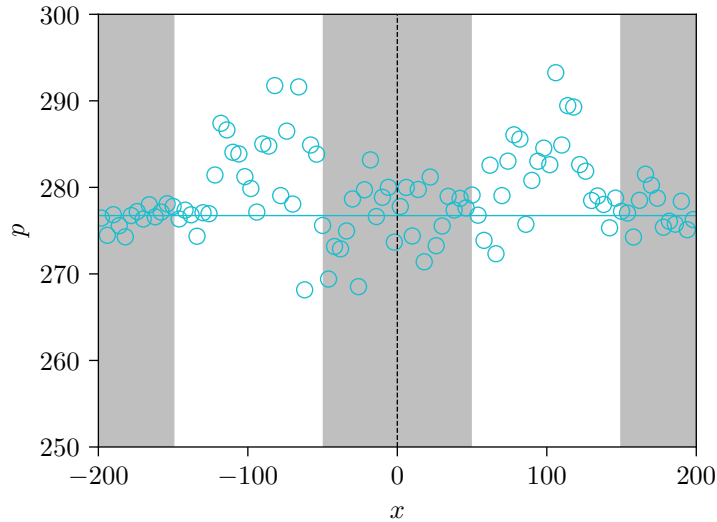


**Fig. 5.3.:** Plot of the total pressure pressure's distribution in bins parallel to the slab in a phase separated steady state (Adapted from Figure 3 of Reference [11]): The total active pressure, given by the sum of all pressure terms in Eq. (5.5), is shown as cyan circles. Remarkably, consideration of the activity's contribution in Eq. (5.5) indeed leads to the definition of an intensive pressure. The pressure in the bulk of the dense and dilute slabs, which are indicated by the shaded gray areas, matches. The enhancement at the interfaces is linked to the interfacial tension which will be discussed in the next section. Averaging the pressure in the bulk regions results in an average pressure of approximately 276, which is indicated by the cyan horizontal line.

represents the pressure in both slabs as shown in Figure 5.3. Note, that only a small excerpt of the  $p$ -axis is shown and thus that the resulting relative uncertainties are actually rather small. We can therefore conclude that the active pressure proposed by [169, 139, 49, 125, 126] seems to be intensive and thus indeed seems to provide a meaningful extension of the concept of pressure to the non-equilibrium case of ABPs. In addition to this important insight, we can also extract some fascinating information from the interfacial regions of the distribution.

### 5.3 Interfacial tension

As noted above, the tangential pressure seems to be constant in the bulk regions of the system. In the interfacial regions, this does not hold true. There are significant peaks, as shown in the non-shaded regions in Figure 5.3, indicating that the tangential pressure is notably larger in the region of the interface. This excess stress can be identified as the interfacial tension. It can be computed as [69]:

$$\gamma = \frac{1}{2} \int_{-L_x/2}^{L_x/2} dx (p_N - p_T(x)) \approx -500. \quad (5.8)$$

While the normal pressure is the same as the bulk pressure throughout the whole system (as argued above), the tangential pressure is larger than the bulk pressure in the interfacial region. Therefore, integrating  $p_N - p_T(x)$  over the full system length and then dividing by 2 to account for the presence of two interfaces gives us the excess stress and thus the interfacial tension. Surprisingly, as  $p_T(x) > p_N$ , the result is negative.

This behavior of an interfacial tension would not be possible in a stable phase separated system in equilibrium. A negative value would indicate that the free energy of the system could be lowered by creation of additional interfaces. Therefore, this would lead to a maximization of interfaces, and thus result in a homogeneous state. Surprisingly, this does not hold for ABPs. As seen both in the previous Chapter 4 and in the simulations undergone to determine the pressure, the phase separation of ABPs is stable. While there are strong fluctuations of the interface, at the propulsion strengths investigated here, one observes a stable slab-geometry and thus a phase-separated steady state. Additionally, also its absolute value  $|\gamma|$  is enormous compared to its counterparts in equilibrium liquid-gas phase separation. I.e. the interfacial tension in liquid-gas coexistence of two-dimensional LJ systems [114], hard-core attractive Yukawa models [31] as well as the hard core square well fluids [122] have been found to be smaller than one. In contrast, the absolute value found for ABPs is between two and three orders of magnitude larger.

To understand this curious effect, the interfacial width  $w$  as defined in Eq. (4.1) and its dependence on the box dimensions were studied by Julian Bialké [11]: As expected, changes to the dimension perpendicular to the slab do not affect the interfacial width, indicating that the system indeed is large enough, that the interfaces are independent of each other and the inner part of the slabs has reached bulk behavior. There is a dependence on the length of the system parallel to the slab, though, which is compatible with standard capillary wave theory and a positive interfacial stiffness, under the assumption that equipartition still holds in our non-equilibrium setting. This can be rationalized by relating interfacial stiffness and tension not by the thermal energy, as expected in equilibrium, but the (negative) work spent by the particle on the surrounding solvent by swimming [11].

To conclude, we could show that the active pressure contribution in ABPs as defined by Refs. [169, 139, 49, 125, 126] and shown in Eq. (5.4) seems to indeed be intensive and at least by that standard can serve as a valid extension to the concept to this system far from equilibrium. Curiously, large scale measurements of the pressure components in a phase separated state reveal that this definition results in a large negative interfacial tension. This is in fact a true non-equilibrium effect, which could not occur in an equilibrium system.



# Influence of shape and dimensionality on the phase behavior

So far, only ABPs in two dimensions have been discussed. One interesting question is, how an anisotropic shape or a higher dimensionality would affect the phase behavior. Earlier studies have already somewhat qualitatively studied the influence of dimensionality by examining three-dimensional active Brownian Spheres [134, 167]. Studies focusing on the behavior of anisotropic active particles include studies of rods [156, 100, 170] but also of dumbbells [136, 144, 48, 25, 26] as well as longer chains [64, 33, 124]. In this chapter, we want to systematically study the influences of both, shape and dimensionality on the phase behavior of active Brownian systems by precise determination of the phase diagram in two specific active dimer models as well as in active Brownian spheres. Most results recapitulated in this chapter have been published in Ref. [121].

## 6.1 Active Brownian dimers

To examine the influence of a non-isotropic particle shape, we study systems of active dimers, which consist of a pair of ABPs that are bound together by a strong finite extensible nonlinear elastic (FENE) bond:

$$u_{\text{FENE}}(r) = -\frac{kR_0^2}{2} \ln \left( 1 - \left( \frac{r}{R_0} \right)^2 \right). \quad (6.1)$$

This allows us to study the influence of the anisotropic geometry in isolation. The rotational dynamics of the active propulsion play a very important factor in determining the system's behavior [25, 26]. Study of combinations of active particles allows to keep the free rotational diffusion of ABPs, whereas the study of anisotropic bodies such non-spherical ellipsoids would lead to the introduction of torques. Not only does this complicate the equations of motion and their numerical treatment, but it also severely complicates the rotational dynamics.

Similar problems arise, when studying systems where the dimer is not propelled along a director that undergoes free rotational diffusion. Earlier studies by Suma

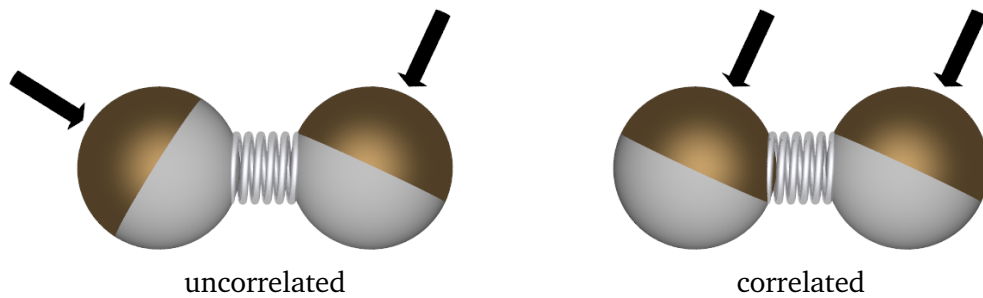


**Fig. 6.1.:** In this work, active Brownian dimers (ABDs) are modeled as a pair of two active Brownian particles. We differentiate two types of ABDs which are shown schematically in this figure. They differ only in their rotational dynamics. For uncorrelated dimers (left) each monomer has an independent director and both of these undergo rotational diffusion independently, corresponding to two independent ABPs that are held together via a bond potential. The monomers of a correlated dimer (right) share a common director. This director still undergoes free rotational diffusion but both particles are always propelled in the same direction. (Adapted from Figure 1 of Reference [121])

et al. [136] for example studied dimers that are propelled in direction of their bond. While this, in terms of experimental realization, might be a more realistic model, this drastically changes the rotational dynamics and therefore the behavior of the system. The rotational diffusion constant and thus the rotational Peclet number describing the strength of activity depend on other parameters, e.g. on the local density. As we want to study only the influence of the non-spherical shape in isolation rather than the multitude of mechanisms involved in the more complex systems, we study dimers, whose monomers' directors still undergo free rotational diffusion.

### 6.1.1 Dimer models

Even for these dimers whose monomers undergo free rotational diffusion, there are different options on how the rotational dynamics of the two monomers influence each other. Here, we study the two extreme cases, namely uncorrelated dimers whose directors are completely independent as well as fully correlated dimers whose monomers share a common director (which still undergoes free rotational diffusion though). The two cases are shown schematically in Figure 6.1.

- The uncorrelated case corresponds to two ABPs that are bound together without any change in their respective rotational dynamics. Therefore, they generally are not propelled in the same direction and thus spend some of their propulsion energy to stretch or squeeze the bond rather than to propel the full dimer.
- In the correlated case, on the other hand, both monomers share a common director and thus they are always propelled in the same direction. Here, most

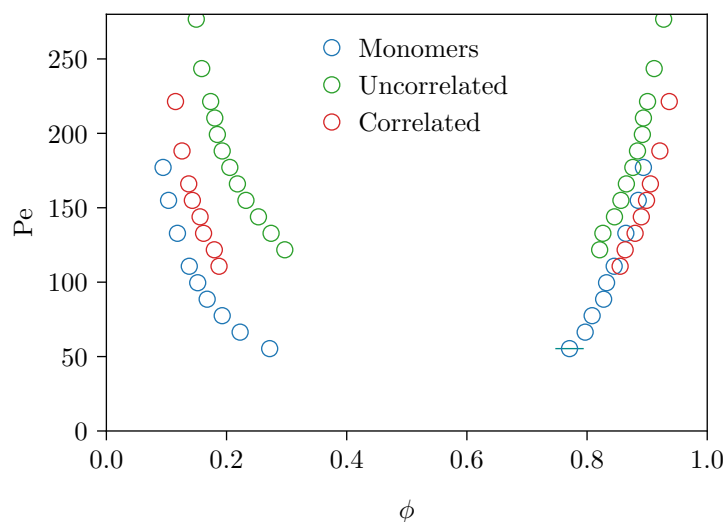


**Fig. 6.2.:** Phase diagram of active Brownian dimers (using data produced by Janina Letz) compared to ABPs (Adapted from Figure 4a) of Reference [121]). While independent ABPs, shown in light blue, phase separate already for  $Pe \gtrsim 40$ , both kinds of dimers phase separate only for much higher propulsion strengths. While the correlated dimers (shown in red) phase separate for  $Pe \gtrsim 60$ , the uncorrelated dimers (shown in green) phase separate  $Pe \gtrsim 90$ . This difference can be easily understood as monomers in uncorrelated dimers will, to some degree, work against each other rather than propelling the full dimer.

of the energy is put into propulsion of the full dimer as the two monomers do not work against each other.

Both types of dimers act in many ways similar to the disk-like ABPs studied in the earlier chapters. In fact, they show a motility induced phase separation as well. At sufficient propulsion strengths, they undergo finite size transitions equivalent to those of ABPs that are shown in Figure 4.1. Therefore, we are able to again make use of the slab geometry at intermediary densities to determine the phase diagram for both kinds of dimers that are studied here.

### 6.1.2 Phase diagram

Analogously to the simulations of active Brownian disks, the phase boundaries are found by extracting the coexisting densities in a phase separated state. Again, simulations take place in an elongated box that ensured stability and a consistent orientation of a slab geometry, which in turn allows to extract bulk phase boundaries by determination of the coexisting densities. The corresponding simulations were conducted by Janina Letz during her Bachelor thesis that was in part supervised by the author.

The resulting phase diagrams are compared to the phase diagram of ABPs in Figure 6.2. Here, the packing fraction of the dimers is computed, approximating their area simply by the area of two disks of diameter  $d_{\text{BH}}$ . The Peclet number is defined in the same way as for ABPs. It turns out, that both kinds of dimers only phase separate for much larger propulsion strengths than the corresponding system of individual self-propelled disks. While ABPs already phase separate at  $\text{Pe} \gtrsim 40$ . Phase separation of the correlated dimers starts at  $\text{Pe} \gtrsim 60$ . Unsurprisingly, uncorrelated dimers phase separate only at even higher Peclet numbers  $\text{Pe} \gtrsim 90$ . As they spend a large amount of the propulsion energy in stretching and squeezing of the bond, the effective propulsion of the full dimer is much smaller than the propulsion of a corresponding correlated dimer with the same active propulsion velocity  $v_0$ .

### 6.1.3 Mapping onto active disks

But we can not only qualitatively but quantitatively understand the differences in the phase diagram between dimers and active disks. To that effect, we will apply a multistep mapping procedure starting at the bare phase diagrams displayed in Figure 6.3(a). As stated above, the packing fraction  $\phi$  for the dimers is approximated here by assuming that one dimer simply occupies the same area as two individual monomers. This does not necessarily hold true. On the one hand the bond potential is forcing the particles together and thus causing the disks to overlap. On the other hand, in case of uncorrelated dimers, opposing orientations can further compress or more likely extend the bond length. To account for both causes of potential overlap, we define a new packing fraction  $\phi' = \rho a_{\text{dim}}$ , where  $a_{\text{dim}}$  is the area of a dimer computed based on the average bond length for the respective dimer type and propulsion strength. The resulting phase diagram is shown in Figure 6.3(b). Accounting for the overlap turned out to drastically reduce the shift towards higher  $\phi$  in case of both dimer types. Nonetheless, the shift in propulsion strength between dimers and monomers but also between dimer types remains.

To understand this difference, we study the influence of the diminished propulsion speed of the uncorrelated dimers on the phase diagram. Assuming a totally stiff bound without any flexibility, the center of mass equation of motion of a dimer in the infinitely dilute limit (i.e. without any other particles in its surroundings) reduces to:

$$\begin{aligned}
 \dot{\mathbf{x}}_{\text{com}} &= \frac{\dot{\mathbf{x}}_1 + \dot{\mathbf{x}}_2}{2} \\
 &= \frac{v_0}{2} \begin{pmatrix} \cos \varphi_1 + \cos \varphi_2 \\ \sin \varphi_1 + \sin \varphi_2 \end{pmatrix} + \sqrt{2D} \frac{\mathbf{R}_{t,1} + \mathbf{R}_{t,2}}{2} \\
 &= v_0 \cos \frac{\varphi_1 - \varphi_2}{2} \begin{pmatrix} \cos \frac{\varphi_1 + \varphi_2}{2} \\ \sin \frac{\varphi_1 + \varphi_2}{2} \end{pmatrix} + \sqrt{D} \mathbf{R}_t.
 \end{aligned} \tag{6.2}$$

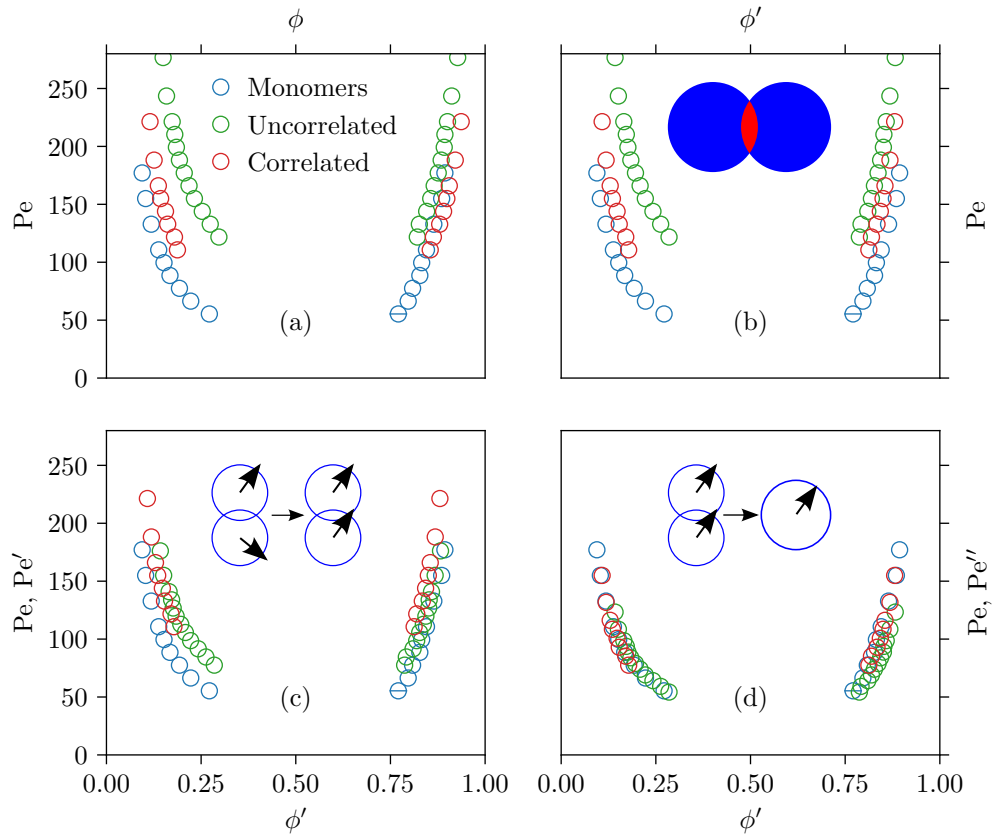


**Fig. 6.3.:** The differences in the phase diagram of ABPs and ABDs, as seen in panel (a) can be understood by a mapping (Adapted from Figure 4 of Reference [121]): First, due to overlap, induced by the bond potential, a dimer actually does not have the same area as two independent disks. This can be corrected by using an average bond length to compute an effective packing fraction  $\phi'$  as shown in panel (b). Most of the difference between uncorrelated and correlated dimers can be understood by computing an effective propulsion velocity of the uncorrelated dimers as an average of the two independent propulsion velocities (c). Lastly, scaling both dimer propulsion strengths by a constant empirical factor of 0.7, which accounts for additional differences (e.g. different cross-sectional areas and rotations of dimers) they can be mapped onto the ABPs' binodals.

This general equation is valid for both correlated, as well as uncorrelated dimers. In the specific case of correlated dimers, the equation greatly simplifies. Here, both of its monomers share a common propulsion direction that undergoes rotational diffusion equivalently to a simple active disk. Therefore,  $\varphi_1 = \varphi_2$ , and thus the equation of motion reduces to that of ABPs in the infinitely dilute limit (cf. Eq. (3.1)):

$$\dot{\mathbf{x}}_{\text{com,corr}} = v_0 \begin{pmatrix} \cos \varphi \\ \sin \varphi \end{pmatrix} + \sqrt{D} \mathbf{R}_t. \quad (6.3)$$

In the case of uncorrelated dimers, however, the propulsion directions of the monomers forming the dimer are independent. After a change of variables  $\bar{\varphi} = \frac{\varphi_1 + \varphi_2}{2}$  and  $\tilde{\varphi} = \frac{\varphi_1 - \varphi_2}{2}$  the equation of motion takes the form:

$$\begin{aligned} \dot{\mathbf{x}}_{\text{com,uncorr}} &= v_0 \cos \tilde{\varphi} \begin{pmatrix} \cos \bar{\varphi} \\ \sin \bar{\varphi} \end{pmatrix} + \sqrt{D} \mathbf{R}_t \\ \dot{\tilde{\varphi}} &= \sqrt{D_r} R_{r,1} \\ \dot{\bar{\varphi}} &= \sqrt{D_r} R_{r,2}. \end{aligned} \quad (6.4)$$

Obviously, this has a similar form as the equation in the correlated case. Nonetheless, there is a crucial difference, as the propulsion term is reduced by a factor of  $\cos \tilde{\varphi}$ . To estimate the difference in mean propulsion strength, we now analyze this factor. First, we observe that  $2\tilde{\varphi}$  is the sum of two independent random variables  $\varphi_1$  and  $-\varphi_2$  that are uniformly distributed in  $[-\pi, \pi)$ . Therefore, its probability distribution is given as a convolution of the uniform distribution in this interval with itself:

$$p_{2\tilde{\varphi}}(2\tilde{\varphi}) = \int_{-\infty}^{\infty} d\varphi p_{\varphi}(2\tilde{\varphi} - \varphi) p_{\varphi}(\varphi), \quad (6.5)$$

where we used:

$$p_{\varphi}(\varphi) = \begin{cases} \frac{1}{2\pi} & \varphi \in [-\pi, \pi) \\ 0 & \text{otherwise.} \end{cases} \quad (6.6)$$

To simplify the notation, we can rewrite  $p_{2\tilde{\varphi}}(2\tilde{\varphi})$  in terms of an integral over Heaviside step functions  $\Theta(x)$ :

$$\begin{aligned} p_{2\tilde{\varphi}}(2\tilde{\varphi}) &= \frac{1}{2\pi} \int_{-\infty}^{\infty} d\varphi \Theta(\pi + \varphi - 2\tilde{\varphi}) \cdot \Theta(\pi - \varphi + 2\tilde{\varphi}) \cdot \Theta(\pi + \varphi) \cdot \Theta(\pi - \varphi) \\ &= \frac{1}{2\pi} (\min(2\tilde{\varphi} + \pi, \pi) - \max(2\tilde{\varphi} - \pi, -\pi)) \\ &= \begin{cases} \frac{1}{2\pi} + \frac{2\tilde{\varphi}}{4\pi^2} & 0 > 2\tilde{\varphi} > -2\pi \\ \frac{1}{2\pi} - \frac{2\tilde{\varphi}}{4\pi^2} & 0 < 2\tilde{\varphi} < 2\pi \\ 0 & \text{otherwise.} \end{cases} \end{aligned} \quad (6.7)$$

Therefore,  $\tilde{\varphi}$ 's probability distribution is decaying linearly around 0 as:

$$p_{\tilde{\varphi}}(\tilde{\varphi}) = \begin{cases} \frac{1}{\pi} + \frac{\tilde{\varphi}}{\pi^2} & 0 > \tilde{\varphi} > -\pi \\ \frac{1}{\pi} - \frac{\tilde{\varphi}}{\pi^2} & 0 < \tilde{\varphi} < \pi \\ 0 & \text{otherwise.} \end{cases} \quad (6.8)$$

Thus, we can now compute the effective (i.e. mean) propulsion speed of an uncorrelated dimer's center of mass as:

$$\begin{aligned} \langle |\cos \tilde{\varphi}| \rangle &= \int_{-\pi}^{\pi} d\tilde{\varphi} p(\tilde{\varphi}) |\cos \tilde{\varphi}| \\ &= 2 \int_0^{\pi} d\tilde{\varphi} p(\tilde{\varphi}) |\cos \tilde{\varphi}| \\ &= \frac{2}{\pi}. \end{aligned} \quad (6.9)$$

By rescaling the propulsion strength of the uncorrelated dimers with this factor, we find an effective propulsion strength  $Pe' = \frac{2}{\pi}Pe$ . A comparison of the binodal lines employing this effective  $Pe'$  in case of the uncorrelated dimers is shown in Figure 6.3(c). Here, the dimers' curves match quite well and thus most of the differences between correlated and uncorrelated dimers can be explained by the simple mapping, that was outlined above. This is quite remarkable as we neglected any effects of the non-uniform propulsion strength present for uncorrelated dimers. It is possible to further improve the mapping by not computing a single average bond length in the first step, but to account for different average overlaps in the dense and the dilute region by computing an average bond length depending on the surrounding density. While this slightly improves the matching, it turns out that it still does not account for the main differences which arise due to the non-uniform swimming speed in uncorrelated dimers. Therefore, the corresponding results are not presented here in any more detail.

While the different dimer types already match remarkably well in Figure 6.3(c), there is still a shift of the phase boundaries between dimers and monomers. We attribute this difference to the differing cross sectional area as well as to the difference in interaction between pairs of dimers and monomers respectively as well as the anisotropy and rotational degrees of freedom that are only present in the case of dimers. In fact, scaling the propulsion strength of dimers by another (heuristic) factor of 0.7, which is meant to account for these differences, all curves can be brought to a rather good agreement. While the binodals of the correlated dimers match well, the curves corresponding to the uncorrelated dimers do not match as nicely. This difference is unsurprising, though, as additional effects of both the non-uniform swimming speed as well as the increase of the relative motion of the monomers forming an uncorrelated dimer are not accounted for.

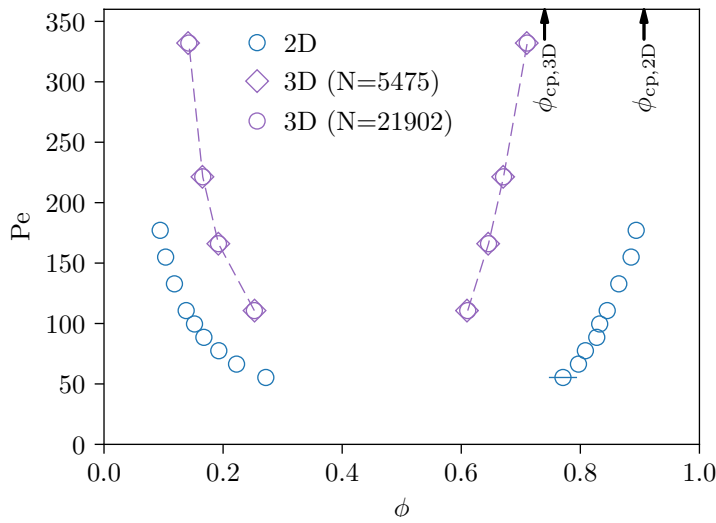


**Fig. 6.4.:** The phase diagram of active Brownian spheres in three dimensions is shown in purple with a connecting dashed line as a guide for the eye. For comparison the phase diagram of ABPs in two dimension is shown in light blue. One can easily see that phase separation sets in much later for the spheres. A comparison of the width of the binodals is not meaningful, as they represent different quantities. Here,  $\phi$  represents area and volume fractions for the two- and three-dimensional systems respectively. Two different system sizes are shown for the three-dimensional case to demonstrate the absence of finite size effects. (Adapted from Figure 5 of Reference [121])

## 6.2 Active Brownian spheres in three dimensions

Active Brownian particles in three dimensions also show a MIPS, based on the same mechanism as those in two dimensions. Earlier studies already suggested, however, that a much higher propulsion strength is needed to reach the regime of phase separation [167, 134]. But to allow for a quantitative comparison between the two cases and thus to evaluate the influence of the system's dimensionality an exact determination of the phase diagram is needed.

### 6.2.1 Phase diagram

Equivalently to the methodology in two dimensions, the binodal packing fractions can be determined by extracting coexisting densities in a phase separated slab geometry. Placing  $N = 21902$  spheres in a box with side lengths  $L_x = 2.5L_y = 2.5L_z = 60$  at propulsion strengths of  $Pe \gtrsim 100$  results in a stable slab geometry which allowed us to extract binodal densities. The resulting phase diagram is compared to the two dimensional results in Figure 6.4.



While the Peclet number is defined equivalently in both two and three dimension, the packing fraction  $\phi$  refers to an area and a volume fraction in two and three dimensions respectively. Therefore, a comparison of the width of the binodal lines is not meaningful. This can be easily seen already by comparison of the highest possible packing fractions: The area fraction of an infinite system of hard disks in two dimensions can reach values as high as  $\phi_{\text{cp},2\text{D}} \approx 0.9069$  [37], whereas the volume fraction of an analogous system of hard spheres in three dimensions is limited by  $\phi_{\text{cp},3\text{D}} \approx 0.7405$  [51]. Nonetheless, one can see that the dense branches in both cases quickly approach close packing for increasing propulsion strength.

Direct comparison of the ordinates, on the other hand, already provides interesting insights. Phase separation in two dimensions occurs at much lower propulsion strengths. It already sets in for  $\text{Pe} \gtrsim 40$  in two dimensions, whereas in three dimensions it only occurs for  $\text{Pe} \gtrsim 80$ . Therefore, there is roughly a factor of 2 between the minimum propulsion strengths in two and three dimensions. Said difference can be understood following a simple kinetic argument. In active Brownian particles, two different time scales govern the system: One is the mean reorientation time  $\tau_r$ , depending only on the model; the other is the mean collision time  $\tau_c$ , which is the mean time between two collisions of a particle with other particles and thus dependent on both the active propulsion velocity  $v_0$  and the packing fraction. Their ratio actually determines how likely it is that particles are blocked on collision and thus the onset of phase separation [104, 133]. The mean reorientation time has an explicit dependence on the dimensionality. As both, two- and three-dimensional ABPs, have the same rotational diffusion constant, the corresponding orientational correlation times in two  $\tau_{r,2\text{D}} = D_r^{-1}$  and three dimensions  $\tau_{r,3\text{D}} = (2D_r)^{-1}$  differ by a factor of 2, which is consistent with our findings. Therefore, the increased propulsion strength that is needed for phase separation in three in comparison to two dimensions is caused by the faster orientational decorrelation in three dimensions which has to be counterbalanced by a smaller mean collision time and thus a larger propulsion velocity.

To verify these results and to preclude the existence of finite size effects, we also simulated a box with side lengths  $L_x = 5L_y = 5L_z = 60$  with  $N = 5475$ . The resulting points on the binodal line are shown as purple diamonds in Figure 6.4. They perfectly coincide with the results of the larger box size (shown as purple circles). Based on this, we can conclude that we accurately and independently of the system size determined the phase diagram of active Brownian particles in three dimensions as well.



# Determination of the critical point using the original subsystem distribution method

After studying the binodal lines and how their position is influenced by various factors, we will finally turn to the critical region, that so far has been exempted from our analysis. Our first goal is to precisely determine the position of the critical point. Unfortunately, the corresponding machinery known from equilibrium physics cannot be directly applied to our driven systems. Therefore, we have to incrementally work towards a satisfactory methodology, starting from the machinery that has been successfully applied to an active variant of the Asakura-Oosawa model before [141, 143]. In this chapter, these gradual improvements are explored. The chapter ends with an analysis of the problems associated with the methodology. Our final approach circumventing these issues and its results are presented in Chapter 8. Several parts of this chapter are a recapitulation of material also included in Refs. [120, 143].

## 7.1 Original subsystem distribution method

Determination of critical points is a hard problem. The slab method employed to determine the binodal lines well in the phase separated regime fails for systems close to criticality (cf. Section 4.2). In the vicinity of a critical point, as explained in Section 2.2.4, the correlation length (and time) diverge, which results in a diverging width of the interfacial region and thus a failure of the slab densities to converge to bulk values. Therefore, to examine the critical region of the phase diagram and in particular to determine the exact location of the critical point, other methods have to be employed. Specifically, the theory of finite size scaling, explained in Section 2.3, allows to gain insights into the critical properties of examined systems. Methods like the intersection of cumulants for different system sizes (cf. Section 2.3.1) are widely employed to locate the critical point [13, 109, 161, 68, 147, 152, 111]. For their application, it is vital to sample the particle number distribution. To that end, in equilibrium, grand canonical (GC) simulations have been established as the method of choice and have been employed successfully in a variety of different systems [18, 160, 162, 161, 68, 147, 111]. Unfortunately, a direct application of the machinery established for equilibrium systems to our model system is impossible, as

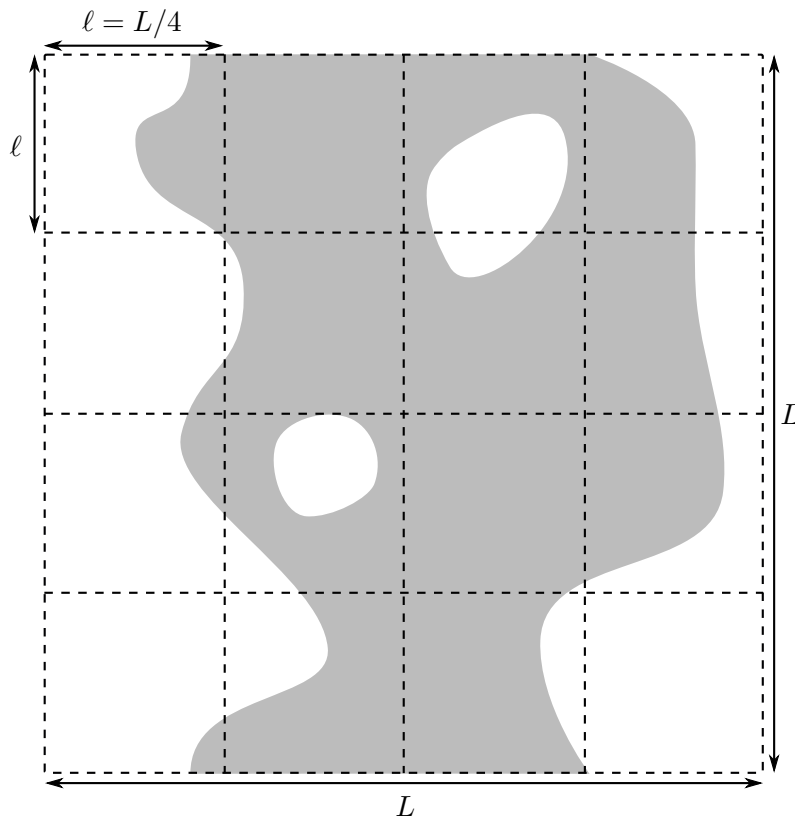


**Fig. 7.1.:** Sketch of the system geometry used in the original subsystem distribution method [13]. Instead of simulating several small systems with fluctuating particle number via a GC scheme, one large system is simulated. This system of side length  $L$  is then subdivided into  $N^2$  subsystems, each with side-lengths  $\ell = L/N$  and a fluctuating particle number that is quasi-independent of all other subsystems (for sufficiently large  $N$ ). All other subsystems serve as a particle reservoir. By changing  $N$ , one such simulation allows to determine the particle number distribution for different subsystem sizes  $\ell$  and thus simulating one large system at different values of  $Pe$  allows to find a crossing of cumulants for different  $\ell$  and in turn an estimate of the critical propulsion strength  $Pe_{cr}$ .

GC simulations are not available in driven systems, for which no rigorous free energy is known (so far). No algorithm properly sampling a fluctuating particle number is available, which prevents a direct determination of particle number fluctuations from a GC simulation. Thus, to determine the position of the critical point in an active system by crossing of cumulants, other methods have to be employed.

The basis of our analysis is the sampling of particle number fluctuations via block-distribution methods that have been applied to systems in [13, 12, 108, 110, 109] and out of equilibrium [141, 143]. The general idea is quite simple using the notion of a grand-canonical system being in contact with a (thermodynamically large) particle reservoir: Subdividing a (unfortunately not thermodynamically) large simulation box of side length  $L$  into  $N^2$  smaller subsystems (also called subboxes) of side lengths  $\ell = L/N$ , allows each of those systems' particle numbers to fluctuate.

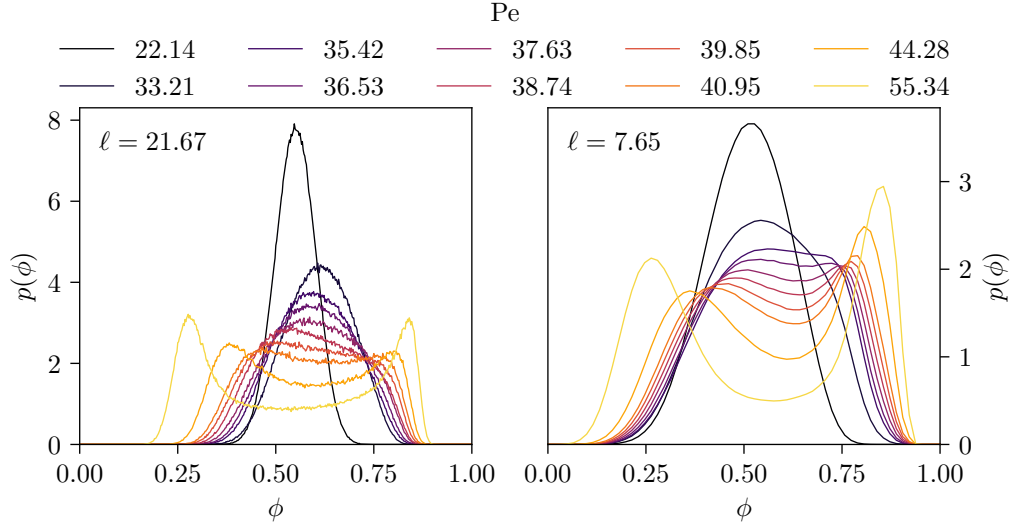


**Fig. 7.2.:** Plots of the packing fraction’s probability distribution in subsystems for different subsystem sizes  $\ell$  and their dependence on the propulsion strength  $Pe$  (following the corresponding locus of maximum  $Q_\ell(Pe)$  (cf. Section 7.3)): The subplots show the subsystem sizes  $\ell \approx 21.67$  and  $\ell \approx 7.65$  corresponding to  $N = 6$  and  $N = 17$  subdivision along both axes respectively. The different propulsion strengths are color coded going from low propulsion strengths  $Pe \approx 22.14$  far in the homogeneous region plotted in black to high propulsion strengths  $Pe \approx 55.34$  well in the phase separated region plotted in yellow. For both  $\ell$ , there is a clear evolution going from a Gaussian-like single peaked structure through a broadening until the peak eventually breaks in two, giving way to a double-peak structure for high propulsion strengths. However, the curves are much more sharply peaked at higher subsystem sizes and the transition from single to double peak happens in a much shorter  $Pe$  interval.

The rest of the box, namely all other subsystems, provide a particle bath for each individual subbox. A sketch of this geometry is shown in Figure 7.1.

The large  $L \times L$  box features periodic boundary conditions and is kept at a fixed overall density and thus a fixed particle number. The dashed grid then sketches one possible subdivision of the full system into  $N^2 = 16$  smaller subsystems. One big advantage of the method is that a simulation of one large system allows to determine the particle number and density distributions of several subsystem sizes by application of different subdivisions to the same underlying simulations. Different  $N$  result in different  $\ell$  and thus in practice only one large box size has to be simulated to sample one point in the phase space. Note, however, that those results for different subdivisions are heavily correlated and thus proper sampling is needed to reliably determine the size dependence of the moments of the particle number and density distributions.

Exemplary plots of resulting packing fraction distributions in ABPs for two different subdivisions are shown in Figure 7.2. Both plots show the expected evolution from

a single peaked structure in the homogeneous region, through a broadening until a double peaked structure emerges in the phase separated regime. Consequently, the general evolution of  $Q_\ell$  seems to be well reproduced in the subsystem scheme. Qualitatively, also the dependence on the subsystem size  $\ell$  seems to be recovered. In the large system, the distribution is peaked more sharply and the transition from single to double peaked structure happens over a short  $Pe$  interval. In contrast, the peaks of the distribution for the small system are much broader and the transition is considerably washed out. We can thus expect a steeper  $Q_\ell$  curve for the larger system, consistent with the crossing of  $Q_\ell$  in GC studies of equilibrium systems.

It remains to choose a proper number of subdivisions  $N$ . Obviously, a low  $N$  such as  $N = 4$  used in Figure 7.1, results in strong correlations between the particle numbers in the different subsystems. It is thus only used here for illustrative purposes. For the actual determination of the critical point  $N$  has to be chosen higher. As explained in References [141, 143], there are lower and upper bounds on  $N$  and thus on  $\ell$ . For low  $N$ , the validity of assuming quasi-independent subsystems in a large particle bath breaks down. The correlations between subsystems become stronger and thus lead to a distortion of the particle number distribution. Furthermore, simulations by design take place close to a critical point and are thus subject to diverging correlation lengths, which provides the basis for the method to work, but also correlation times, which lead to longer autocorrelation times for larger subsystems. This in turn, prevents us from using extremely large systems consequently containing large subsystems. Even in equilibrium systems, significant computational effort is needed to achieve convergence in very large systems [152]. On the other hand, there also exists a lower bound for valid subsystem sizes and thus an upper bound on  $N$ . For subsystems that are too small, the particle number distribution becomes distorted as well, as the number of particles becomes so low that the Gaussian limit of the Poisson distribution is not reached. Also such extremely small system sizes might make additional corrections to the first order scaling laws necessary [154, 160]. While these constraints are stated explicitly only in References [141, 143], they are inherent in all applications of the subsystem distribution method, for which box dimensions to include in the analysis have to be chosen [13, 109, 152]. Unfortunately, these constraints are not strict, meaning that the associated distortions gradually increase. Therefore, the choice of subsystems is somewhat empirical and no hard boundaries can be derived. However, the decision can for example be based on studying the order of curves far above and below the critical point [141, 143].

In contrast to GC simulations, in subsystem distribution methods the chemical potential of the "particle bath" is not set directly but rather by the overall density in case of a liquid-gas transition or the overall magnetization in case of Ising-like systems. As combining all subsystems results in the full simulation box, this sets the mean of the order parameter distribution fixed to the value that was used in

the simulation box rather than fluctuating around a mean value which would be the case for a GC scheme. While this might introduce a bias in the sampling, it also provides a major benefit. In case of a GC simulations, the mean density would have to be determined via averaging. Therefore, insufficient sampling would result in a systematically underestimated second moment of the measured density distribution due to an incorrectly determined mean [41]. As the mean density in the subsystem distribution method is known, there is no systematic underestimation in this case. Nonetheless, sufficiently long (i.e. significantly longer than the correlation time) sampling runs are needed to produce meaningful results. But in this non-systematic but statistical case, independent runs provide a reliable estimate of the uncertainty in the calculation.

The cumulant method in general and its application using block-distribution methods specifically only allow to determine the critical value of the control parameter. Furthermore, it is useful only if it is applied along a locus that goes through the critical point in the thermodynamic limit. This is unproblematic in systems that allow to find the critical value along the order parameter axis by symmetry arguments, e.g. Ising-like systems. There, the system is symmetric with respect to inversion of all spins and thus the critical point is known to lie on the locus  $m = 0$ . For other systems such as an off-lattice system featuring a gas-liquid transition the situation is not as simple. The critical value along the order parameter axis, e.g. the density or packing fraction, cannot simply be identified based on symmetry arguments but has to be determined by other means. In equilibrium systems, a common approach is to simply follow the extension of the rectilinear diameter [152, 141, 143]. In the case of ABPs this does not look promising, as the law of the rectilinear diameter is violated already far above the critical point (cf. Figure 4.3) and thus, its linear extension is highly unlikely to go through the critical point. Therefore, another method is needed to find a proper density locus along which one should simulate. In the following, two different options for the choice of the locus are explored and compared.

## 7.2 Results along constant density

Starting with the easiest option, we will try a locus of constant packing fraction. Luckily, earlier results seem to indicate that such simulations at least in an equilibrium LJ system indeed are able to predict the critical point quite accurately and even that the precise density (or packing fraction) does not seem to be crucial [109]. On the contrary, the reported results for different densities in the range between  $\rho = 0.30$  and  $\rho = 0.36$  show crossings at compatible temperature values. Note, that these intersections neither happen perfectly at one point nor do the resulting critical

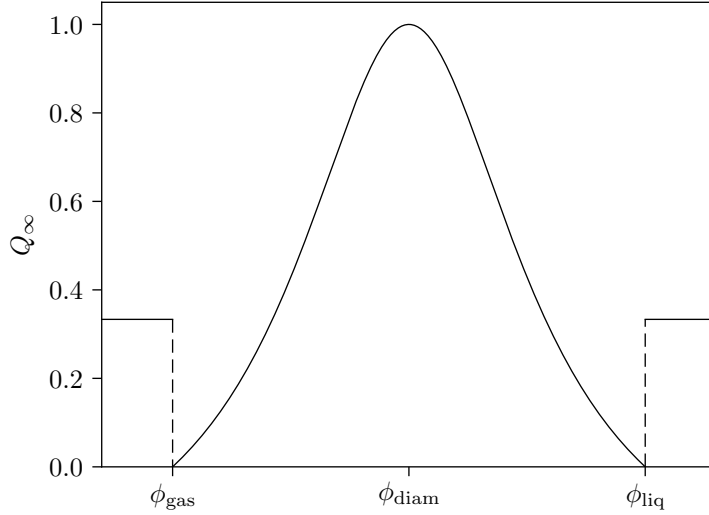


**Fig. 7.3.:** Infinite system size limit  $Q_\infty(\bar{\phi})$  in the two phase region [66]: In an infinitely large system,  $Q_\ell$  approaches this limiting form (assuming analogy of  $\mu$  and  $\bar{\phi}$ ). For packing fractions outside of the binodal lines ( $\bar{\phi} < \phi_{\text{gas}}$  or  $\bar{\phi} > \phi_{\text{liq}}$ ), the packing fraction distribution is Gaussian and thus  $Q_\infty = 1/3$ . Between the binodals,  $p_{\bar{\phi}}(\phi)$  essentially shows a double peak structure, where changing  $\bar{\phi}$  changes the relative weights of the peaks and with that  $Q_\infty$ . The peak value of  $Q_\infty = 1$  is reached for equal weights corresponding to the diameter  $\bar{\phi} = \phi_{\text{diam}}$ .

temperatures match perfectly. But these discrepancies are rather small especially considering the small system size that was studied ( $N = 4096$  particles) [109]. Nonetheless, in our case, it remains necessary to estimate the correct critical packing fraction at least approximately. For equilibrium systems, following a linear extension of the rectilinear diameter can already give a good indication of the valid packing fraction region to examine. Analogously to the reasoning in discarding simulations along a locus extending the rectilinear diameter, extracting this information in our non-equilibrium case does not provide a meaningful estimate. Therefore, we have to find an alternative method to estimate the correct packing fraction. Another option is to study the dependence of  $Q_\ell$  on the mean packing fraction roughly at the critical propulsion strength. In GC simulations, this would correspond to the dependence on the applied chemical potential. In the two phase region, the theoretical prediction derived by Kim and Fisher [66] for this dependence in the thermodynamic limit is shown in Figure 7.3. Outside the binodal lines, the distribution becomes Gaussian, resulting in  $Q_\ell = 1/3$ . Within the binodal lines, the distribution becomes doubly peaked. A change of chemical potential (or in case of the subsystem method a change of the global packing fraction) then results only in a change of relative weights of the two peaks. This leads to  $Q_\ell$  starting at 0 for the points on the binodal and in between exhibiting a maximum reaching  $Q_\ell = 1$ . The position of this maximum can be interpreted to be analogous to the often applied equal area locus which will go through the critical point [18]. For finite systems, the curve looks similar, albeit



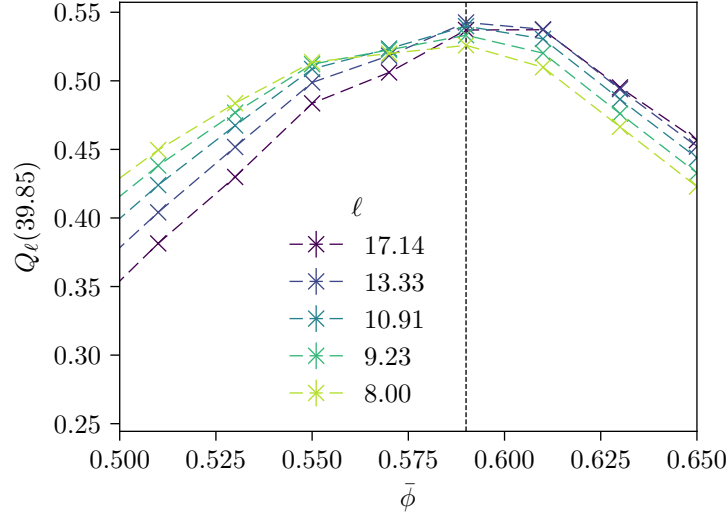


**Fig. 7.4.:** Density dependence of  $Q_\ell(\text{Pe} \approx 39.85)$ : Different curves correspond to different subsystem sizes. The connecting lines are only meant as guides to the eye. As only one run was done for every packing fraction respectively, the uncertainties are estimated via the fluctuations of  $Q_\ell(\text{Pe} \approx 39.85)$  during the run. All curves exhibit a maximum at approximately  $\bar{\phi} = 0.59$ , which is the packing fraction used in the crossing analysis above. It is indicated by a dashed vertical line.

with softer transitions [66, 147]. Also the maximum does not reach  $Q_\ell = 1$ . In fact, the basis of the method of crossing  $Q_\ell$  is the system size dependence of said maximum value. Nonetheless, we can use the position of the maximum to estimate the proper density to simulate at, when examining the dependence of  $Q_\ell(\bar{\phi})$  on the mean packing fraction close to the critical point.

Figure 7.4 shows this course of  $Q_\ell(\bar{\phi})$  at  $\text{Pe} \approx 40$  in a box of side-length  $240 \times 240$ . At  $\text{Pe}_{\text{cr}}$  and in the limit of infinite system size,  $Q_\ell(\bar{\phi})$  is expected to exhibit a maximum at  $\phi_{\text{cr}}$  [66]. As the  $Q_\ell(\bar{\phi})$  curves for all system sizes  $\ell$  reach their maximum approximately at  $\bar{\phi} \approx 0.59$  (indicated by a dashed vertical line), this value will be used as a rough estimate of the critical packing fraction.

Following this approximate determination of  $\phi_{\text{cr}}$ , simulations are done for different propulsion strengths along a constant packing fraction locus of  $\bar{\phi} = 0.59$ , to determine the critical propulsion strength  $\text{Pe}_{\text{cr}}$  by finding the intersection point of  $Q_\ell(\text{Pe})$  for different  $\ell$ . Similarly to the simulations used to approximate  $\phi_{\text{cr}}$ , a square box of side length  $240 \times 240$  is used, containing 35317 ABPs, which corresponds to the intended packing fraction of  $\bar{\phi} = 0.59$ . Simulations are done at six different values of  $\text{Pe}$  between 33 and 45, which is the approximate interval within which  $\text{Pe}_{\text{cr}}$  is presumed to lie. To allow for a more accurate determination of  $Q_\ell$  and its uncertainty and even more importantly to minimize the effect of the long correlation times close to the critical point, five independent runs were done at each state point. In each of

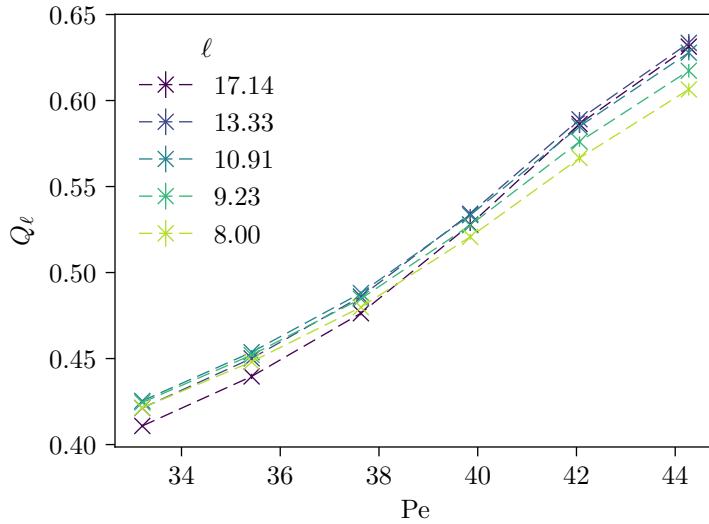


**Fig. 7.5.:** Plot of  $Q_\ell(\text{Pe})$  for a large system ( $240 \times 240$ ) along a constant density locus of  $\bar{\phi} = 0.59$ . The different colors correspond to the different subsystem sizes ranging from  $\ell = 8$  ( $N = 30$ ) displayed in green to  $\ell \approx 17.14$  ( $N = 14$ ) plotted in purple. Each curve corresponds to the mean of five independent runs. Even though some of the curves cross, they do so in consecutive intersections over the full width of the simulated  $\text{Pe}$  interval. This is exacerbated by the fact that curves corresponding to both the smallest and the largest subsystem size do not seem to cross their respective neighboring curves within this rather large  $\text{Pe}$  section.

these independent simulations, the system was relaxed from a homogeneous state for  $t = 500$ . Subsequently, a production run of length  $t = 2000$  was done, evaluating the second and fourth moments of the density distribution in the subsystems of different sizes at intervals of time  $\delta t = 0.5$ .

Our estimate of  $Q_\ell(\text{Pe})$  and its uncertainty are then found by computing:

$$Q_\ell(\text{Pe}) = \left\langle \frac{\left\langle \left( \phi_\ell(\text{Pe}) - \bar{\phi} \right)^2 \right\rangle_t^2}{\left\langle \left( \phi_\ell(\text{Pe}) - \bar{\phi} \right)^4 \right\rangle_t} \right\rangle_{\text{runs}}. \quad (7.1)$$

Here,  $\bar{\phi} = 0.59$  refers to the fixed average packing fraction,  $\langle \cdot \rangle_t$  and  $\langle \cdot \rangle_{\text{runs}}$  refer to time-averaging and averaging over independent runs respectively. Its standard error is found by studying the fluctuation between independent runs.

The results are shown in Figure 7.5. The plot shows  $Q_\ell(\text{Pe})$  for five different subsystem sizes from  $\ell = 8$  to  $\ell \approx 17.14$  which are colored going from green to purple with increasing subsystem size. The system sizes that are displayed correspond to a separation of the full system into  $N = 30, 26, 22, 18, 14$  subsystems along both axes thus resulting in 900, 676, 484, 324, and 196 total subsystems respectively. As explained above, the choice of subsystem sizes to use when applying this method

is somewhat empirical. To determine the position of the critical point within the interval, we would need to find a point where  $Q_\ell$  becomes independent of the subsystem size. As the curves are supposed to show opposite order above and below a critical point this would correspond to an intersection point at which all curves cross (cf. Fig. 2.2). Studying the course of the different curves, we find not one such isolated point, but multiple consecutive intersection points. While the curves corresponding to small subsystem sizes cross at small values of  $Pe$ , those corresponding to larger  $\ell$  cross at higher propulsion strengths. The problem becomes worse when we study the change in order of the curves above and below the rough starting estimate for the position of the critical point between  $Pe \approx 33.2$  and  $Pe \approx 44.3$ . Even though this interval is rather broad, not all curves show the expected order both at the upper and the lower end of the interval. Going to larger or smaller subsystem sizes exacerbates the problem. As mentioned above, the range of subsystem sizes has to be limited empirically in all applications of subsystem distribution methods. However, the failure to find a full crossing of curves for subsystems within only less than a factor of 2.2 of each other placed in a rather large system such as the one studied here, indicates that the method has to be refined before any conclusions about the position of the critical point can be made.

### 7.3 Locus of maximum $Q_\ell$

To understand the failure of our naive approach, we go back to  $Q_\ell$ 's dependence on the overall packing fraction. While a simulation along its maximum will show the expected monotonic increase from  $1/3$  to  $1$  when increasing  $Pe$  going through the critical point, the same does not necessarily hold true when simulating at different  $\bar{\phi}$ . In fact, imagine simulating along a locus of constant packing fraction significantly differing from the critical packing fraction. Starting in the homogeneous region,  $Q_\ell$  would be close to  $1/3$  but coming closer to the binodal, it would first start to decrease as it would approach the minimum seen in Figure 7.3. After going through the transition point, the minima would spread further apart, which would then lead to an increase in  $Q_\ell$  as now  $\bar{\phi}$  relative to the minimum corresponds to a point closer to the diameter. This is obviously not a problem in systems as the Ising model where the correct locus is known by symmetry. But even for systems lacking this explicit symmetry, simulating at a locus sufficiently close to the critical point can give proper results, as demonstrated using a LJ system in 2D [108, 110, 109]. As shown in Reference [109], the position of the maximum is independent of and the width of the maximum is only very weakly dependent on the system size such that the difference from the maximum value is similar for all system sizes. Therefore, the order of the curves is nearly unaffected and an estimate for the critical point can still be found by examining the consecutive intersections that are spread over

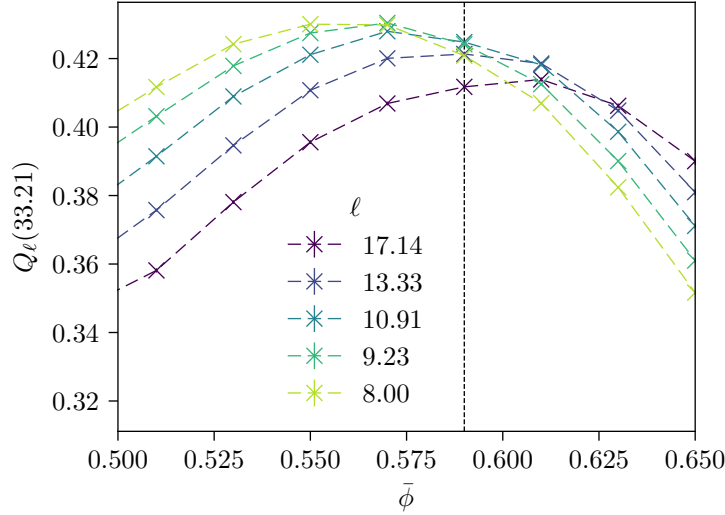


**Fig. 7.6.:** Overall packing fraction dependence of  $Q_\ell$  ( $Pe \approx 33.21$ ): The presentation is analogous to Figure 7.4. Again all curves exhibit a maximum. However, the positions of the maxima are shifted depending on the subsystem size  $\ell$ . The position of the maximum for the largest subsystem is close to  $\bar{\phi} = 0.59$  (even though slightly shifted to higher  $\bar{\phi}$ ), whereas the maxima for small subsystems are severely shifted towards smaller  $\bar{\phi}$ . This results in a difference between the order of the curves when examining their maximum values and their values at  $\bar{\phi} = 0.59$ .

a sufficiently small interval [109]. Especially when simulating on a locus closer to the equal area line, such as for example along the linear extension of the rectilinear diameter, the critical point can be found with great accuracy. Examples are the subsystem distribution study of the 3D LJ model by Watanabe et al. [152] or the GC studies of the hard core square well (HCSW) model [93, 67, 66, 68]. However, there are examples where the simulation along one locus shared by all system sizes fails. One particularly well studied example is the restrictive primitive model (RPM) [77, 67, 68]. Studying the dependence of  $Q_\ell$  on the chemical potential in this model reveals, that the symmetry of the short ranged models mentioned before, namely the shared position of the maximum in  $Q_\ell$ , is not obeyed in this model. In contrast, the position of the maximum of  $Q_\ell$ , when scanning the chemical potential, is strongly dependent on the system size, and thus to reliably extract the critical point, each system size has to be studied along its own locus of maximum  $Q_\ell$  [77, 67, 68].

Similarly to the RPM, ABPs show a strong asymmetry, which one can already guess from the strong violation of the law of the rectilinear diameter [66]. This becomes especially problematic, when the critical packing fraction was not guessed perfectly, as this would cause the curves to not intersect in exactly one point. Furthermore, as the behavior above and below criticality cannot be reliably predicted and even the general order of  $Q_\ell$  for different system sizes due to the asymmetry is not well known, this failure to exactly hit the critical point can actually lead to non-crossing curves

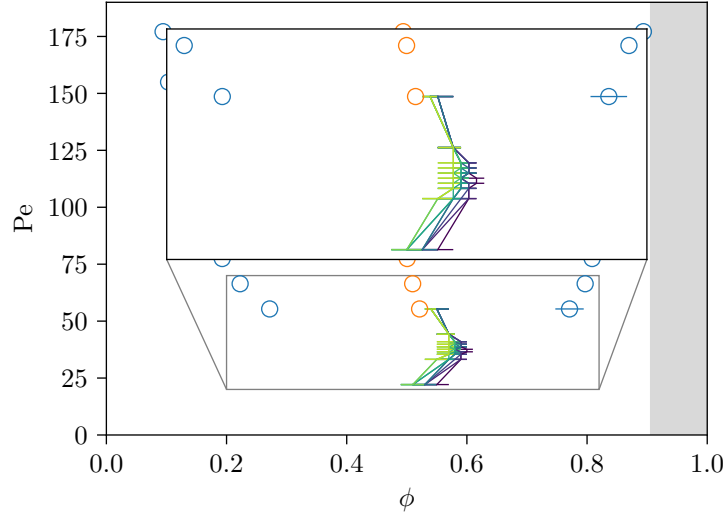


**Fig. 7.7.:** Course of the loci of maximum  $Q_\ell$  for different subsystem sizes  $\ell$  plotted in the phase diagram shown in Figure 4.3: The loci are colored going from green for small subsystems  $\ell \approx 7.22$  to purple for large subsystem sizes  $\ell \approx 14.44$ . Errorbars indicate the distance to the next simulated state point, connecting lines are only meant as guides for the eye. The inset shows the critical region slightly enlarged to increase visibility. While there is no significant difference in the phase separated region, the loci split up going into the homogeneous region. There is a systematic trend, that the larger subsystems show a more pronounced deviation from the linear extension of the diameter than the smaller subsystems.

$Q_\ell$ . Even when the critical packing fraction was determined accurately, corrections to scaling as well as other deficiencies in the methodology can cause non-intersecting lines [68]. To highlight the problem, Figure 7.6 shows the dependence of  $Q_\ell$  on the mean overall packing fraction  $\bar{\phi}$  for  $Pe \approx 33.21$ . The value used in the simulations along the locus of constant packing fraction ( $\bar{\phi} = 0.59$ ) is shown as a dashed vertical line. Simulating at this packing fraction in fact gives misleading results for  $Q_\ell(Pe)$ . The different curves exhibit their maxima at different  $\bar{\phi}$ . At  $\phi_{cr} \approx 0.59$ , the curves corresponding to small  $\ell$  misleadingly show an order corresponding to the two-phase region, while the large subsystems show the correct order. Comparing the maxima instead shows that all curves indeed show the order corresponding to the homogeneous region. Therefore, as  $\phi_{cr}$  is not known apriori and we need a locus going through  $\phi_{cr}$  in the thermodynamic limit, and as choosing  $\bar{\phi}_{\ell, \max}$  as a locus has proven very successful in equilibrium studies [93, 77, 67, 66, 68], we will analyze  $Q_{\ell, \max}(Pe)$  instead of  $Q_\ell(Pe)|_{\bar{\phi} \approx \phi_{cr}}$ .

## 7.4 Results along the locus $Q_{\ell, \max}$

To study a possible crossing of  $Q_{\ell, \max}(Pe)$  for different subsystem sizes  $\ell$ , we first have to determine the course of  $\bar{\phi}_{\ell, \max}$ , the mean packing fraction locus maximizing

$Q_\ell(\text{Pe})$  for each  $\text{Pe}$  and  $\ell$ . As we already saw in Figures 7.6 and 7.4, this locus indeed depends on both of these parameters. Determination of this locus is much more demanding computationally in comparison to the simulations along the locus of constant packing fraction, as for each value of  $\text{Pe}$  multiple simulations at different packing fractions have to be done to determine the maximum along the packing fraction axis. To accelerate the simulations and also to reduce the long correlation time, a system size of  $L = 130$  is chosen. The corresponding results look very similar to Figures 7.4 and 7.6. For reference, the results of these simulations for three different propulsion strengths are also shown in Appendix A.1. Depending on the spread of the maxima as well as the width of the peaks up to seven different packing fractions were evaluated. To properly estimate the uncertainty of the corresponding result for  $Q_\ell$ , ten independent runs were conducted for every state point, meaning for every  $\text{Pe}, \bar{\phi}$  pair. As every simulation in itself has to be run for a sufficiently long time to generate proper results that are independent of the starting configuration, these simulations as mentioned above were very demanding computationally and thus the resolution could not be increased much further. Therefore, even with these extensive simulations, the uncertainties associated with the determination of  $\bar{\phi}_{\ell, \max}$  are still rather large. Figure 7.7 shows the resulting locus, where each point corresponds to the respective mean density at which the best estimate of  $Q_{\ell, \max}(\text{Pe})$  exhibits its maximum while disregarding the associated uncertainties. Although this seems unsatisfactory, there is no good alternative, as the functional form of the peak is not known and thus no meaningful fit can be done. To allow for an estimation of the associated uncertainties of the locus nonetheless, errorbars indicating the distance to the next neighboring state point simulated are shown.

Sufficiently far in the phase-separated regime, the loci of all subsystem sizes seem to fall onto each other, as already seen in Figure 7.4. This joint locus approaches the extension of the diameter for large propulsion strengths ( $\text{Pe} \approx 55.34$ ). When decreasing the propulsion strength, the course of the joint locus is changed towards higher packing fractions. After reaching a maximum packing fraction at  $\text{Pe} \approx 40$ , the loci turn towards lower values of  $\bar{\phi}$  again. Even though the qualitative course of all loci is similar, they differ quantitatively. For propulsion speeds smaller than  $\text{Pe} \approx 44.28$  the loci split up. Rather than to follow a joint path, there is a systematic difference in the loci's courses depending on  $\ell$ . The deviation from the rectilinear packing fraction becomes larger with increasing subsystem sizes. The locus corresponding to the smallest subsystem size reaches a maximum packing fraction of  $\bar{\phi} \approx 0.57$ , whereas the largest subsystem's locus has its maximum at  $\bar{\phi} \approx 0.59$ . Even at small propulsion strengths of  $\text{Pe} \approx 25$ , the loci still follow different courses. This significant difference can be seen nicely in Figure 7.6.

As explained in Section 7.3, we want to evaluate  $Q_\ell(\text{Pe})$  along their respective locus in hope of a more well-defined crossing point for different subsystem sizes  $\ell$ . For

this, we have to not only find the locus  $\bar{\phi}_{\ell,\max}(\text{Pe})$  but also the corresponding value  $Q_{\ell,\max}(\text{Pe})$ . The significant uncertainties in the determination of the locus provide an obstacle to an estimation of  $Q_{\ell,\max}(\text{Pe})$  and its associated uncertainty. As the maxima are rather flat and the uncertainties in the determination of  $Q_{\ell}(\text{Pe})$  for different  $\bar{\phi}$  are small, we chose to simply take the respective maximum value as well as its uncertainty as estimates for  $Q_{\ell,\max}(\text{Pe})$ . This choice is somewhat problematic as the finite resolution of  $Q_{\ell}(\text{Pe})$ 's dependence on the overall packing fraction  $\bar{\phi}$  can lead to a bias toward smaller values for  $Q_{\ell,\max}(\text{Pe})$ . On the other hand, taking the maximum value as an estimate introduces a bias towards larger values of  $Q_{\ell,\max}(\text{Pe})$ . Both these systematic errors are ignored by our choice of estimation. An alternative strategy to overcome these problems would be to fit each curve and then to extract the maximum of the curve and its uncertainty from the fit parameters. While this could yield results not suffering from the biases mentioned above, it is not a viable option in our case. The functional form of  $Q_{\ell}(\text{Pe})$ 's dependence on the overall packing fraction  $\bar{\phi}$  is not known and thus we do not know what functional form to use for our fit. We therefore stick to the original estimation, noting that the maxima are rather flat in comparison to the resolution of points along the dimension of the packing fraction. Nonetheless, when interpreting the estimated  $Q_{\ell,\max}(\text{Pe})$ , one should keep the associated biases in mind.

Plotting our estimates against  $\text{Pe}$  for different subsystem sizes results in Figure 7.8. Far below a putative critical point ( $\text{Pe} \approx 22$ ) all curves approach the limiting value of  $Q_{\ell} = 1/3$  for a homogeneous system with a Gaussian distributed packing fraction. There is still some deviation from the limiting value, but as even the largest subsystem with  $\ell = 14.44$  is rather small, it is expected that transition from homogeneous to phase separated is still considerably washed out. Also the Gaussian distribution is an idealization as obviously densities below zero or over  $\phi_{\text{cp}}$  are not possible and thus especially for distances far from the average packing fraction, the distribution will be distorted. These facts do not hamper our analysis, though. All curves representing the different system sizes show the correct order going from small  $Q_{\ell,\max}$  for large  $\ell$  to larger values of  $Q_{\ell,\max}$  for smaller subsystems.

Starting at low  $\text{Pe}$ , the correct order holds until  $\text{Pe} \approx 33$ , as demonstrated in the upper left inset. This inset shows  $Q_{\ell,\max}(33.2)$ , meaning  $Q_{\ell,\max}$  for a fixed propulsion strength of  $\text{Pe} \approx 33.2$ , versus the subsystem size  $\ell$ . We can see that all curves are still ordered as expected in the homogeneous region, as  $Q_{\ell,\max}(33.2)$  is monotonically decreasing for increasing  $\ell$ . Although the order is already imperfect as some of the values corresponding to small subsystems already overlap within their uncertainties. This agrees with observations of analyses done on equilibrium systems which also found consecutive intersections systematically going from smaller to larger subsystems [93]. The range of intersections found in ABPs seems to be more drastic though. At high propulsion strengths, we see that all curves that show

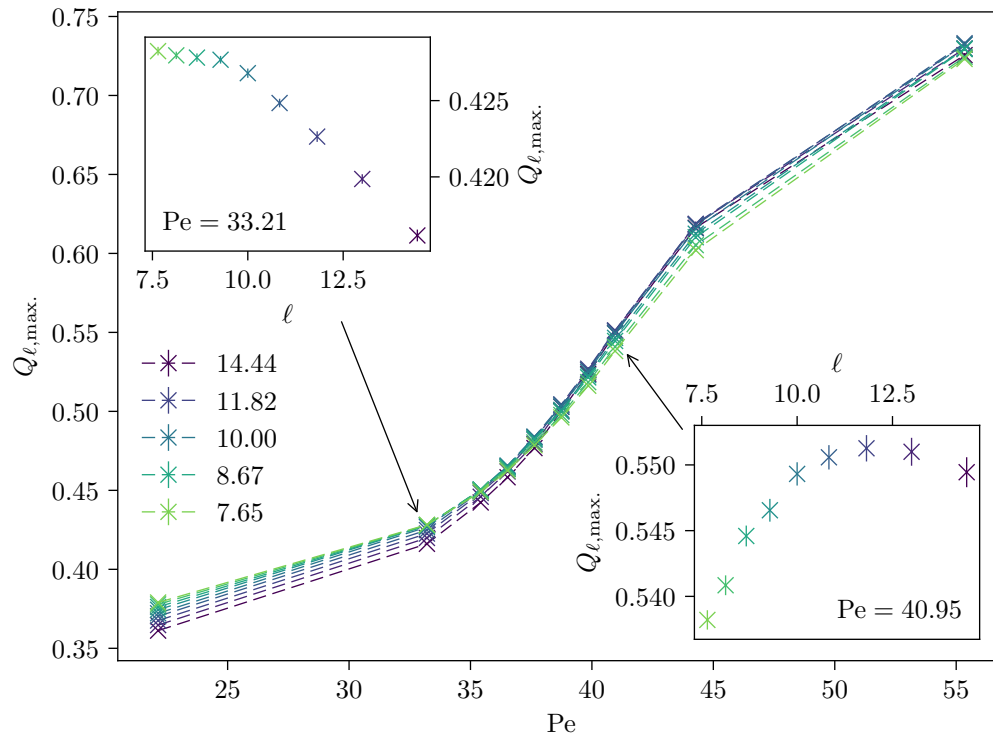


**Fig. 7.8.:** Course of  $Q_{\ell, \max}(Pe)$  for different  $\ell$  when evaluated along the respective locus of maximum  $Q_{\ell}(Pe)$ . Note, that the connecting lines only serve as guides to the eye. Far in the homogeneous region at  $Pe \approx 22.14$  the curves show the correct order going from small values for large subsystem sizes to larger values for small subsystems. All curves are close to the limiting value of  $Q_{\ell, \text{hom.}} = 1/3$ . Well in the phase separated region at  $Pe \approx 55.34$  most curves have crossed and thus inverted their order. Only the largest subsystems do not show the expected behavior. The insets show the dependence of  $Q_{\ell, \max}(Pe)$  on the subsystem size  $\ell$  at  $Pe \approx 33.21$  and  $Pe \approx 40.95$  highlighting the inversion of order between those two points.



the correct order far above the critical point at least within uncertainties ( $\ell \lesssim 12$ ) already exhibit this behavior for  $Pe \approx 41.0$ . This is again demonstrated via an inset in Figure 7.8. In the lower right  $Q_{\ell, \max}(40.95)$ 's dependence on the subsystem size  $\ell$  is plotted. All but the largest two subsystems ( $\ell = 13.0$  and  $\ell \approx 14.4$ ) show (within uncertainties) the monotonic increase associated with the phase separated regime. Above this propulsion strength, all curves that did not show this order do not cross. They rather start to decrease again with respect to the smaller system sizes. The reason for this failure will be discussed in Section 7.5. For now, we will have to exclude them from the analysis, keeping only those curves that show the expected order far above and below the critical region. While this is not very satisfying, it is a known draw-back of the subsystem method and the same criterium for exclusion has also been used in earlier applications of the method [141, 143].

In the  $Pe$  interval between  $33 \lesssim Pe \lesssim 41$ , the curves of  $Q_{\ell, \max}(Pe)$  interchange their position and thus invert their order. For high propulsion strengths the sequence does not change anymore for  $Pe \gtrsim 41.0$ , which we thus take as an upper bound for the position of the critical point. For low propulsion strengths only the smallest subsystems started to cross before  $Pe \lesssim 35.4$ . As these smallest subsystems only contain around 40 particles and, furthermore, as the intersection points are expected to move towards the bulk value of  $Pe_{\text{cr}}$  for larger subsystems, we estimate a lower bound for the critical point to be at  $Pe \approx 35.4$ . We thus estimate the critical point to lie in the interval of  $Pe_{\text{cr}} \in [35.4, 41.0]$ . Comparing these results with the simulations along the locus of constant packing fraction, this is already a big improvement. The crossing area of the latter, shown in Figure 7.5, showed intersections over the full simulated range of  $33 \lesssim Pe \lesssim 45$ , with failures to cross of both the largest and smallest subsystems. We thus had to conclude that this allowed no proper estimation of  $Pe_{\text{cr}}$  at all. Simulating along the locus of maximum  $Q_{\ell}(Pe)$  leads to the significantly narrower crossing region shown in Figure 7.8, which allowed for a first, though tentative, estimation of  $Pe_{\text{cr}}$ . This improvement is especially remarkable, given that the size of the full simulated system was much smaller in this case. Notwithstanding these improvements, there still remains a rather broad intersection region, and more importantly, especially large subsystems fail to show the correct order even far in the phase separated region.

## 7.5 Problems of the original subsystem distribution method

To understand why the subsystem method fails to produce more accurate results and why already rather small subsystems fail to show the expected limiting behavior in the phase separated regime, it is instructive to study the corresponding packing

fraction distributions in subsystems of different sizes over the range of applied propulsion strengths  $Pe$ . These are shown in Figure 7.2. Both subplots shows the evolution of the packing fraction distribution, increasing the propulsion strength from well in the homogeneous regime ( $Pe \approx 22.14$ ) through the critical region and well into the phase separated regime ( $Pe \approx 55.34$ ) for one individual subsystem size. Qualitatively, the plots for the different subsystem sizes show a similar evolution. Quantitatively, there are differences though, which actually form the basis of the  $Q_\ell(Pe)$  analysis as explained in Section 2.3.1. In the homogeneous region, the differences turn out similar to those explained in said section, which are also known from grand canonical studies in equilibrium [160]. Far in the homogeneous regime, the Gaussian-like curve is peaked much more narrowly for the larger subsystems. Moreover, and more important for the  $Q_\ell(Pe)$  analysis, the broadening and the breakage of the symmetry of the peak begins much earlier in the smaller subsystems, which in turn leads to an earlier increase in  $Q_\ell$  producing the order expected beneath a critical point. In the phase separated regime, the two peaks of the curve also seem to become more pointed for larger subsystems. However, this only sets in at rather high propulsion strengths and even at the highest propulsion strength that is shown, the trend seems to be not very well pronounced and the intermediary densities do not seem to become less significant at higher  $\ell$ .

These problems stem from biased measurements of the order parameter distribution in the subsystems. Even in equilibrium they do not reproduce the grand canonical distribution [13]. We rather measure a conditional probability under the constraint that the overall packing fraction in the system remains conserved. At first sight, this constraint and thus the measurement of a conditional probability distribution does not seem to matter when examining small subsystems in a large surrounding box. However, especially above the critical point in the phase separated region, the simulation at an intermediary packing fraction leads to phase separation and thus the creation of interfaces. Therefore, the probability of intermediary densities especially in larger subsystems is much more pronounced in comparison to (in the equilibrium case) the grand canonical distribution [13].

The issue is highlighted in Figure 7.9. Here, packing fraction distributions for different subsystem sizes are compared at a high propulsion strength ( $Pe \approx 55.34$ ), which lies already well in the phase separated region. As mentioned above, the peaks are becoming more pronounced for larger subsystems. While the lighter colored curves corresponding to the smaller subsystems show broader flanks, the darker curves showing the distributions for larger  $\ell$  exhibit a much steeper increase and thus much more pronounced peaks. This only holds for the outer flanks of the curve though. At their inner flanks, the peaks of the larger subsystems are broader and at intermediary densities the order of the curves does not follow the expected behavior [13]. In contrast to the observed behavior, one would expect the

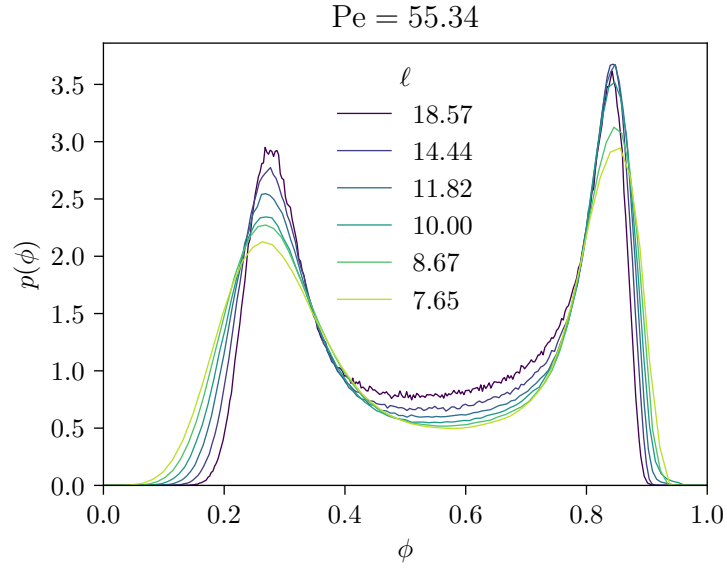


**Fig. 7.9.:** Plot illustrating the subsystem size dependence of the packing fraction probability distribution far above the critical point in the phase separated regime. Different subsystem sizes  $\ell$  range from  $\ell \approx 7.65$  color-coded in green to  $\ell \approx 18.57$  color-coded in purple. All curves show a pronounced doubly peaked structure. As expected for increasing subsystem size, this structure becomes more and more sharply peaked. The intermediary densities do not follow this trend though. In contrast to experience from grand canonical distributions, the order of  $P(\phi_{\text{cr}})$  is not from large to small systems but inverted. This can be traced to the over-expression of interfaces in the subsystem method.

probability of intermediary densities to decrease for larger  $\ell$  in the phase separated region. The failure to do so can be understood by considering the extreme case of phase separation into a strict slab geometry. Disregarding any fluctuations of the interface, the average number of subsystems containing a part of the interface (also disregarding the theoretical special case, where the boundary coincides perfectly with the subsystem boundaries) is given as  $2N = \frac{2L}{\ell}$  which seems to decrease with increasing subsystem size  $\ell$ . But since the number of subsystems in the full box is given by  $N^2 = \frac{L^2}{\ell^2}$ , the fraction of the subsystems containing a part of the interface in this theoretical limiting case actually grows as  $\frac{2}{N} = \frac{2}{L}\ell$ , thus growing linearly in  $\ell$ . Even though realistic systems obviously show much more complex interface geometries, these considerations make it plausible why large subsystems especially at high propulsion strengths fail to show the expected behavior.



## Improving the subsystem distribution method

To overcome the problems described in the last section, we now turn to a new improved subsystem distribution method, that was developed for the 2D Ising model by Florian Dittrich in his Diploma thesis [28]. After explaining and verifying the new approach, we apply this method for ABPs to gain a more precise estimate for the position of critical point. Again, large parts of this chapter are a recapitulation of material also included in Ref. [120].

### 8.1 Idea of the improved subsystem distribution method

In a nutshell, the idea of the improved method is to artificially exclude the occurring interfaces, that are causing problems in the original subsystem distribution method, from the analysis by exploiting the stability of interfaces in a finite system [28]. In such systems, even in the vicinity of a critical point, interfaces remain somewhat stable. Simulating an elongated box, similar to the one used to determine binodal densities in Chapter 4, we force the system into a slab geometry. Specifically, we use the system that is schematically shown in Figure 8.1, namely a system with side lengths  $2\ell \times 6\ell$  and thus an aspect ratio of 1:3. Rather than extracting the distribution of packing fractions essentially randomly throughout the simulation box as it was done before, we now place only four subsystems of size  $\ell \times \ell$  in the system (cf. Figure 8.1). Two of them are centered around the center of mass in the elongated direction (blue in Figure 8.1). The other two are shifted by  $3\ell$  along the elongated direction (red in Figure 8.1). In the presence of a stable slab, these subsystems are thus placed at the center of both the dense and the dilute region. Note, though, that fluctuations become very strong close to the critical point, and thus, that bubbles and even rifts can appear. By choosing the subsystems as specified, the weight of the interfacial area nonetheless is significantly suppressed. Below the critical point, the slab will eventually dissolve.

Different from the original method, we also do not impose a fixed overall packing fraction  $\bar{\phi}$  on the subsystems but only on the full system. The packing fraction is

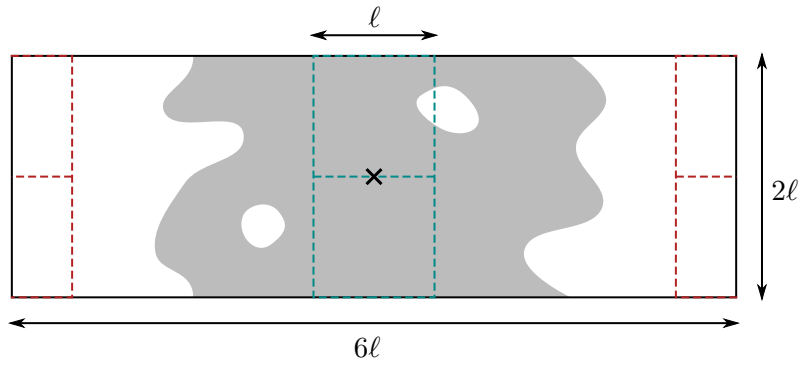


**Fig. 8.1.:** Sketch of the system geometry used in the improved subsystem distribution method [28] (Adapted from Figure 1c) of Reference [120], reprinted figure with permission from [J. T. Siebert et al., *Physical Review E*, 93, 030601(R), 2018] Copyright 2018 by the American Physical Society.): Simulating an elongated box with side length ratio of 1 : 3 at an intermediary packing fraction, the system's preferential configuration is a slab geometry in which the slab is aligned with the short axis. This allows us to suppress measurements of the interfacial region by measuring the packing fraction distribution only in the four quadratic subsystems indicated by dashed lines: Two subsystems are placed at the center of mass, the other two are shifted by half of the longer box dimension and thus centered in the dilute region.

chosen to result in a system roughly filled half by either phase. The packing fraction in both phases should then only depend weakly (if at all) on  $\bar{\phi}$ , whereas choosing two boxes in each phase directly results in a measurement that corresponds to an equal-area locus [18], which in turn should allow us to properly determine the position of the critical point. Effectively, the two areas of size  $2\ell \times 2\ell$  in which no measurements are done act as a particle bath for the measurement boxes. Obviously, this is still not equivalent to a simulation in the grand canonical ensemble in which the system can exchange particles with an infinitely large reservoir. Nonetheless, the new method is qualitatively similar to the original subsystem distribution method, but much closer to the ideal measurements than the original approach.

There is another difference between the methods: In the original method, estimates for all subsystem sizes are based on the same underlying simulation of a large system. In contrast, the new method requires independent simulations to be done for every subsystem size that is examined. While this is much more expensive from a computational point of view, it also provides some benefits. First of all, it results in independent estimates for all subsystem sizes, which in turn allows for a more meaningful estimation of the associated uncertainties. Furthermore, the original subsystem approach results in subtly changed boundary conditions for different  $\ell$  [13]. Therefore, in the original scheme an additional length scale and consequently an additional scaling variable is introduced [28]. This is fixed in the improved method as well, as the boundary conditions are the same for all subsystem sizes. Also the computational costs of simulating each system size individually are

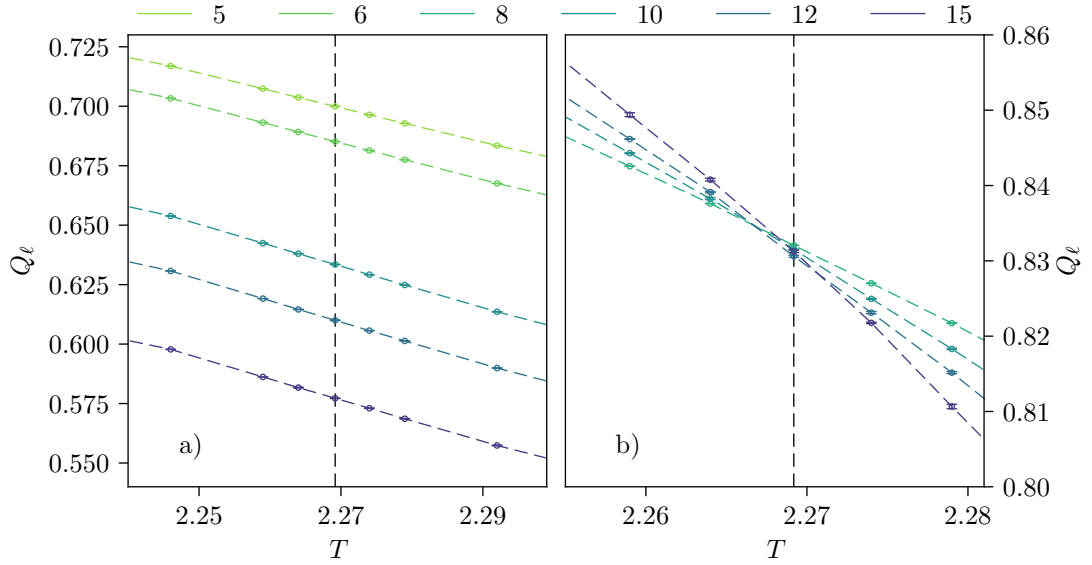


**Fig. 8.2.:** Testing the improved subsystem method to determine the critical point of the 2D Ising model (all data by Florian Dittrich [28], adapted from Figure 1a) and b) of Reference [120], reprinted figure with permission from [J. T. Siebert et al., Physical Review E, 93, 030601(R), 2018] Copyright 2018 by the American Physical Society.): Especially in two-dimensional lattice models, e.g. the Ising model in 2D, the original subsystem distribution method is known to fail [109]. As shown in Panel a)  $Q_\ell(T)$  curves fail to cross over a wide range of temperatures around the analytically known critical temperature  $T_{cr} \approx 2.269185$  [92] (indicated by the dashed vertical line). In contrast, the new method results in a precise intersection point very close to  $T_{cr}$  as shown in Panel b).

counterbalanced by the fact that only one packing fraction per system size and propulsion strength has to be simulated. Finally, the number of subsystems in each box is much smaller in the new method, resulting in a drastically increased need for more sampling. However, the system sizes that are simulated are much smaller than in the original approach, such that in the end the computational costs of both methods are of the same order of magnitude.

## 8.2 Test on the 2D Ising model

As mentioned above, the improved method was developed by Florian Dittrich during his Diploma thesis [28]. In his work, it was tested on the two-dimensional Ising model. Due to its simplicity, and in the case of the two-dimensional model, the availability of an analytic solution [92], the Ising model frequently serves as a benchmark system. In fact, the original subsystem distribution method has been developed using the Ising model as well [13]. It turned out though, that especially in the 2D Ising model the original method does not only fail to give a single intersection point but the cumulants of different subsystem sizes do not cross at all [109]. As a

result, the 2D Ising model not only serves as an excellent benchmark system due to the availability of exact reference values, but also due to the drastic failure of the original method. An improved method, that is able to accurately predict the critical point in the 2D Ising model is very likely to be successful for other model systems, that show a less severe failure of the original method. The lack of intersections is demonstrated in Figure 8.2 in the left panel, using data provided by Florian Dittrich. The critical temperature is shown as a dashed vertical line [92]. The curves corresponding to different system sizes are roughly parallel and do not intersect within a wide interval around that critical temperature. The right panel shows the results applying the improved method, again using data provided by Florian Dittrich [28]. Here the curves actually do intersect. This intersection point is in excellent agreement with the critical temperature, which is again indicated by a dashed vertical line. Therefore, the improved subsystem distribution method, as demonstrated in Figure 8.2, is in fact able to accurately and precisely determine the critical temperature in the 2D Ising model, which in turn is very promising for its application to ABPs.

### 8.3 Test on the 2D Lennard-Jones model

The proof of concept, applying the new subsystem distribution method to the 2D Ising model, already suggest, that its application can correctly predict critical points and indeed might improve upon the results of the original subsystem scheme. Nonetheless, there are significant differences between the 2D Ising model and ABPs. Most importantly, there remains the question whether the method not only works for on-lattice systems such as the Ising model but also for off-lattice systems. Given the fact, that the original subsystem scheme seems to be only applicable to off-lattice systems [109], it is not self-evident, that the improved scheme will be equally effective in on- and off-lattice systems. To ensure its applicability, we will therefore first study its ability to predict the position of the critical point in a 2D LJ liquid.

In contrast to the Ising model, there is no analytic solution of the 2D LJ model to use as a reference. In fact, the position of the critical point in the 2D LJ model strongly depends on the chosen cut-off in the LJ potential as well as whether the potential is consecutively shifted [123]. Given the availability of reference values for the original subsystem scheme [109], we use a cut-off of  $2.5\sigma$  and subsequently shift the potential to zero at the cut-off:

$$u(r) = \begin{cases} 4\epsilon \left( \left(\frac{\sigma}{r}\right)^{12} - \left(\frac{\sigma}{r}\right)^6 + 2.5^{-6} - 2.5^{-12} \right) & r < 2.5\sigma \\ 0 & \text{otherwise.} \end{cases} \quad (8.1)$$



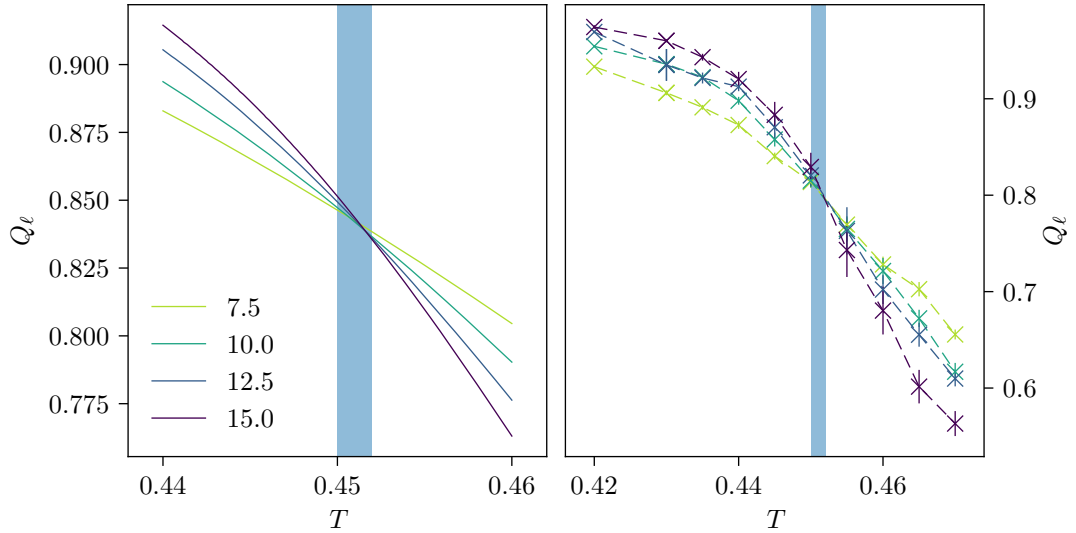


**Fig. 8.3.:** Testing the improved subsystem method to determine the critical point on the 2D LJ model: Both panels show  $Q_\ell$  curves for four different system sizes. The left panel shows the results of our GC reference simulations along the locus of maximum  $Q_\ell$ , which provides an estimate of  $T_{\text{cr}} \approx 0.451$ . The right panel features the results of the improved subsystem method, which are in excellent agreement to the reference data.

Even though there have been multiple studies on the position of the critical point in a 2D LJ liquid in the literature [159, 18, 96], only two studies have focused on this exact potential form, namely Smit and Frenkel [123] using a fit to the binodal lines to extract the critical point and Rovere et al. [109] using the original subsystem distribution method. Both studies therefore do not suffice as reference values of high accuracy for the improved subsystem distribution scheme.

Instead, we conduct GC Monte Carlo (MC) simulations in a quadratic box with periodic boundary conditions along both axes using a simulation code provided by Peter Virnau. Simulations are done at the critical temperature estimate ( $T = 0.47$ ) given by [109]. The chemical potential  $\mu$  is tuned to obtain a two-peaked density distribution. Using histogram reweighting [39, 40, 160, 70],  $Q_\ell$  can be extracted for a wide variety of values for  $T$  and  $\mu$  in the critical region. The critical temperature is then found by studying  $Q_\ell$  for multiple system sizes  $\ell$  along the locus of maximum  $Q_\ell$  [93, 77, 67, 66, 68]. The result is shown in the left panel of Figure 8.3. There are consecutive intersections over a very slim area around  $T_{\text{cr}} \approx 0.451$ . Alternatively, the critical temperature can be estimated by fitting the density distribution to the 2D Ising master curve extracted from the data provided by Florian Dittrich [28]. Even though no field mixing was employed [160], an estimate for the critical temperature can be extracted which lies at  $T_{\text{cr}} = 0.450$ . Although no in-depth error analysis was conducted, we can sufficiently pinpoint the critical point of the LJ fluid using the potential described by Eq. (8.1) to be at  $T_{\text{cr}} = 0.451(1)$ . This estimate is indicated

by the light blue shaded area in both panels of Figure 8.3. Surprisingly, this value is considerably lower than the estimate found by the original subsystem scheme ( $T_{\text{cr}} = 0.472(10)$ ) [109]. Note, however, that the system used in Ref. [109] was rather small in comparison to the systems employed for ABPs in this work.

After successfully estimating a reference value for  $T_{\text{cr}}$ , we now employ the improved subsystem scheme to check its accuracy for the (off-lattice) 2D LJ fluid. Simulations are done using an underdamped system applying a Langevin thermostat with  $\gamma = 1$  in a box with side length ratio of 1 : 3 and periodic boundary conditions along both axes. Densities are measured employing the subsystem arrangement shown in Figure 8.1. The resulting  $Q_\ell$  curves for different subsystem sizes  $\ell$  are shown in the right panel of Figure 8.3. The curves do not only show the expected behavior significantly above and below the critical temperature, but their intersection point is in excellent agreement with the reference value extracted from the GC simulations. Especially, the improved method indeed seems to give much more accurate results than the original subsystem scheme [109]. Even though there are still quite significant uncertainties associated with the values in Figure 8.3, these could be reduced by additional sampling. Given that this only serves as a check for the methodology, the significant computational effort that would be necessary to do so does not seem justified. Note, that while employing the subsystem scheme, the computational effort to extract the critical point is two to three orders of magnitude higher than that of the GC approach, even though it still gives results of inferior accuracy. Therefore, as long as GC simulations are available, they definitely remain the standard choice to extract critical points.

Nonetheless, we established that the improved subsystem scheme is in fact able to accurately predict the critical point not only in on- but also in off-lattice systems. Furthermore, GC simulations, as mentioned above, are not available for ABPs. We therefore employ the improved subsystem scheme to our system in the following to see whether it can improve upon the estimates of the critical point found by the original subsystem method.

## 8.4 Determination of the critical point in ABPs

After successfully benchmarking the improved method, it is now applied to ABPs. Analogous to the benchmarks, an elongated system with side ratio 1 : 3 is used (cf. Figure 8.1). Simulating at roughly the critical overall packing fraction ( $\bar{\phi} = 0.6$ ), the system's preferred state above as well as close to the critical point is the slab geometry. Again, four subsystems of size  $\ell \times \ell$  are selected at the center of the dense and the dilute region to conduct the measurements.

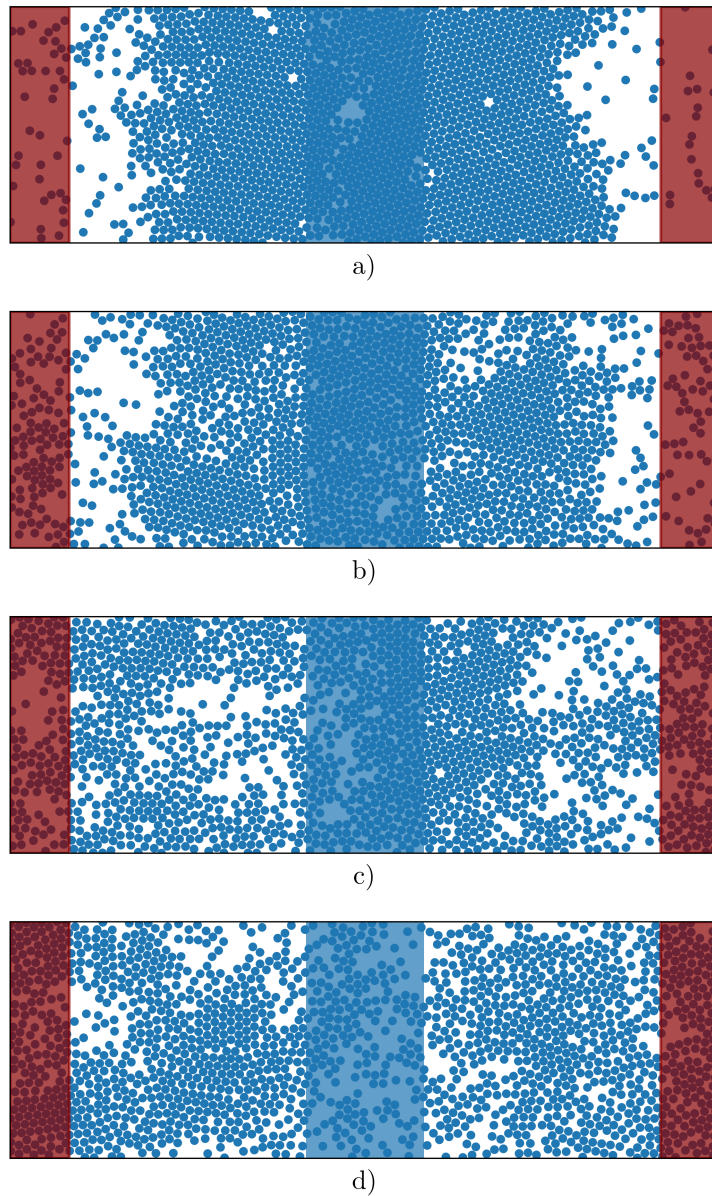


**Fig. 8.4.:** Exemplary snapshots demonstrating the application of the improved subsystem distribution method for ABPs (Adapted from Figure S1 of the SI to Reference [120], reprinted figure with permission from [J. T. Siebert et al., *Physical Review E*, 93, 030601(R), 2018] Copyright 2018 by the American Physical Society.): As shown schematically in Figure 8.1, an elongated box is simulated. The measurement areas in the dense and dilute region are indicated as blue and red shaded areas respectively. a) At very high  $Pe \approx 100$  and thus far in the phase separated region, the slab is stable. b) For  $Pe \approx 41$  close to the critical point, the system's preferential configuration still is a slab geometry. c) But especially close to the critical point, the fluctuations increase and the slab becomes less stable. Bubbles and even rifts can appear. These, in turn, can influence the determination of the center of mass, resulting in a non-ideal measurement close or even in the interfacial region. d) For low propulsion strengths ( $Pe \approx 35$ ), the system is in a homogeneous state.

Exemplary snapshots and the corresponding measurement areas are shown in Figure 8.4. Panel a) shows an example of the geometry at  $Pe \approx 100$ . This is far above the region examined here. Nonetheless, it gives an impression of the slabs at high velocities that were used to extract the binodal densities. Closer to the critical point, at  $Pe \approx 41$  the system still favors the slab geometry as shown in Panel b). However, the densities of the dense and the dilute region have become much more similar and the interface is much more diffuse. In total, the slab becomes less stable. Fluctuations increase and bubbles or even rifts can appear. As shown in Panel c) this can influence the determination of the COM and thus lead to non-ideal measurements close or in the worst case even in the interfacial region. Below the critical point, the slab eventually dissolves, giving way to a homogeneous state. An exemplary snapshot of this geometry, albeit still close to criticality, is shown in Panel d) ( $Pe \approx 35$ ). Qualitatively, this evolution is equivalent to that in equilibrium as seen in the 2D Ising and LJ models. However, the fluctuations in ABPs are more severe and thus the slab's stability is reduced. Even though this means, that the weight of measurements in the interfacial region is larger in ABPs than in the corresponding equilibrium systems, the improved method still allows to exclude most of the misleading measurements and thus still should be able to predict the critical propulsion strength more accurately than the original subsystem distribution method.

Nonetheless, the issue of instability becomes more severe for larger systems. Here bubbles and rifts become more frequent and more persistent. In fact, this issue is the main reason for larger subsystems to be excluded from the analysis. For small subsystems, in turn, the slab is too stable, in most cases not forming multiple grains that move and turn with respect to each other but a single hexagonal structure. This also distorts the measurements and thus very small subsystems also have to be excluded from the analysis. While this restriction of subsystem sizes is present also in other subsystem schemes [143], it is somewhat unsatisfactory, that even the improved subsystem scheme is not able to circumvent such constraints. Nevertheless, the new method still promises an improvement over the other efforts so far, which is especially visible studying the packing fraction distributions.

Analogously to Figure 7.2, we first study the evolution of the packing fraction distribution for different  $\ell$  going through the critical point. The results for the largest and smallest system sizes studied here are shown in Figure 8.5. Only a small interval of propulsion strengths around the critical point is shown. Therefore, neither the strongly double peaked limit nor the Gaussian limit are reached far above or below the critical point respectively. Nonetheless, all system sizes show the evolution from a weakly (if at all) double peak structure at  $Pe \approx 35.42$  below the critical point towards a much more pronounced double peaked structure above the critical point at  $Pe \approx 44.28$ . Most notably, the minimum between the peaks at high  $Pe$  is more pronounced, meaning deeper, than that measured in the original subsystem

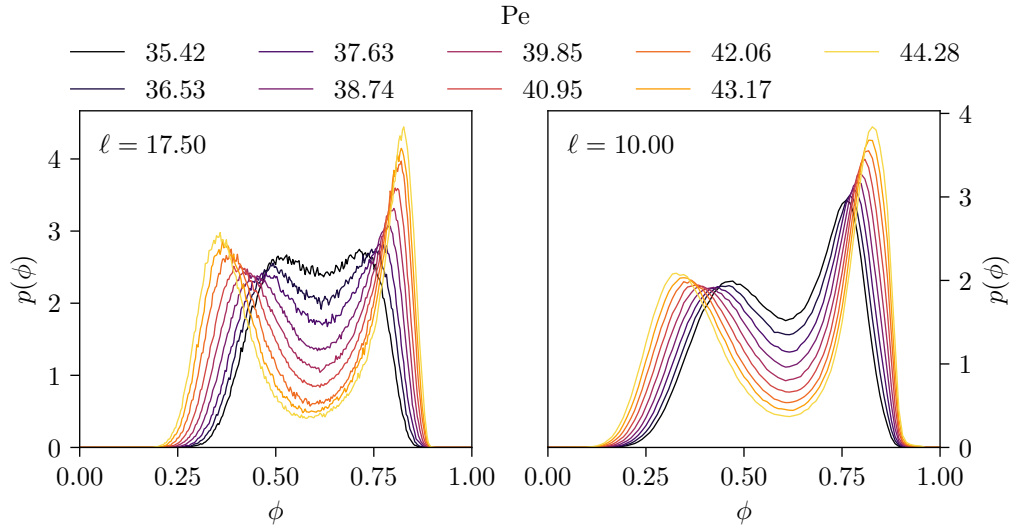


**Fig. 8.5.:** Plots of the packing fraction’s probability distribution in subsystems for different subsystem sizes  $\ell$  and their dependence on the propulsion strength  $Pe$  employing the improved subsystem distribution method: Equivalently to Figure 7.2, the subplots correspond to one of the examined subsystem sizes  $\ell$ . Each of them shows the dependence of  $p(\phi)$  on the propulsion strength  $Pe$ . For the smallest subsystem (bottom right), the change is more gradual, showing a more and more pronounced double peaked structure for increasing  $Pe$ . In contrast, for the largest subsystem (top left), the change is much more pronounced. While the distribution is sharply double peaked at high propulsion strengths, this double peaked structure all but disappears for the smallest simulated value.

scheme (cf. Figure 7.2). Quantitatively, there are again some differences between the different system sizes. The largest system with  $\ell = 17.5$  shown in the top left corner shows a nearly single peaked structure at the lowest  $Pe$  and two strong separated peaks at the highest propulsion strength. These differences are less and less pronounced for smaller  $\ell$ , resulting in more gradual changes. This difference between system sizes nicely agrees with the expectations on which the method of crossing  $Q_\ell$  is based.

As explained in the Section 7.5, the main problem of the original subsystem scheme was the overexpression or interfaces in the measurement boxes and as a result the overestimation of the weight of intermediary packing fractions at high propulsion strengths. The improved subsystem scheme specifically aims at reducing these distortions. Figure 8.6 highlights the differences in the packing fraction distribution above the critical point at  $Pe \approx 44.28$  showing the results of the improved and the original method on the left and right respectively. The most notable difference is the much sharper form of the peaks for all  $\ell$  in the improved method shown in the left panel. In comparison, the double peaked structure of the distribution measured in the original scheme is much less pronounced. Another important difference between the methods can be seen by separately comparing the curves for different  $\ell$ . The failure of the old method to show the correct order of the minima’s heights above

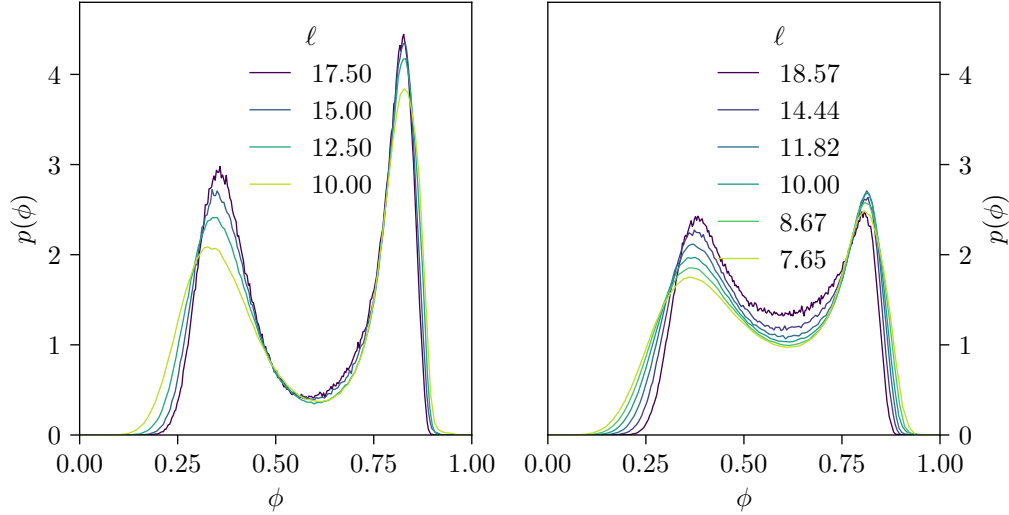


**Fig. 8.6.:** Effect of the new method on the packing fraction distribution  $p(\phi)$ : The plot compares  $p(\phi)$  measured applying the new method on the left with those using the old method on the right at the same propulsion strength  $Pe \approx 44.28$ . As seen in Figure 7.9 for even higher  $Pe$ , due to the presence of interfaces, the distribution is not showing the expected sharp double peaked structure using the old method. Applying the new method, in turn, leads to a more sharply peaked structure. Even though the curves still do not show the correct order at intermediary packing fractions (going from small values for large subsystems to larger values for small subsystems), they are much closer together. These differences demonstrate the advantages of suppressing the measurements in the interfacial region.

the critical point was already discussed in Figure 7.9 for an even higher propulsion strength  $Pe \approx 55.34$ . At this lower  $Pe$  the incorrect order is also present, although the differences are slightly less drastic. In the improved scheme, the minima do not clearly show the correct order either. Nevertheless, they are very close to each other. At even higher propulsion strength, they might even reach the correct order. Therefore, this feature of the packing fraction distribution seems to be captured significantly better by the improved subsystem distribution method. This, in addition to the elimination of the additional scaling variable  $L/\ell$  [28] promises more precise results for the improved method.

After these encouraging preliminaries, a significant computational effort has to be made to extract the packing fraction distribution and as a result  $Q_\ell(Pe)$  with sufficient accuracy. Based on the results gained from the original subsystem distribution, the interval of studied propulsion strengths was limited to nine values in the interval  $Pe \in [34.42, 44.28]$ . Four different system sizes are studied, namely  $\ell = 10.0, 12.5, 15.0, 17.5$ . Therefore, 36 individual data points have to be estimated. As the systems are comparably small, parallelization within individual runs is limited to a few CPU cores. To still gather sufficient statistics between 54 and up to 174 independent runs in case of the large systems in close vicinity to the critical point

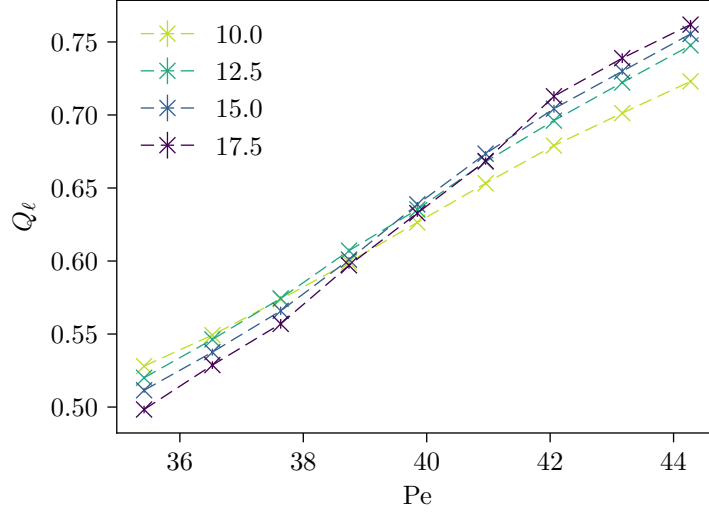


**Fig. 8.7.:**  $Q_\ell$  vs.  $Pe$  measured using the improved subsystem distribution method (Adapted from Figure 2b) of Reference [120], reprinted figure with permission from [J. T. Siebert et al., *Physical Review E*, 93, 030601(R), 2018] Copyright 2018 by the American Physical Society.): For low and high  $Pe$ , the curves show the order expected below and above a critical point respectively. While the curves are ordered going from large to small  $\ell$  at the low end, they show the inverted order for high  $Pe$ . Between  $Pe \approx 37.63$  and  $Pe \approx 42.06$  the curves cross. This gives us an estimate of  $Pe_{cr} = 40(2)$  for the position of the critical point, which is compatible albeit more precise than the estimate of the original method ( $Pe_{cr} = 38(3)$ ).

are performed. Each run consists of a relaxation followed by a production run of at least 800 Brownian times. This substantial computational effort is necessary to reduce the uncertainties sufficiently to extract the intersection point. Compared to the equilibrium simulations, the necessary sampling is significantly higher, which can be attributed to the large fluctuations.

Each individual run is now used to estimate the packing fraction distribution and from it their moments. In contrast to the original subsystem method, the overall packing fraction is not known though and therefore it has to be estimated before the moments can be studied. We thus first estimate  $\langle \phi \rangle$  for every individual run by simple average and then use these estimates to find  $\langle m_2 \rangle = \langle (\phi - \langle \phi \rangle)^2 \rangle$ ,  $\langle m_4 \rangle = \langle (\phi - \langle \phi \rangle)^4 \rangle$ , and finally  $Q_\ell = \langle m_2 \rangle^2 / \langle m_4 \rangle$ . These estimates are then averaged over all runs to find the final estimate and by studying their fluctuations, the associated uncertainties. As it is known from equilibrium simulations, that insufficient sampling can lead to systematical underestimation of the moments of the packing fraction distribution [38], it has been verified, that computing the moments by averaging over batches of runs instead of over individual runs results in no significant differences.

The results of this estimation are shown in Figure 8.7, analogously to those of the original subsystem method in Figure 7.8. In the low- and high- $Pe$  limit, all four

curves corresponding to the examined system sizes show the behavior expected below and above a critical point. While the curve for the largest  $\ell$  is comparably steep, starting out at the smallest  $Q_\ell$  value and crossing to become the largest for high propulsion strengths, the inverse is true for the more gradual increase of the curve corresponding to the smallest  $\ell$ . Between  $Pe \approx 37.63$  and  $Pe \approx 42.06$ , the curves are crossing and as a result inverting their order. As a result, we can estimate the critical propulsion strength to be  $Pe_{cr} = 40(2)$ , which does nicely agree with our estimate found in the original method ( $Pe_{cr} = 38(3)$ ). Even with the improved method, there are still consecutive intersections and thus the resulting uncertainty of the estimate is significantly larger than that of the equilibrium benchmark systems. Nonetheless, the intersection range is narrower than in the old method (cf. Figure 7.8) and there is a significant improvement in accuracy of our estimate. We thus conclude, that, in fact, we have found a critical point in ABPs and have reliably estimated its location along the control parameter to be  $Pe_{cr} = 40(2)$ . The fact that we can find a rather well defined crossing range does support our hypothesis that scaling laws known from equilibrium in fact remain valid in this system far from equilibrium, which is already a remarkable result in itself.

To fully locate the critical point, we still need to find the correct critical packing fraction  $\phi_{cr}$ , which is determined as the average packing fraction in all four subsystems at the critical point. The statistical uncertainty when averaging the density along one individual run and also the standard error computed by comparing multiple independent runs at the same state point and in a system of the same size are both negligibly small. This results in precise estimates for  $\langle \phi_\ell(Pe_{cr}) \rangle$  which show a weak dependence on both the system size as well as our estimate for  $Pe_{cr}$ . Especially due to the dependence on the system size one might be tempted to try an extrapolation to an infinite system size [66]. But only few different system sizes are available and the dependence of  $\langle \phi_\ell(Pe_{cr}) \rangle$  on  $\ell$  turns out to be rather small and to saturate quickly. As furthermore the critical exponents are unknown, no such extrapolation was performed. In contrast,  $\phi_{cr}$  is determined by simply averaging over all state points compatible with our estimate  $Pe_{cr}$  and over all system sizes, which results in an estimate of  $\phi_{cr} = 0.597(3)$ . As explained above, this is an average over different propulsion strengths and system sizes. Thus, the standard deviation of these values, rather than a (meaningless) standard error, is given as a measure of the result's uncertainty. This result is well consistent with the estimation of the critical density which arises from the original subsystem distribution analysis. Here, the critical density can be approximated by the limiting position of the locus of maximum  $Q_\ell$  at criticality. For the largest subsystems, the maximum was reached at values of  $\phi = 0.595(15)$ . We can thus conclude that the critical packing fraction is  $\phi_{cr} = 0.597(3)$ .

Figure 8.8 shows our estimate of the critical point's location in the phase diagram together with the results for the binodal lines that were presented in Figure 4.3.



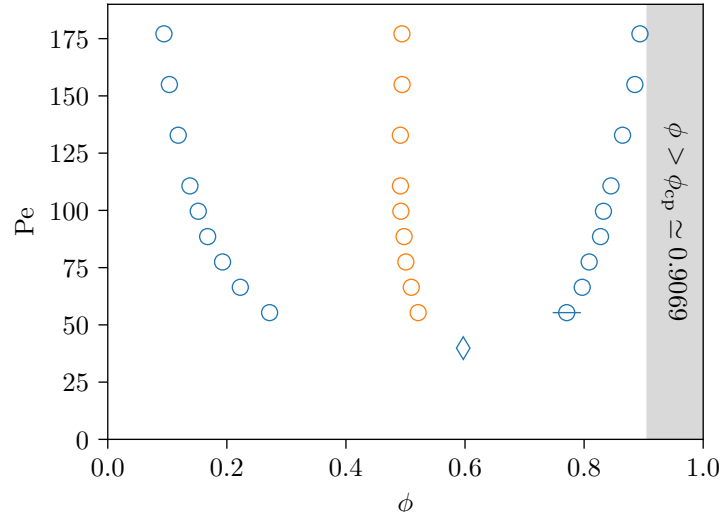


**Fig. 8.8.:** Phase diagram of ABPs including the estimate of the critical point (Adapted from Figure 2a) of Reference [120], reprinted figure with permission from [J. T. Siebert et al., Physical Review E, 93, 030601(R), 2018] Copyright 2018 by the American Physical Society.): In addition to the points on the binodal lines that were already shown in Figure 4.3, a cyan diamond indicates the estimated position of the critical point  $Pe_{cr}$  and  $\phi_{cr}$ .

Here, the binodal lines are shown as blue circles and our estimate of the critical point is shown as an empty blue diamond. Additionally, the diameter is shown again as orange circles. As expected based on the curvature of the diameter at small  $Pe$  and the behavior of the locus of maximum  $Q_\ell$  (cf. Figure 7.7), the critical point does not lie on a linear extension of the diameter but is significantly shifted towards higher packing fractions. This behavior, which is uncommon albeit not unheard of in equilibrium systems [62, 84], is also consistent with other studies of critical behavior in active systems, where the law of rectilinear behavior was found to be violated as well. Note however, that these studies focused on the influence of activity on underlying equilibrium phase transitions [101, 141, 143]. Also the critical propulsion strength  $Pe_{cr} = 40(2)$  is consistent with the results found in the original subsystem distribution method. There,  $Q_\ell(Pe)$  for different subsystem sizes  $\ell$  were found to cross between  $Pe \approx 33$  and  $Pe \approx 41$ . These results, regardless of the method's shortcomings and the resulting drastically reduced precision, thus give a compatible estimate for  $Pe_{cr}$ . Even though this is already a strong indication for our results validity, in the next section we will test whether we can find additional evidence, corroborating our findings.

## 8.5 Alternative bounds on the critical point

In addition to the crossing of  $Q_\ell(\text{Pe})$  curves, there are other indicators which on their own are insufficient to estimate the critical propulsion strength but nonetheless can be used to check the validity of our estimates.

### 8.5.1 Cluster size distribution

To that end, we study the cluster size distribution. In contrast to an earlier study by Fily et al. [43], who studied its dependence on the packing fraction at high propulsion strengths in the phase separated regime, we focus on the evolution of the distribution at constant packing fraction but increasing the propulsion strength through our estimate of the critical point. We define a cluster by the Stillinger criterium [135] as a group of connected particles. Two particles are considered to be pairwise connected if their distance is smaller than the cutoff radius  $2^{1/6}$ , meaning that they interact with each other. Based on this criterion, the cluster size distribution was determined for the simulations that were also used for the original subsystem analysis. Therefore, the box is of size  $130 \times 130$ . A packing fraction of  $\phi = 0.59 \approx \phi_{\text{cr}}$  was chosen.

The left panel of Figure 8.9 shows the resulting cluster size distribution normalized with respect to the probability of the single particle cluster for propulsion strengths in the interval  $33.21 \leq \text{Pe} \leq 44.28$ . The different  $\text{Pe}$  are color-coded going from black to orange respectively. The two panels on the right show the curves for the smallest ( $\text{Pe} \approx 33.21$ ) and the largest ( $\text{Pe} \approx 44.28$ ) propulsion strengths in isolation. All curves are comparably close to our estimate of the critical point ( $\text{Pe}_{\text{cr}} = 40(2)$ ) and thus the overall behavior is somewhat similar. At low particle numbers all curves show a power-law-like decay. However, at the lowest propulsion strength, the power law goes over into a steep decay at roughly  $N \approx 1000$ , whereas at the highest propulsion strength, the distribution decays quicker much earlier but shows a non-monotonic behavior, namely a peak at  $N \approx 5000$ . Note, that the power-law-like decay does not imply that the system is at criticality [21]. We thus cannot derive a lower bound for  $\text{Pe}_{\text{cr}}$  from this analysis. Nonetheless, the formation of relatively stable large scale clusters as indicated by the peak at high particle numbers for  $\text{Pe} \approx 44.28$  suggests that this system is in fact above the critical point in the phase separated region.

Obviously, the difference between homogeneous or critical systems and the phase separated system at  $\text{Pe} \approx 44.28$  is more gradual than one might expect. Rather than showing a strict power-law-like decay, as expected for simulations along the correct

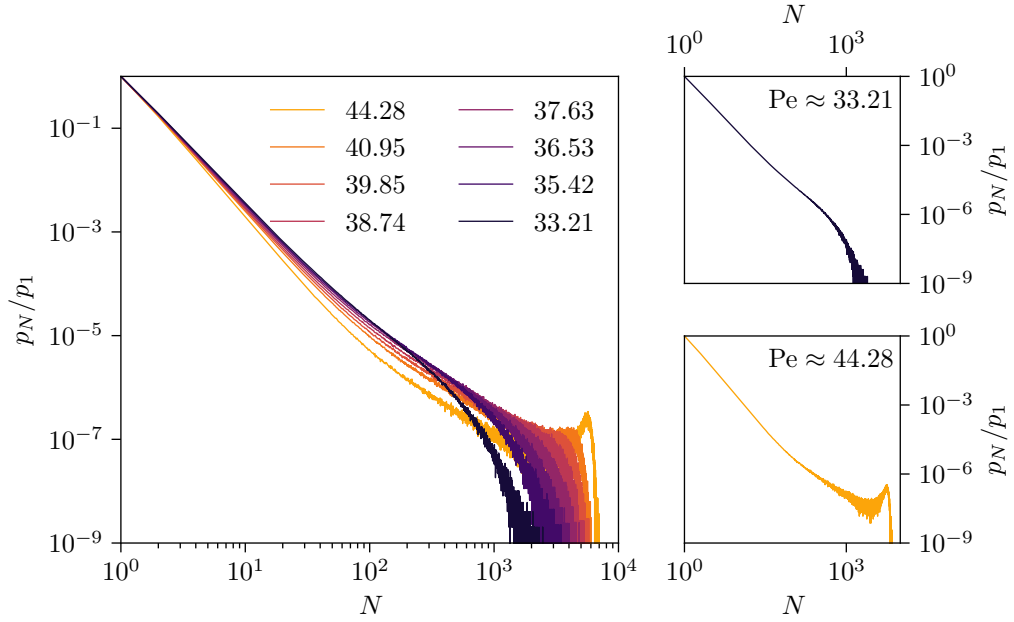


**Fig. 8.9.:** Cluster size distribution close to the critical point: The curves show the cluster size distribution in a  $130 \times 130$  simulation box at an overall packing fraction close to the critical packing fraction ( $\phi = 0.59$ ). The curves are normalized with the probability of a single particle cluster. The two panels on the right show the curves for the smallest ( $Pe \approx 33.21$ ) and the largest ( $Pe \approx 44.28$ ) propulsion strengths in isolation.

locus in equilibrium [21], all curves show a shoulder at large cluster sizes  $N$ . This shoulder is growing for increasing  $Pe$  and becomes non-monotonic at  $Pe \gtrsim 40$ . These distortions can have multiple causes. Simulations take place at a constant density close to the critical density which might not coincide with the percolation line [21]. Generally, the percolation threshold depends on the cluster definition and only for proper cluster definitions, the percolation threshold ends at the critical point [23]. Furthermore, simulations take place in a finite box with a fixed particle number. All these effects could arise in equilibrium systems as well, systematic distortions due to the non-equilibrium nature of the system cannot be ruled out either.

In conclusion, our analysis of the cluster size distribution allows a tentative estimate of an upper bound on the critical point ( $Pe_{cr} < 44.28$ ), which agrees well with our estimate of  $Pe_{cr} = 40(2)$ . Nonetheless, further studies would be needed to elucidate the onset of percolation and corresponding exponents in ABPs.

## 8.5.2 Static structure factor

After extracting an upper bound on the critical propulsion strength from the cluster size distribution, we try to extract a lower bound by estimation of the correlation

length from the static structure factor  $S(q)$  at low  $q$  values as suggested by Fily and Marchetti [42]. There exists high quality data on the structure factor of ABPs in the homogeneous region. Macedo Biniossek et al. [81] evaluated the dependence of the structure factor on multiple parameters, namely the packing fraction, propulsion velocity and reorientation time. While these results can serve as a great reference especially for theoretical work in the future [81], our focus is not on studying the general structure of the homogeneous active fluid but we are specifically interested in examining the structure factor in the critical regime. We thus use the extensive simulations performed to apply the original subsystem distribution method to extract high precision estimates for the static structure factor in this region of the phase diagram.

To extract precise values for low  $q$ ,  $S(q)$  is evaluated not as the Fourier transform of the radial distribution function but by directly summing over all particles [52, p. 98]:

$$S(\mathbf{q}) = \left\langle \frac{1}{N} \sum_{k,l} \exp(-i\mathbf{q}(\mathbf{r}_k - \mathbf{r}_l)) \right\rangle, \quad (8.2)$$

where  $\langle \cdot \rangle$  refers to a time average along a trajectory. As our system is isotropic, the dependence on  $\mathbf{q}$  simplifies to a dependence on  $q = |\mathbf{q}|$ . The underlying simulations are again those used for the original subsystem method. Because of the periodic boundary conditions and the box size  $L = 130$ , only  $q$  values of the form  $q = \frac{2\pi n}{L}$  with  $n \in \mathbb{N}$  can be considered. The smallest  $q$  value is thus  $q_{\min} = \frac{2\pi}{130} \approx 0.048$ . Analogously to the analysis of the cluster size distribution, a locus of constant packing fraction at  $\phi \approx 0.59$  is used in the analysis.

The results are shown in Figure 8.10. Different propulsion strengths are shown in colors going from purple ( $Pe \approx 33.21$ ) to orange ( $Pe \approx 40.95$ ). All curves show multiple peaks, with the first being located roughly at  $q = 2\pi$  corresponding to particles in contact. Going to lower  $q$  values, all curves show a minimum and an subsequent increase. For low  $Pe$ , this increase flattens going towards  $q \rightarrow \frac{2\pi}{L}$  but increasing  $Pe$ , the curves approach a power-law divergence with an exponent close to  $-2$ . This is in accordance with scaling theory predicting a divergence following  $S(q) \propto q^{-2+\eta}$  at the critical point [45]. In our finite system this exponent will only hold for  $\frac{2\pi}{L} \ll q \ll \frac{2\pi}{D}$  where  $D$  is the typical distance of particles in the system. Below the critical point, the curve is not diverging but following a Lorentzian with argument  $\xi q$ , resulting in a dependence on the correlation length  $\xi$ . We thus expect  $S(q)$  to follow this modified Ornstein-Zernicke form [45, 42]:

$$S(q) = \frac{S_0}{1 + (\xi q)^{2-\eta}} \quad (8.3)$$

at least for  $\frac{2\pi}{L} \ll q \ll \frac{2\pi}{D}$ .

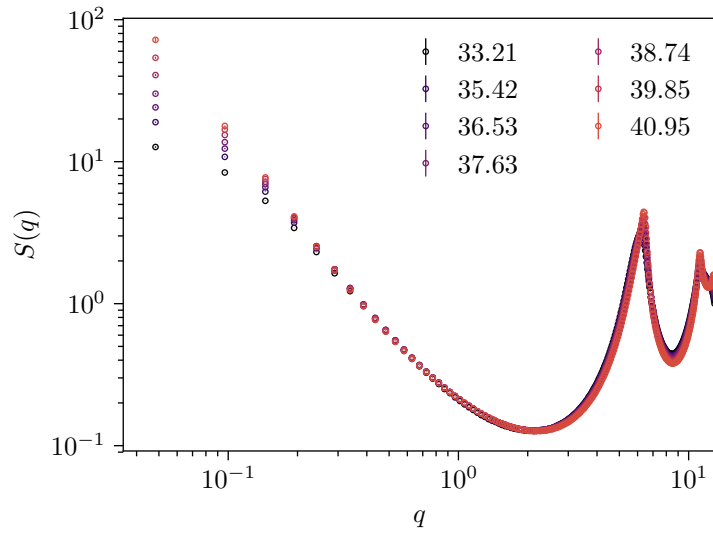


**Fig. 8.10.:** Static structure factor for different  $Pe \lesssim Pe_{cr}$ :  $S(q)$  is shown in colors going from dark purple to orange for propulsion strengths  $Pe \approx 33.21$  up to  $Pe \approx 40.95$ , respectively. While all curves show multiple peaks, for low  $q$  there is a significant difference between the different propulsion strengths. For increasing  $Pe$  the curves approach a power-law divergence.

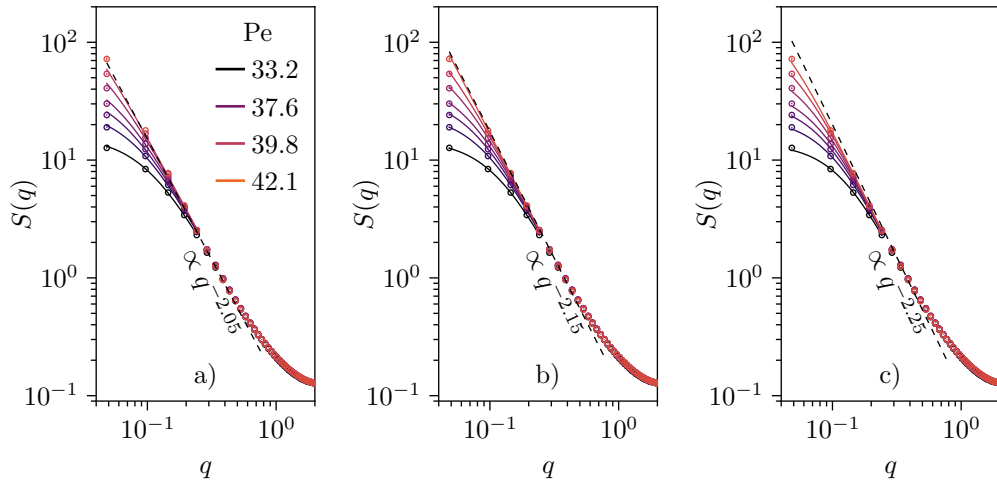


**Fig. 8.11.:** Static structure factor assuming different values for the anomalous dimension (Adapted from Figure S5 of the SI to Reference [120], reprinted figure with permission from [J. T. Siebert et al., Physical Review E, 93, 030601(R), 2018] Copyright 2018 by the American Physical Society.): Only negative, and thus unphysical values can reproduce the slope's steepness (indicated by the dashed line) as well as the functional form based on Eq. (8.3) (indicated by the fits displayed as solid lines) properly.

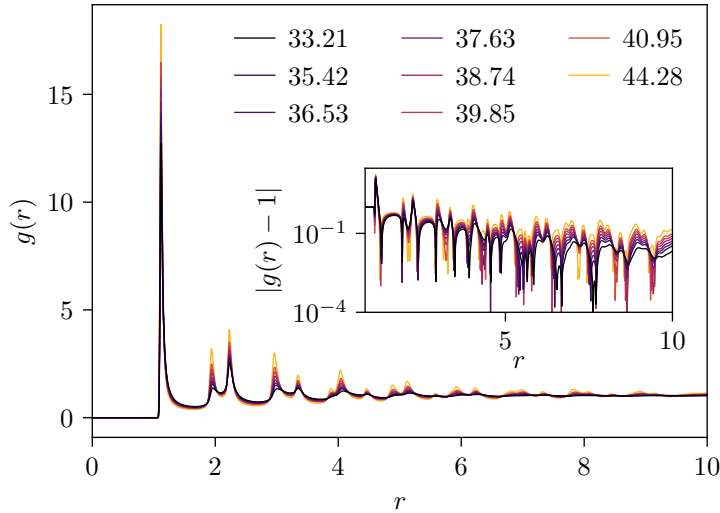


**Fig. 8.12.:** Radial distribution function for different  $Pe$  close to  $Pe_{cr}$ :  $g(r)$  is shown in colors going from dark purple to orange for propulsion strengths  $Pe \approx 33.21$  up to  $Pe \approx 44.28$ , respectively. After a sharp peak at contact, all curves show a significant amount of local structure even for large  $r$ . The inset highlights this by showing  $|g(r) - 1|$  on a logarithmic scale.

Based on the form of  $S(q)$ , it is now tempting to try extracting the anomalous dimension from the limiting slope and subsequently to find an estimate of the correlation length by fitting the structure factor for low  $q$  using Eq. (8.3). By examining the maximum slope, one finds that only a value for the anomalous dimension  $\eta < 0$  is able to properly reproduce the slope as shown for three different  $\eta$  in Figure 8.11 assuming the values  $\eta = -0.05, -0.15, -0.25$ . For those values, the low  $q$  limit of  $S(q)$  can be fitted to Eq. (8.3) reasonably well, whereas  $\eta \geq 0$  does neither reproduce the maximum slope nor the functional form. This value of  $\eta < 0$  is not physical though as it would imply that the order parameter correlations would diverge with increasing distance. Therefore, it seems that a naive extraction of  $\eta$  and  $\xi$  from  $S(q)$  in this finite system and at constant particle number does not give reasonable results. Even the system size of  $L = 130$  that was used to extract these values seems insufficient to reach the power-law dependence of  $S(q) \propto q^{-2+\eta}$ . Rather, strong finite size effects cause a misleading measurement which results in an unphysical estimate of the anomalous dimension.

To understand this failure, we study the radial distribution function shown in Figure 8.12. Different  $Pe$  are shown in a color scheme analogous to Figure 8.10. After a sharp first peak at contact, all curves show multiple additional peaks with a structure much richer than in a simple equilibrium fluid (e.g. a LJ fluid [50, 88]). These stem from the rather strong local order in the grains seen in the fluid (cf. Figure 8.4). They are more pronounced for higher  $Pe$ , where also the decay of the maxima's heights is slowest. Nonetheless, even for the smallest propulsion

strength of  $Pe \approx 33.21$ , which is significantly below  $Pe_{cr}$ , the additional substructure does not disappear within a large radius of 10. To highlight this, and also to show the difference in decay strength, the inset shows  $|g(r) - 1|$  on a logarithmic scale. In a simple fluid,  $g(r)$  is expected to show exponentially dampened oscillations around 1. The decay constant of the resulting envelope around  $|g(r) - 1|$  is given by the correlation length:  $|g(r) - 1| \propto \exp(-r/\xi)$  for  $r$  being larger than the range of the local structure and still significantly smaller than the box length [88, 132]. This regime does not exist in our simulations as the length scale  $r_{hex.}$  of the local hexagonal structure is large enough that  $r_{hex.} < r \ll L$ . Due to the long range of the local order in the pair correlations, caused by large hexagonal grains in the fluid, even a system with side length  $L = 130$  as used here seems insufficient. Rather the asymptotic limit of exponential decay in the fluid structure seems to be reached only for  $r \ll L$ . Therefore, the proper regime to extract the anomalous dimension and correlation length from the static structure factor is not available in a box of our size and much larger systems would have to be used to reach a meaningful estimate. This is hardly achievable as proper relaxation and sampling of such a system would be very expensive computationally.

In conclusion, both the structure factor and the radial distribution function show a behavior that is consistent with an increasing correlation length.  $S(q)$  approaches a power-law divergence for low  $q$  values when increasing  $Pe$ ,  $g(r)$ 's exponential decay constant  $1/\xi$  becomes smaller for increasing  $Pe$ . Both properties can only be seen qualitatively but cannot be quantified to extract an estimate for the correlation length due to strong finite size effects. Therefore, one can only conclude that the lowest values shown in Figure 8.10 and 8.12 are still significantly below  $Pe_{cr}$ . However, a hard lower bound or even quantitative estimates of the correlation length cannot be extracted. Additional information about this analysis can be found in Appendix A.2. While an extraction of the correlation length and its scaling behavior by analysis of the structure factor was not successful, we will see in the next section that other critical exponents can indeed be extracted.





## Critical exponents

The determination of the critical point in ABPs is in itself already a major result, completing our determination of the phase diagram in the area of the gas liquid transition. Nonetheless, the exact position of the critical point is strongly model dependent. Thus, comparison with results of other models does not yield any significant insight and it does not answer the question of existence of universality far from equilibrium. Naively, it seems to be tempting to compare  $Q_\ell$  at the intersection point to determine whether the system belongs to a certain universality class. This would be misleading though, as this value is only universal along different models but it is not independent of box geometry and boundary conditions [119]. We can already see this difference by comparing the intersection points of the original and the improved subsystem distribution method, which differ significantly. Nonetheless, our determination of the critical point's position allows us to determine critical exponents, which in turn can be compared to exponents found in other universality classes, to determine whether ABPs fall into one of these classes known from equilibrium. An especially likely candidate would be the Ising universality class, which is shared by equilibrium systems featuring a critical point and a phase transition with one-dimensional order parameter as well as only short range interactions [77]. Furthermore, if these exponents would not match those of the Ising universality class, comparison with different systems might allow insights into the question about the existence of a non equilibrium "active" universality class. Therefore, in the remainder of this section we will determine critical exponents and compare them with the values known for Ising-like systems in equilibrium (cf. Table 2.1). This chapter completes the recapitulation of the material in Ref. [120].

### 9.1 Order parameter exponent $\beta$

First, we will try to estimate the order parameter exponent. As described in Eq. (2.13), the mean order parameter  $\langle m \rangle = \langle \phi_{\text{liq}} \rangle - \langle \phi_{\text{gas}} \rangle$ , measured in the phase separated region but still close to criticality, is expected to follow a power-law increase in terms of the dimensionless distance to the critical point

$$\tau = \frac{\text{Pe}^{-1} - \text{Pe}_{\text{cr}}^{-1}}{\text{Pe}_{\text{cr}}^{-1}}. \quad (9.1)$$

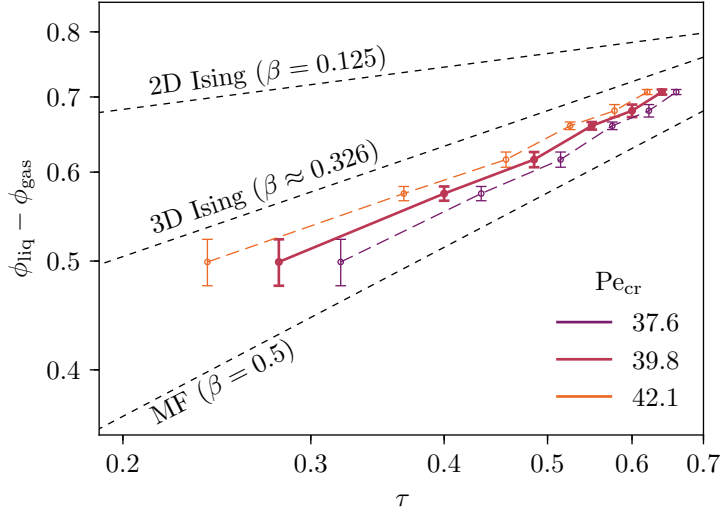


**Fig. 9.1.:** Scaling plot of the order parameter against  $\tau$  (Adapted from Figure 3a) of Reference [120], reprinted figure with permission from [J. T. Siebert et al., Physical Review E, 93, 030601(R), 2018] Copyright 2018 by the American Physical Society.): Close to the critical point, the mean order parameter shows a power-law dependence on the distance to the critical point  $\langle m \rangle \propto \tau^\beta$ . Plotting  $\langle m \rangle$  against  $\tau$  on a double logarithmic scale thus should result in a line with slope  $\beta$ . To account for the rather large uncertainties in determining the critical point, we show three curves corresponding to our best estimate, as well as generous lower and upper bounds shown as thick and dashed lines respectively. Estimation of the slopes by a linear fit results in  $\beta \approx 0.40, 0.45, 0.50$  in increasing order of steepness. For reference, Ising and MF slopes are indicated by dashed lines.

The exponent in the resulting power law,  $\langle m \rangle \propto \tau^\beta$ , is known as the order parameter exponent and has a value of  $1/8$  for 2D Ising universality.

To extract  $\beta$ , we study the dependence of the distance of corresponding points on the binodals, determined in Chapter 4, on their respective dimensionless distance from the critical point. The resulting relation is shown in Figure 9.1 in a log-log plot. The three curves correspond to our best estimate as well as generous upper and lower bounds for the critical propulsion strength. They are shown as thick and dotted lines respectively. These three separate curves are shown to avoid the misleading conclusion that this uncertainty is independent for the different points along each curve. On the contrary, they all share the same deviation from the true curve as can be seen by studying  $\tau$ 's dependence on  $\text{Pe}_{\text{cr}}$  (cf. Eq. (9.1)) and thus the  $\tau$  values will either be all over- or all underestimated. To give a well founded answer about the uncertainty of the resulting slope, this has to be considered. On the other hand, the uncertainties in determining the binodals are truly statistical and mutually independent. Thus, they are shown as error bars. The uncertainties in both directions are rather large, especially close to the critical point. Therefore, it is not possible to give a meaningful estimate of  $\beta$  with a corresponding uncertainty.

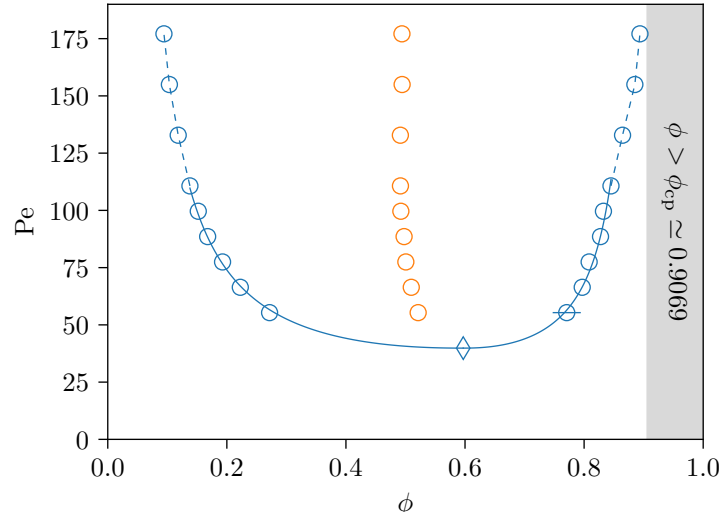


**Fig. 9.2.:** Phase diagram of ABPs including a fit of the binodals close to  $Pe_{cr}$  (Adapted from Figure 2a) of Reference [120], reprinted figure with permission from [J. T. Siebert et al., Physical Review E, 93, 030601(R), 2018] Copyright 2018 by the American Physical Society.): Based on our best estimate of the order parameter exponent  $\beta \approx 0.45$  and the position of the critical point, the binodal lines can now be completed by fitting the dense and dilute branch close to the critical point ( $Pe < 111$ ). These fits are shown as solid lines. The dashed connecting lines at high  $Pe$  are only meant as guides for the eye.

Nonetheless, we can compare the resulting slope with that corresponding to 2D Ising universality. As reference this as well as 3D Ising and Mean Field slopes are shown as dotted lines. Comparing the results for ABPs with the 2D Ising slope, we can conclude that despite the large uncertainties, the slope and thus  $\beta$  for ABPs is significantly larger than that corresponding to 2D Ising universality. This is thus a first indication that ABPs do not follow the 2D Ising universality class. It is only a rather weak indication though, as the uncertainties associated with both the binodal lines as well as the position of the critical point are rather large. Furthermore, even the lowest propulsion strengths for which the binodals have been estimated are quite far from the critical point such that the scaling regime is not yet reached necessarily.

Despite the large uncertainties, we can still extract an estimate of  $\beta \approx 0.45(5)$  based on a linear fit to the thick, as well as the dashed lines in Figure 9.1. Albeit this estimate's rough nature, we can still use it to get an idea about the binodals' behavior between the lowest points that were extracted via direct measurement and the critical point. Based on the known scaling behavior of the order parameter  $m \propto \tau^\beta$ , we fit both branches separately with a power law

$$\phi_{\text{gas/liq}}(\tau) = \phi_{cr} + b_{\text{gas/liq}}\tau^\beta, \quad (9.2)$$

where  $\phi_{\text{cr}}$  and  $\tau$  are based on our best estimate for the critical point and  $b_{\text{gas/liq}}$  are fitting parameters [131]. Obviously, there could be other contributions, such as a linear offset, canceling out in the computation of  $m$ . These additional contributions are neglected here. The resulting fits are shown in Figure 9.2 as solid blue lines. The points on the binodals that were not considered in the fitting due to their large distance to the critical point, are connected by dotted lines as guides for the eye. The lower points on the binodal are consistent with the fit. Note however, that also other values for  $\beta$  are able to reproduce the behavior to some degree, especially considering deviations in the position of the critical point. 2D Ising universality ( $\beta = 1/8$ ) seems highly unlikely, though, as the resulting abrupt increase is inconsistent with our estimates for the binodal lines.

## 9.2 Correlation length exponent $\nu$

One way to estimate the correlation length exponent is to study the system size dependence of the slope of  $Q_\ell(\tau)$  at the critical point. The slope  $dQ_\ell/d\tau|_{\tau \approx 0}$  is predicted to follow a power law with respect to  $\ell$  in the vicinity of the critical point [13]

$$dQ_\ell/d\tau|_{\tau \approx 0} \propto \ell^{1/\nu}. \quad (9.3)$$

Therefore, a good estimation of the derivative  $dQ_\ell/d\tau|_{\tau \approx 0}$  allows to find the correlation length exponent. The correlation length itself is difficult to estimate (see Section 8.5.2) and thus a direct observation of its scaling behavior is not easily achievable. An indirect estimation of the exponent is thus required.

This method is especially well suited for our analysis as the slope varies only slowly along  $Q_\ell(\tau)$  and thus a robust estimation of  $dQ_\ell/d\tau|_{\tau \approx 0}$  is possible even when the uncertainty in the estimation of the critical point is large. The behavior of  $Q_\ell(\tau)$  for different system sizes in the vicinity of the critical point is shown in Figure 9.3. The data points are shown as crosses with error bars. To estimate the derivative of  $Q_\ell(\tau)$ , we fit a linear function to each curve for the respective system size over the full range in which we estimate the position of the critical point. The resulting fits are shown as solid lines. These lines reproduce the data points well and thus we can hope that the resulting estimation of the derivative  $dQ_\ell/d\tau|_{\tau \approx 0}$  is robust with respect to uncertainties in estimating  $P_{\text{e,cr}}$ . Visual inspection of the slopes already reveals the expected behavior of increasing slopes for increasing system sizes.

Figure 9.4 now shows the resulting estimates for the derivative and their dependence on  $\ell$  in a log-log plot. The power-law behavior  $dQ_\ell/d\tau|_{\tau \approx 0} \propto \ell^{1/\nu}$  predicts a line in log-log scale with a slope corresponding to  $1/\nu$ . The black dotted lines again show the slopes corresponding to 2D Ising ( $1/\nu = 1$ ), 3D Ising ( $1/\nu \approx 1.59$ ) and mean

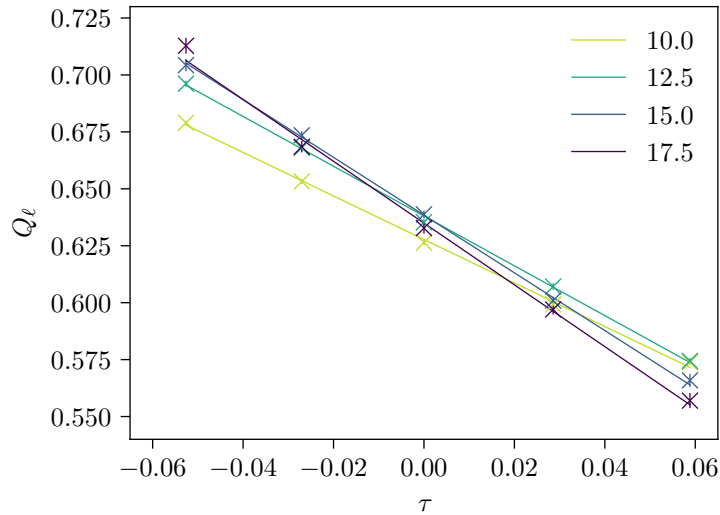


**Fig. 9.3.:** Linear fit of  $Q_\ell(\tau)$  at the crossing point to extract  $dQ_\ell/d\tau|_{\tau \approx 0}$ : Finite size scaling theory also predicts a power-law dependence of the slope of  $Q_\ell(\tau)$  at the critical point  $dQ_\ell/d\tau|_{\tau \approx 0} \propto \ell^{1/\nu}$  [13]. To extract said slope, a linear function, shown as full lines, is fitted to  $Q_\ell(\tau)$ , displayed as crosses. The fit reproduces the linear behavior rather well along the full range where the critical point is estimated.

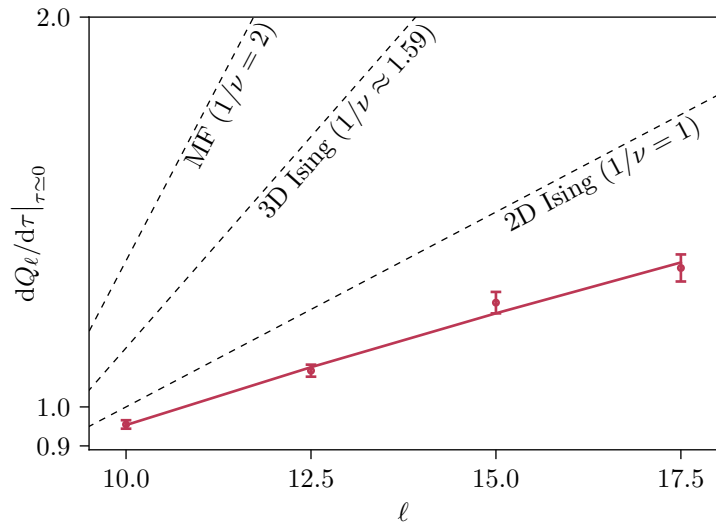


**Fig. 9.4.:** Scaling plot of  $dQ_\ell/d\tau|_{\tau \approx 0}$  against  $\ell$  (Adapted from Figure 3c) of Reference [120], reprinted figure with permission from [J. T. Siebert et al., Physical Review E, 93, 030601(R), 2018] Copyright 2018 by the American Physical Society.): The  $\tau$  derivative of  $Q_\ell(\tau)$  is expected to have a power-law dependence on  $\ell$ :  $dQ_\ell/d\tau|_{\tau \approx 0} \propto \ell^{1/\nu}$ . The four data points show the estimates for the derivative for the different system sizes examined here. Three dashed lines show the slopes corresponding to 2D Ising ( $1/\nu = 1$ ), 3D Ising ( $1/\nu \approx 1.59$ ) and mean field ( $1/\nu = 2$ ) behavior in increasing order of steepness for reference. The exponent found for ABPs (solid line,  $1/\nu \approx 0.65(4)$ ) is significantly lower than that of 2D Ising universality, indicating  $\nu > 1$  for ABPs.

field ( $1/\nu = 2$ ) behavior in increasing order of steepness for reference. The exponent found for ABPs (solid line) is significantly lower than that of 2D Ising universality which again indicates that ABPs are unlikely to fall into the equilibrium universality class of 2D Ising. The fit shown as the solid line in Figure 9.4 rather predicts a value of  $1/\nu \approx 0.72$  and thus  $\nu \approx 1.5 > 1$ .

### 9.3 Another quotient of critical exponents $\gamma/\nu$

Finally, we will estimate another quotient of exponents  $\gamma$  and  $\nu$ . For this, we study the system size dependence of the susceptibility

$$\chi_\ell = \frac{\langle (N_\ell - \langle N_\ell \rangle)^2 \rangle}{\langle N_\ell \rangle}. \quad (9.4)$$

Assuming that usual scaling laws are valid, this susceptibility in the infinite system size limit follows the scaling law  $\chi_\infty \propto \tau^{-\gamma}$  (see Eq. (2.14)). The dependence of the finite size susceptibility is then given by

$$\chi_\ell = \chi_0(\ell/\xi)\xi^{\gamma/\nu} = \ell^{\gamma/\nu}\tilde{\chi}(\ell/\xi), \quad (9.5)$$

where it is assumed that the scaling function  $\tilde{\chi}$  only depends on the quotient  $\ell/\xi$  [74, 141, 143]. Additionally, it was used that the correlation length in a finite system with periodic boundaries is bounded by the box dimension. Based on that observation, in the vicinity of the critical point,  $\ell/\xi$  becomes independent of the system size for our method and thus the only  $\ell$  dependence of  $\chi_\ell$  is given by the prefactor  $\chi_\ell \propto \ell^{\gamma/\nu}$ . Consequently, we can thus extract  $\gamma/\nu$  by studying the susceptibility's system size dependence.

Figure 9.5 shows a log-log plot of said dependence. Analogously to Figure 9.1, the three colored curves correspond to our best estimate for  $P_{e_{cr}}$  (thick points and line) as well as generous upper and lower bounds. The points show the results extracted from simulations. The lines show linear fits to these data points, which reproduce their behavior very well. For reference, three dotted lines indicate the slopes corresponding to 2D Ising ( $\gamma/\nu = 7/4$ ), 3D Ising ( $\gamma/\nu \approx 1.96$ ), and mean field ( $\gamma/\nu = 2$ ) universality. Even the curve for the generous upper bound of  $P_{e_{cr}} \approx 42.1$  shows an increase that is slightly but still statistically significantly lower than that of 2D Ising universality. The other curves indicate even lower exponents. We can thus conclude that  $\gamma/\nu$  in ABPs seems to be lower than for 2D Ising universality.

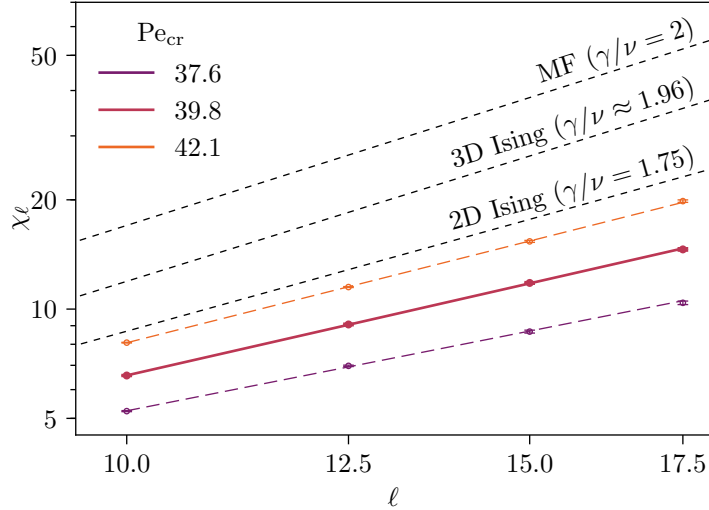


**Fig. 9.5.:** Scaling plot of  $\chi_\ell$  vs.  $\ell$  (Adapted from Figure 3b) of Reference [120], reprinted figure with permission from [J. T. Siebert et al., Physical Review E, 93, 030601(R), 2018] Copyright 2018 by the American Physical Society.): In the homogeneous region but close to the critical point, the finite size susceptibility  $\chi_\ell$  has a power-law dependence on the system size with exponent  $\gamma/\nu$ :  $\chi_\ell \propto \ell^{\gamma/\nu}$  [74]. This again is a rather robust method to estimate critical exponents as the relation is valid as soon as the correlation length sufficiently diverges to reach the limiting value of the box size. Analogously to Figure 9.1 the curves corresponding to our best estimate for  $Pe_{cr}$  as well as generous upper and lower bounds are shown as solid and dashed lines respectively. The corresponding slopes are found as  $\gamma/\nu \approx 1.25, 1.44, 1.59$  in increasing order of steepness. Again, the dotted black lines show slopes corresponding to equilibrium universality classes for reference.

## 9.4 Consistency checks and outlook

In conclusion, the results of the improved subsystem distribution method indicate that ABPs do not fall into the equilibrium universality class of 2D Ising. Figures 9.1, 9.4, and 9.5 compare the exponents  $\beta$ ,  $\nu$ , and  $\gamma/\nu$  to their 2D Ising counterparts and even generous bounds on our estimate for the critical point are incompatible with the 2D Ising reference values. Using rough estimates of critical exponents ( $\beta \approx 0.45$ ,  $\nu \approx 1.5$ , and  $\gamma \approx 2.2$ ), we can tentatively check the scaling relation  $\gamma + 2\beta = 2\nu$ . It is approximately satisfied, especially considering the large numerical uncertainties. This, in turn, serves as a provisional consistency check. Nonetheless, the uncertainties in our determination of the critical point are still considerable. Therefore, we currently cannot definitively answer the question of the existence of an "active matter" universality class. Future work on other active systems, such as run-and-tumble particles [137] or ABP-like agents on a lattice [157] might give insights into the universality of the exponents found in our analysis.





## Conclusion and outlook

In this thesis, we have studied the non-equilibrium phase transition of active Brownian particles (ABPs). A main focus of the work lied on studying the phase behavior and on providing precise, quantitative estimates of the position of the phase boundaries. To that end, Chapter 4 demonstrated how the binodal lines of standard ABPs can be estimated over a wide range of propulsion strengths via extraction of co-existing densities in a phase separated slab geometry. With this method, which was established originally in equilibrium physics, precise, quantitative, and most importantly finite-size independent estimates of the binodal lines were found, only excluding the vicinity of the critical point. We thus provided greatly improved estimates, which not only give insights into the analogy between this non-equilibrium transition and corresponding gas-liquid transitions in equilibrium by itself, but also served as basis for our subsequent studies.

Due to the non-equilibrium nature of the model system, proper definitions for thermodynamic properties cannot necessarily be carried over from equilibrium thermodynamics. While the phase boundaries are defined in terms of the packing fraction, for which no extensions of the equilibrium definition are necessary, we have also studied the notion of an active pressure, based on the definition of Takatori et al. [139]. In Chapter 5, it was explained that this extension to the mechanical definition of a pressure known from equilibrium is necessary to explain the stable phase separation seen for sufficiently high propulsion strengths. To check the validity of the definition, we explicitly verified its intensiveness by examining it in a phase separated system. However, studying the pressure in the interface region indicated that the interfacial tension of the system is negative, which in turn ends the analogy to equilibrium, where a negative interfacial tension would lead to instability of the phase separation. In this, we have found an intriguing true non-equilibrium effect. To improve upon these results and to allow for an easier examination of additional state points, one major goal of further studies should be to find an alternative pressure definition that in contrast to the definition used in this work is not based on the absolute position of the particles. Furthermore, there are groups working towards a thermodynamic theory of ABPs, searching for analogues to other thermodynamic quantities. Especially, a derivation of an analogue to the equilibrium chemical potential would be of great interest, as it could in turn allow to perform grand canonical (GC)-like simulations for ABPs.

Going beyond the standard definition of ABPs, in Chapter 6 we studied how different changes to the model influence the phase behavior and the exact onset of the phase transition. To that end, we examined both the influence of anisotropic particle shape by determination of the phase diagram of different kinds of active Brownian dimers (ABDs) as well as the influence of dimensionality by studying the transition in three-dimensional ABPs. It turned out that both factors reduce the tendency to phase separate and delay the onset of phase separation towards higher propulsion strengths. Furthermore, the influence of the shape as well as the specific method to introduce the active propulsion was understood via a simple mapping procedure. The delayed onset of phase separation in three dimensions was explained by the reduced orientational decorrelation time.

Finally, the last chapter focused on the region of the phase diagram that, until then, had been exempted from the analysis, namely the region around the critical point. Different variants of subsystem distribution methods were applied to locate the exact position of the critical point. By stepwise refinement of the methodology and consequently the precision of our estimate, we were able, for the first time, to give a quantitative estimate of the critical point's position in ABPs based on finite-size scaling theory. This final estimate was found by applying an improved subsystem distribution method, which was originally proposed by Florian Dittrich in his Diploma thesis. After benchmarking the methodology based on equilibrium systems, we found  $Pe_{cr} = 40(2)$  and  $\phi_{cr} = 0.597(3)$  for ABPs. This was corroborated by both the previous analysis using the original subsystem scheme as well as by additional upper and lower bounds on the critical point that were found by examination of the cluster size distribution and the order parameter correlations in form of  $g(r)$  and  $S(q)$ . This concluded our analysis of the phase boundaries, such that we now have precise estimates for them over the full range of the phase diagram.

Additionally, the availability of a good estimate of  $Pe_{cr}$  allowed us to study critical exponents of ABPs. By examination of different scaling laws close to the critical point, we obtained rough estimates for the critical exponents  $\beta$ ,  $\nu$ , and  $\gamma$  and showed that these are incompatible with 2D Ising universality. This final result sparks the interesting question of the existence of an active universality class, which could extend the notion of universality to non-equilibrium phase transitions. Additional work on increasing the precision of the estimate of  $Pe_{cr}$  to eliminate statistical as well as possible systematic errors is needed to find definitive answers to this question though. In addition to improving the methodology to obtain better estimates in case of ABPs, future work studying other active systems such as ABP-like systems on a lattice [157] or run-and-tumble particles [137] could give important insights towards understanding possible universal behavior in active matter.

## A.1 Supplementary Figures

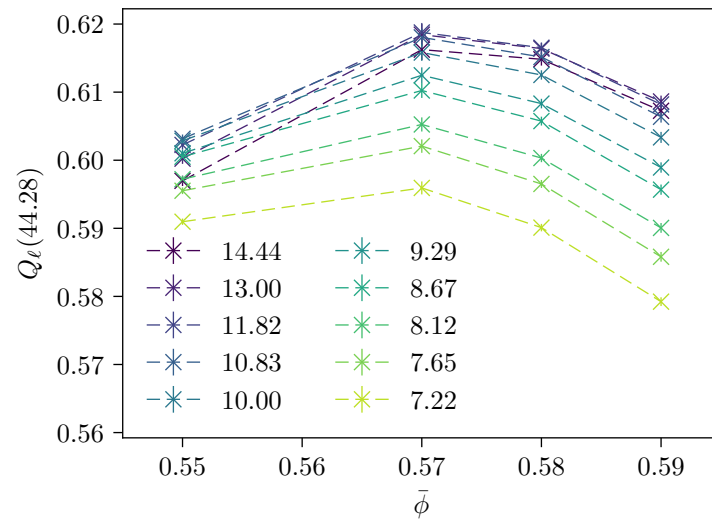


**Fig. A.1.:** Peak of  $Q_\ell$  at  $Pe \approx 44.28$  vs. the average packing fraction  $\bar{\phi}$ : Subsystem sizes are differentiated by colors, going from small subsystems shown in light green to large subsystems shown in dark purple. Connecting lines are plotted as guide to the eye. All curves exhibit a maximum, which lies at a similar position of  $\bar{\phi} \approx 0.57$  for all subsystem sizes. Except for the largest subsystem, the curves are in an order consistent with a system in a phase-separated regime (going from small  $Q_\ell$  for small  $\ell$  towards larger values for larger subsystems).

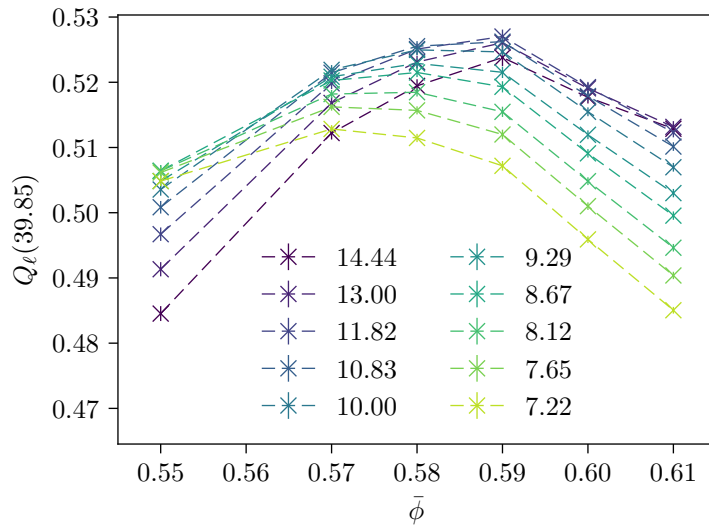


**Fig. A.2.:** Peak of  $Q_\ell$  at  $Pe \approx 39.85$  vs. the average packing fraction  $\bar{\phi}$ : Plot analogous to Figure A.1 for  $Pe \approx 39.85$ . All but the largest two subsystems still show the order corresponding to the two-phase region. Note, that all curves exhibit a dent at  $\bar{\phi} = 0.6$ . On the one hand, this highlights the correlations between the curves for different subsystem sizes. On the other hand, it could explain the incorrect order of the curve for  $\ell = 13.00$ .

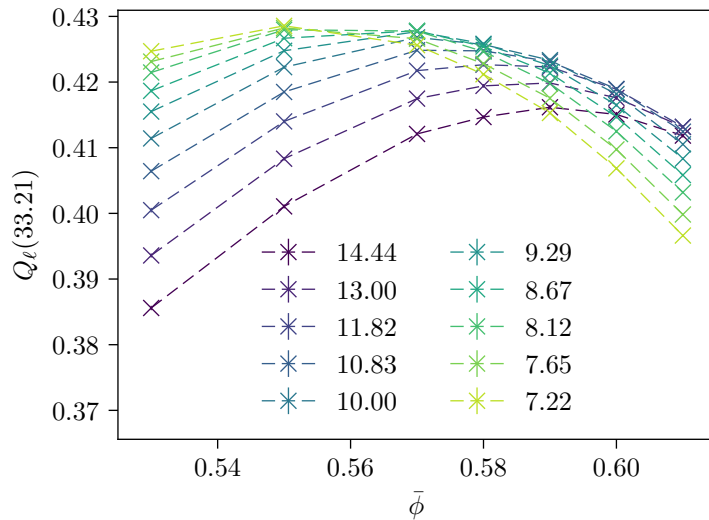


**Fig. A.3.:** Peak of  $Q_\ell$  at  $Pe \approx 33.21$  vs. the average packing fraction  $\bar{\phi}$  (Adapted from Figure S4a) of the SI to Reference [120], reprinted figure with permission from [J. T. Siebert et al., Physical Review E, 93, 030601(R), 2018] Copyright 2018 by the American Physical Society.): Plot analogous to Figure A.1 for  $Pe \approx 33.21$ . At this propulsion strength, the maxima become broader. The curves all show an order corresponding to the homogeneous region (going from large  $Q_\ell$  for small  $\ell$  towards smaller values for larger subsystems).

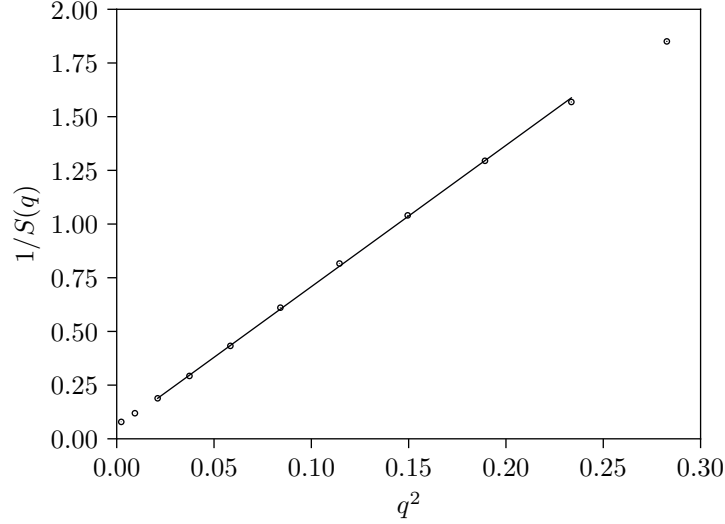


**Fig. A.4.:** Linear fit to  $1/S(q)$  vs.  $q^2$  for small  $q$  and for  $Pe \approx 33.2$  (Adapted from Figure S6a) of the SI to Reference [120], reprinted figure with permission from [J. T. Siebert et al., *Physical Review E*, 93, 030601(R), 2018] Copyright 2018 by the American Physical Society.): Choosing this lowest  $Pe$  available should minimize finite-size effects. To the same effect, the smallest  $q$  values are exempted from the fitting procedure. Assuming standard Ornstein-Zernicke form (see Eq. (A.1)), this fit allows to extract the correlation length  $\xi$ .

## A.2 Static structure factor and correlation length

In principle, the correlation length can be extracted by studying the low- $q$  limit of the static structure factor in the homogeneous region but close to criticality (see Eq. (8.3)). However, as explained in Section 8.5.2, this equation is only valid in the regime where  $\frac{2\pi}{L} \ll q \ll \frac{2\pi}{D}$  for box size  $L$  and typical particle distance  $D$ . Direct fitting of the structure factor's low- $q$  limit did not prove successful, as it resulted in a negative and thus unphysical estimate for the anomalous dimension, which can be attributed to the fact that the appropriate regime for  $q$  is not reached, at least very close to the critical point, where finite-size effects are maximal. Instead, we try here to extract the correlation length  $\xi$  at least for propulsion strengths significantly in the homogeneous region. This should minimize finite-size effects and thus allow us to find at least a very rough estimate for the correlation length for these parameters. To that end, we neglect the anomalous dimension  $\eta$  and assume standard Ornstein-Zernicke form [52]:

$$1/S(q) = 1/S(0) \cdot (1 + (\xi q)^2). \quad (\text{A.1})$$

Consequently, we can find an estimate for the correlation length by fitting  $1/S(q)$  for low  $q$ . To avoid finite size effects, the lowest  $q$  values are excluded from the fit though. Figure A.4 shows  $1/S(q)$  versus  $q^2$  for  $Pe \approx 33.2$ . At low  $q$ , there is an

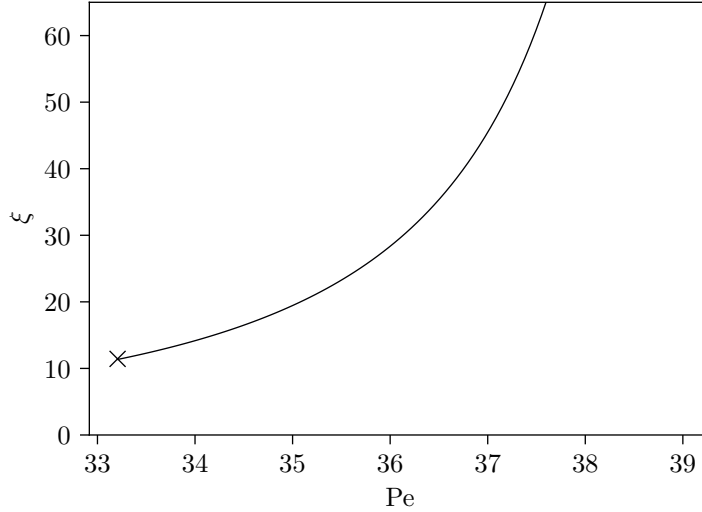


**Fig. A.5.:** Rough extrapolation of the correlation length approaching the critical point from the homogeneous region (Adapted from Figure S6b) of the SI to Reference [120], reprinted figure with permission from [J. T. Siebert et al., *Physical Review E*, 93, 030601(R), 2018] Copyright 2018 by the American Physical Society.): This estimation is based on the critical amplitude  $\xi_0$  and our best estimates for  $Pe_{cr}$  and  $\nu$ . As all of these are subject to statistical and potentially also systematic uncertainties, this extrapolation based on the scaling law in Eq. (A.2) can only serve as a qualitative estimate.

interval of roughly linear increase. Eq. (A.1) is then fitted to this region and the resulting fit, which is shown as a solid line in Figure A.4, seems to reproduce the data sufficiently well. The correlation length  $\xi \approx 11$  is found from the fitting parameters. Obviously, the procedure is only a rough approximation, as both the lower and upper  $q$  limits are found empirically and finite-size effects cannot be fully ruled out.

Regardless, taking our estimate for  $\xi$  we can try to approximate the course of the correlation length below the critical point:

$$\xi = \frac{\xi_0}{\left( Pe^{-1}/Pe_{cr}^{-1} - 1 \right)^\nu}. \quad (\text{A.2})$$

Inserting our best estimates  $Pe_{cr} \approx 40$  and  $\nu \approx 1.5$  gives a plausible estimate of  $\xi_0 \approx 1.0$ . If we assume this value, Eq. (A.2) gives a prediction for the evolution of the correlation length approaching the critical point from below. Figure A.5 shows this prediction. Keep in mind though, that all three quantities that were inserted in Eq. (A.2) have large associated uncertainties as well as possibly systematic biases. These results can thus only serve as rough, qualitative estimates of the true evolution.

The correlation length above the critical point could in principle be estimated similarly by studying the structure factor at points on the binodal lines. Given the very limited success of the procedure below the critical point, such an estimation is not carried out though. The large computational effort that would be necessary does not seem warranted.





# Bibliography

- [1] M. P. Allen and D. J. Tildesley. *Computer simulation of liquids*. Oxford university press, 1987 (cit. on p. 7).
- [2] L. Alvarez, L. Dai, B. M. Friedrich, et al. „The rate of change in Ca<sup>2+</sup> concentration controls sperm chemotaxis“. In: *The Journal of Cell Biology* 196.5 (2012), 653–663. DOI: 10.1083/jcb.201106096 (cit. on p. 2).
- [3] L. Bai and D. Breen. „Calculating Center of Mass in an Unbounded 2D Environment“. In: *Journal of Graphics, GPU, and Game Tools* 13.4 (2008), pp. 53–60. DOI: 10.1080/2151237X.2008.10129266 (cit. on p. 33).
- [4] M. Ballerini, N. Cabibbo, R. Candelier, et al. „Interaction ruling animal collective behavior depends on topological rather than metric distance: Evidence from a field study“. In: *Proceedings of the national academy of sciences* 105.4 (2008), pp. 1232–1237. DOI: 10.1073/pnas.0711437105 (cit. on p. 2).
- [5] J. A. Barker and D. Henderson. „Perturbation Theory and Equation of State for Fluids. II. A Successful Theory of Liquids“. In: *The Journal of Chemical Physics* 47.11 (1967), pp. 4714–4721. DOI: <http://dx.doi.org/10.1063/1.1701689> (cit. on p. 27).
- [6] U. Basu, V. Volpati, S. Caracciolo, and A. Gambassi. „Short-Time Behavior and Criticality of Driven Lattice Gases“. In: *Physical review letters* 118.5 (2017), p. 050602. DOI: 10.1103/PhysRevLett.118.050602 (cit. on p. 5).
- [7] C. Bechinger, R. Di Leonardo, H. Löwen, et al. „Active particles in complex and crowded environments“. In: *Reviews of Modern Physics* 88.4 (2016), p. 045006. DOI: 10.1103/RevModPhys.88.045006 (cit. on p. 2).
- [8] J. Bialké, T. Speck, and H. Löwen. „Active colloidal suspensions: Clustering and phase behavior“. In: *Journal of Non-Crystalline Solids* 407.0 (2015), pp. 367–375. DOI: 10.1016/j.jnoncrysol.2014.08.011 (cit. on p. 31).
- [9] J. Bialké, T. Speck, and H. Löwen. „Crystallization in a Dense Suspension of Self-Propelled Particles“. In: *Physical Review Letters* 108 (16 2012), p. 168301. DOI: 10.1103/PhysRevLett.108.168301 (cit. on pp. 2, 3, 26).
- [10] J. Bialké, H. Löwen, and T. Speck. „Microscopic theory for the phase separation of self-propelled repulsive disks“. In: *EPL (Europhysics Letters)* 103.3 (2013), p. 30008. DOI: 10.1209/0295-5075/103/30008 (cit. on p. 4).

- [11] J. Bialké, J. T. Siebert, H. Löwen, and T. Speck. „Negative Interfacial Tension in Phase-Separated Active Brownian Particles“. In: *Physical Review Letters* 115 (9 2015), p. 098301. DOI: 10.1103/PhysRevLett.115.098301 (cit. on pp. vii, 4, 21, 26, 31, 35, 37, 40, 41, 43, 44).
- [12] K. Binder. „Finite size effects on phase transitions“. In: *Ferroelectrics* 73.1 (1987), pp. 43–67. DOI: 10.1080/00150198708227908 (cit. on p. 56).
- [13] K. Binder. „Finite size scaling analysis of ising model block distribution functions“. English. In: *Zeitschrift für Physik B Condensed Matter* 43.2 (1981), pp. 119–140. DOI: 10.1007/BF01293604 (cit. on pp. 16, 17, 55, 56, 58, 70, 74, 75, 96, 97).
- [14] K. Binder, B. J. Block, P. Virnau, and A. Tröster. „Beyond the Van Der Waals loop: What can be learned from simulating Lennard-Jones fluids inside the region of phase coexistence“. In: *American Journal of Physics* 80.12 (2012), p. 1099. DOI: 10.1119/1.4754020 (cit. on p. 31).
- [15] J. Blaschke, M. Maurer, K. Menon, A. Zöttl, and H. Stark. „Phase separation and coexistence of hydrodynamically interacting microswimmers“. In: *Soft matter* 12.48 (2016), pp. 9821–9831. DOI: 10.1039/c6sm02042a (cit. on p. 4).
- [16] A. C. Brańka and D. M. Heyes. „Algorithms for Brownian dynamics computer simulations: Multivariable case“. In: *Phys. Rev. E* 60 (2 1999), pp. 2381–2387. DOI: 10.1103/PhysRevE.60.2381 (cit. on p. 28).
- [17] A. C. Brańka and D. M. Heyes. „Algorithms for Brownian dynamics simulation“. In: *Phys. Rev. E* 58 (2 1998), pp. 2611–2615. DOI: 10.1103/PhysRevE.58.2611 (cit. on p. 28).
- [18] A. Bruce and N. Wilding. „Scaling fields and universality of the liquid-gas critical point“. In: *Physical review letters* 68.2 (1992), p. 193. DOI: 10.1103/PhysRevLett.68.193 (cit. on pp. 15, 55, 60, 74, 77).
- [19] I. Buttinoni, G. Volpe, F. Kümmel, G. Volpe, and C. Bechinger. „Active Brownian motion tunable by light“. In: *Journal of Physics: Condensed Matter* 24.28 (2012), p. 284129. DOI: 10.1088/0953-8984/24/28/284129 (cit. on pp. 2, 4).
- [20] I. Buttinoni, J. Bialké, F. Kümmel, et al. „Dynamical Clustering and Phase Separation in Suspensions of Self-Propelled Colloidal Particles“. In: *Physical Review Letters* 110 (23 2013), p. 238301. DOI: 10.1103/PhysRevLett.110.238301 (cit. on pp. 2–4, 23, 24, 26).
- [21] X. Campi, H. Krivine, and N. Sator. „Percolation line of self-bound clusters in supercritical fluids“. In: *Physica A: Statistical Mechanics and its Applications* 296.1-2 (2001), pp. 24–30. DOI: 10.1016/S0378-4371(01)00158-3 (cit. on pp. 86, 87).
- [22] M. E. Cates and J. Tailleur. „When are active Brownian particles and run-and-tumble particles equivalent? Consequences for motility-induced phase separation“. In: *EPL (Europhysics Letters)* 101.2 (2013), p. 20010. DOI: 10.1209/0295-5075/101/20010 (cit. on pp. 3, 25, 26).
- [23] A. Coniglio and W. Klein. „Clusters and Ising critical droplets: a renormalisation group approach“. In: *Journal of Physics A: Mathematical and General* 13.8 (1980), p. 2775. DOI: 10.1088/0305-4470/13/8/025 (cit. on p. 87).

- [24]A. Cornfeld and H. Carr. „Experimental evidence concerning the law of rectilinear diameter“. In: *Physical Review Letters* 29.1 (1972), p. 28. DOI: 10.1103/PhysRevLett.29.28 (cit. on p. 36).
- [25]L. F. Cugliandolo, G. Gonnella, and A. Suma. „Fluctuations of rotational and translational degrees of freedom in an interacting active dumbbell system“. In: *Chaos, Solitons & Fractals* 81, Part B (2015), pp. 556–566. DOI: 10.1016/j.chaos.2015.04.015 (cit. on pp. 4, 45).
- [26]L. F. Cugliandolo, G. Gonnella, and A. Suma. „Rotational and translational diffusion in an interacting active dumbbell system“. In: *Phys. Rev. E* 91 (6 2015), p. 062124. DOI: 10.1103/PhysRevE.91.062124 (cit. on p. 45).
- [27]S. K. Das, S. A. Egorov, B. Trefz, P. Virnau, and K. Binder. „Phase Behavior of Active Swimmers in Depletants: Molecular Dynamics and Integral Equation Theory“. In: *Physical Review Letters* 112 (19 2014), p. 198301. DOI: 10.1103/PhysRevLett.112.198301 (cit. on p. 2).
- [28]F. Dittrich. Diploma Thesis, Johannes Gutenberg-Universität Mainz, Germany. 2017 (cit. on pp. 73–77, 82).
- [29]C. Dombrowski, L. Cisneros, S. Chatkaew, R. E. Goldstein, and J. O. Kessler. „Self-Concentration and Large-Scale Coherence in Bacterial Dynamics“. In: *Physical Review Letters* 93.9 (2004), p. 098103. DOI: 10.1103/physrevlett.93.098103 (cit. on p. 2).
- [30]R. Dreyfus, J. Baudry, M. L. Roper, et al. „Microscopic artificial swimmers“. In: *Nature* 437.7060 (2005), 862–865. DOI: 10.1038/nature04090 (cit. on p. 2).
- [31]Y. Duda, A. Romero-Martínez, and P. Orea. „Phase diagram and surface tension of the hard-core attractive Yukawa model of variable range: Monte Carlo simulations“. In: *The Journal of chemical physics* 126.22 (2007), p. 224510. DOI: 10.1063/1.2743623 (cit. on p. 44).
- [32]A. Einstein. „Autobiographical notes“. In: *Albert Einstein: philosopher-scientist* 1 (1949), pp. 1–94 (cit. on p. 1).
- [33]T. Eisenstecken, G. Gompper, and R. G. Winkler. „Conformational properties of active semiflexible polymers“. In: *Polymers* 8.8 (2016), p. 304. DOI: 10.3390/polym8080304 (cit. on pp. 4, 45).
- [34]S. El-Showk, M. F. Paulos, D. Poland, et al. „Solving the 3D Ising model with the conformal bootstrap II. c-minimization and precise critical exponents“. In: *Journal of Statistical Physics* 157.4-5 (2014), pp. 869–914. DOI: 10.1007/s10955-014-1042-7 (cit. on p. 15).
- [35]D. L. Ermak. „A computer simulation of charged particles in solution. I. Technique and equilibrium properties“. In: *The Journal of Chemical Physics* 62.10 (1975), pp. 4189–4196. DOI: 10.1063/1.430300 (cit. on p. 10).
- [36]J. W. Essam and M. E. Fisher. „Padé approximant studies of the lattice gas and Ising ferromagnet below the critical point“. In: *The Journal of Chemical Physics* 38.4 (1963), pp. 802–812. DOI: 10.1063/1.1733766 (cit. on p. 16).
- [37]L. Fejes. „Über die dichteste Kugellagerung“. In: *Mathematische Zeitschrift* 48.1 (Dec. 1, 1942), p. 676. DOI: 10.1007/BF01180035 (cit. on pp. 35, 53).

- [38]A. M. Ferrenberg and D. P. Landau. „Critical behavior of the three-dimensional Ising model: A high-resolution Monte Carlo study“. In: *Phys. Rev. B* 44 (10 1991), pp. 5081–5091. DOI: 10.1103/PhysRevB.44.5081 (cit. on p. 83).
- [39]A. M. Ferrenberg and R. H. Swendsen. „New Monte Carlo technique for studying phase transitions“. In: *Physical review letters* 61.23 (1988), p. 2635. DOI: 10.1103/PhysRevLett.61.2635 (cit. on p. 77).
- [40]A. M. Ferrenberg and R. H. Swendsen. „New Monte Carlo technique for studying phase transitions“. In: *Physical Review Letters* 63.15 (1989), p. 1658. DOI: 10.1103/PhysRevLett.63.1658.2 (cit. on p. 77).
- [41]A. M. Ferrenberg, D. P. Landau, and K Binder. „Statistical and systematic errors in Monte Carlo sampling“. In: *Journal of statistical physics* 63.5 (1991), pp. 867–882. DOI: 10.1007/BF01029988 (cit. on p. 59).
- [42]Y. Fily and M. C. Marchetti. „Athermal Phase Separation of Self-Propelled Particles with No Alignment“. In: *Physical Review Letters* 108 (23 2012), p. 235702. DOI: 10.1103/PhysRevLett.108.235702 (cit. on pp. 3, 4, 21, 24, 26, 88).
- [43]Y. Fily, S. Henkes, and M. C. Marchetti. „Freezing and phase separation of self-propelled disks“. In: *Soft Matter* 10 (13 2014), pp. 2132–2140. DOI: 10.1039/C3SM52469H (cit. on pp. 31, 86).
- [44]M. E. Fisher. „The theory of critical point singularities“. In: *Critical Phenomena*. Ed. by M. S. Green. Academic Press, London, 1971 (cit. on p. 16).
- [45]M. E. Fisher. „Correlation functions and the critical region of simple fluids“. In: *Journal of Mathematical Physics* 5.7 (1964), pp. 944–962. DOI: 10.1063/1.1704197 (cit. on pp. 13, 88).
- [46]M. E. Fisher. „Rigorous inequalities for critical-point correlation exponents“. In: *Physical Review* 180.2 (1969), p. 594. DOI: 10.1103/PhysRev.180.594 (cit. on p. 15).
- [47]M. E. Fisher and M. N. Barber. „Scaling theory for finite-size effects in the critical region“. In: *Physical Review Letters* 28.23 (1972), p. 1516. DOI: 10.1103/PhysRevLett.28.1516 (cit. on p. 16).
- [48]A. Furukawa, D. Marenduzzo, and M. E. Cates. „Activity-induced clustering in model dumbbell swimmers: The role of hydrodynamic interactions“. In: *Physical Review E* 90.2 (2014), p. 022303. DOI: 10.1103/physreve.90.022303 (cit. on pp. 4, 45).
- [49]F. Ginot, I. Theurkauff, D. Levis, et al. „Nonequilibrium Equation of State in Suspensions of Active Colloids“. In: *Phys. Rev. X* 5 (1 2015), p. 011004. DOI: 10.1103/PhysRevX.5.011004 (cit. on pp. 5, 37, 42–44).
- [50]S. Goldman. „An explicit equation for the radial distribution function of a dense Lennard-Jones fluid“. In: *Journal of Physical Chemistry* 83.23 (1979), pp. 3033–3037. DOI: 10.1021/j100486a020 (cit. on p. 90).
- [51]T. C. Hales. „A proof of the Kepler conjecture“. In: *Annals of mathematics* 162.3 (2005), pp. 1065–1185. DOI: 10.4007/annals.2005.162.1065 (cit. on p. 53).
- [52]J.-P. Hansen and I. R. McDonald. *Theory of simple liquids*. Elsevier, 1990 (cit. on pp. 88, 105).

- [53] M. Hasenbusch. „Finite size scaling study of lattice models in the three-dimensional Ising universality class“. In: *Physical Review B* 82.17 (2010), p. 174433. DOI: 10.1103/PhysRevB.82.174433 (cit. on p. 15).
- [54] S. Herminghaus, C. C. Maass, C. Krüger, et al. „Interfacial mechanisms in active emulsions“. In: *Soft Matter* 10.36 (2014), 7008–7022. DOI: 10.1039/c4sm00550c (cit. on p. 2).
- [55] Y. Hong, N. M. K. Blackman, N. D. Kopp, A. Sen, and D. Velegol. „Chemotaxis of Nonbiological Colloidal Rods“. In: *Phys. Rev. Lett.* 99 (17 2007), p. 178103. DOI: 10.1103/PhysRevLett.99.178103 (cit. on p. 2).
- [56] J. R. Howse, R. A. L. Jones, A. J. Ryan, et al. „Self-Motile Colloidal Particles: From Directed Propulsion to Random Walk“. In: *Physical Review Letters* 99 (4 2007), p. 048102. DOI: 10.1103/PhysRevLett.99.048102 (cit. on p. 22).
- [57] J. D. Hunter. „Matplotlib: A 2D graphics environment“. In: *Computing in science & engineering* 9.3 (2007), pp. 90–95. DOI: 10.1109/MCSE.2007.55 (cit. on p. 20).
- [58] Y. Imry and D. Bergman. „Critical points and scaling laws for finite systems“. In: *Physical Review A* 3.4 (1971), p. 1416. DOI: 10.1103/PhysRevA.3.1416 (cit. on p. 16).
- [59] H.-R. Jiang, N. Yoshinaga, and M. Sano. „Active Motion of a Janus Particle by Self-Thermophoresis in a Defocused Laser Beam“. In: *Physical Review Letters* 105.26 (2010), pp. –. DOI: 10.1103/physrevlett.105.268302 (cit. on p. 2).
- [60] E. Jones, T. Oliphant, P. Peterson, et al. *SciPy: Open source scientific tools for Python*. [Online; accessed 17.05.2018]. 2001– (cit. on p. 20).
- [61] R. Jones and F. Alavi. „Rotational diffusion of a tracer colloid particle: IV. Brownian dynamics with wall effects“. In: *Physica A: Statistical Mechanics and its Applications* 187.3–4 (1992), pp. 436–455. DOI: 10.1016/0378-4371(92)90004-A (cit. on pp. 9, 10).
- [62] S. Jünger, B. Knuth, and F. Hensel. „Observation of singular diameters in the coexistence curves of metals“. In: *Physical review letters* 55.20 (1985), p. 2160. DOI: 10.1103/PhysRevLett.55.2160 (cit. on p. 85).
- [63] L. P. Kadanoff, W. Götze, D. Hamblen, et al. „Static phenomena near critical points: theory and experiment“. In: *Reviews of Modern Physics* 39.2 (1967), p. 395. DOI: 10.1103/RevModPhys.39.395 (cit. on p. 13).
- [64] A. Kaiser, S. Babel, B. ten Hagen, C. von Ferber, and H. Löwen. „How does a flexible chain of active particles swell?“ In: *The Journal of Chemical Physics* 142.12, 124905 (2015), pp. –. DOI: 10.1063/1.4916134 (cit. on pp. 4, 45).
- [65] Y. Katz, K. Tunstrøm, C. C. Ioannou, C. Huepe, and I. D. Couzin. „Inferring the structure and dynamics of interactions in schooling fish“. In: *Proceedings of the National Academy of Sciences* 108.46 (2011), pp. 18720–18725. DOI: 10.1073/pnas.1107583108 (cit. on p. 2).
- [66] Y. C. Kim and M. E. Fisher. „Asymmetric fluid criticality. II. Finite-size scaling for simulations“. In: *Phys. Rev. E* 68 (4 2003), p. 041506. DOI: 10.1103/PhysRevE.68.041506 (cit. on pp. 36, 60, 61, 64, 65, 77, 84).

- [67]Y. C. Kim, M. E. Fisher, and G. Orkoulas. „Asymmetric fluid criticality. I. Scaling with pressure mixing“. In: *Phys. Rev. E* 67 (6 2003), p. 061506. DOI: 10.1103/PhysRevE.67.061506 (cit. on pp. 64, 65, 77).
- [68]Y. C. Kim, M. E. Fisher, and E. Luijten. „Precise Simulation of Near-Critical Fluid Coexistence“. In: *Physical Review Letters* 91 (6 2003), p. 065701. DOI: 10.1103/PhysRevLett.91.065701 (cit. on pp. 55, 64, 65, 77).
- [69]J. G. Kirkwood and F. P. Buff. „The statistical mechanical theory of surface tension“. In: *The Journal of Chemical Physics* 17.3 (1949), pp. 338–343. DOI: 10.1063/1.1747248 (cit. on p. 43).
- [70]K. Kiyohara, K. E. Gubbins, and A. Z. Panagiotopoulos. „Phase coexistence properties of polarizable Stockmayer fluids“. In: *The Journal of chemical physics* 106.8 (1997), pp. 3338–3347. DOI: 10.1063/1.473082 (cit. on p. 77).
- [71]P. Kloeden and E. Platen. *Numerical Solution of Stochastic Differential Equations*. 3rd ed. Stochastic Modelling and Applied Probability. Springer Berlin Heidelberg, 1999 (cit. on p. 28).
- [72]G. H. Koenderink, Z. Dogic, F. Nakamura, et al. „An active biopolymer network controlled by molecular motors“. In: *Proceedings of the National Academy of Sciences* 106.36 (2009), pp. 15192–15197. DOI: 10.1073/pnas.0903974106 (cit. on p. 1).
- [73]F. Kos, D. Poland, D. Simmons-Duffin, and A. Vichi. „Precision islands in the Ising and O(N) models“. In: *Journal of High Energy Physics* 2016.8 (2016), p. 36. DOI: 10.1007/jhep08(2016)036 (cit. on p. 15).
- [74]D. P. Landau and K. Binder. *A guide to Monte Carlo simulations in statistical physics*. Cambridge university press, 2014 (cit. on pp. 7, 16, 98, 99).
- [75]L. D. Landau. „On the theory of phase transitions. I.“ In: *Zh. Eksp. Teor. Fiz.* 11 (1937), p. 19 (cit. on p. 15).
- [76]T. W. Lion and R. J. Allen. „Osmosis with active solutes“. In: *EPL (Europhysics Letters)* 106.3 (2014), p. 34003. DOI: 10.1209/0295-5075/106/34003 (cit. on pp. 5, 37).
- [77]E. Luijten, M. E. Fisher, and A. Z. Panagiotopoulos. „Universality Class of Criticality in the Restricted Primitive Model Electrolyte“. In: *Physical Review Letters* 88 (18 2002), p. 185701. DOI: 10.1103/PhysRevLett.88.185701 (cit. on pp. 15, 64, 65, 77, 93).
- [78]F. Léonard and B. Delamotte. „Critical Exponents Can Be Different on the Two Sides of a Transition: A Generic Mechanism.“ In: *Physical review letters* 115 (20 Nov. 2015), p. 200601. DOI: 10.1103/PhysRevLett.115.200601 (cit. on p. 15).
- [79]H. Löwen. „Active Colloidal Molecules“. Preprint available at <https://arxiv.org/abs/1803.09642>. Mar. 26, 2018 (cit. on p. 4).
- [80]L. G. MacDowell, P. Virnau, M. Müller, and K. Binder. „The evaporation/condensation transition of liquid droplets“. In: *J. Chem. Phys.* 120.11 (2004), p. 5293. DOI: 10.1063/1.1645784 (cit. on p. 31).
- [81]N. de Macedo Biniossek, H. Löwen, T. Voigtmann, and F. Smallenburg. „Static structure of active Brownian hard disks“. In: *Journal of Physics: Condensed Matter* 30.7 (2018), p. 074001. DOI: 10.1088/1361-648X/aaa3bf (cit. on p. 88).

- [82]V. Magdanz, S. Sanchez, and O. G. Schmidt. „Development of a Sperm-Flagella Driven Micro-Bio-Robot“. In: *Advanced Materials* 25.45 (2013), 6581–6588. DOI: 10.1002/adma.201302544 (cit. on p. 2).
- [83]S. Mallory, A Šarić, C Valeriani, and A Cacciuto. „Anomalous thermomechanical properties of a self-propelled colloidal fluid“. In: *Physical Review E* 89.5 (2014), p. 052303. DOI: 10.1103/PhysRevE.89.052303 (cit. on pp. 5, 37).
- [84]N. March. „Similarities and contrasts between critical point behavior of heavy fluid alkalis and d-dimensional Ising model“. In: *Physics Letters A* 378.3 (2014), pp. 254–256. DOI: 10.1016/j.physleta.2013.10.030 (cit. on p. 85).
- [85]M. C. Marchetti, J.-F. Joanny, S. Ramaswamy, et al. „Hydrodynamics of soft active matter“. In: *Reviews of Modern Physics* 85.3 (2013), p. 1143. DOI: 10.1103/RevModPhys.85.1143 (cit. on pp. 4, 39).
- [86]B McCoy. *Advanced Statistical Mechanics (International Series of Monographs on Physics 146)*. Oxford: Oxford University Press, 2010 (cit. on pp. 7, 15, 16).
- [87]W. McKinney. „Data Structures for Statistical Computing in Python“. In: *Proceedings of the 9th Python in Science Conference*. Ed. by S. van der Walt and J. Millman. 2010, pp. 51–56 (cit. on p. 20).
- [88]A. Morsali, E. K. Goharshadi, G. A. Mansoori, and M. Abbaspour. „An accurate expression for radial distribution function of the Lennard-Jones fluid“. In: *Chemical physics* 310.1-3 (2005), pp. 11–15. DOI: 10.1016/j.chemphys.2004.09.027 (cit. on pp. 90, 91).
- [89]V. Narayan, S. Ramaswamy, and N. Menon. „Long-Lived Giant Number Fluctuations in a Swarming Granular Nematic“. In: *Science* 317.5834 (2007), 105–108. DOI: 10.1126/science.1140414 (cit. on p. 2).
- [90]D. R. Nelson. „Coexistence-curve singularities in isotropic ferromagnets“. In: *Physical Review B* 13.5 (1976), p. 2222. DOI: 10.1103/PhysRevB.13.2222 (cit. on p. 15).
- [91]R. Ni, M. A. C. Stuart, and P. G. Bolhuis. „Tunable long range forces mediated by self-propelled colloidal hard spheres“. In: *Physical review letters* 114.1 (2015), p. 018302. DOI: 10.1103/PhysRevLett.114.018302 (cit. on pp. 5, 37).
- [92]L. Onsager. „Crystal statistics. I. A two-dimensional model with an order-disorder transition“. In: *Physical Review* 65.3-4 (1944), p. 117. DOI: 10.1103/PhysRev.65.117 (cit. on pp. 15, 75, 76).
- [93]G. Orkoulas, M. E. Fisher, and A. Z. Panagiotopoulos. „Precise simulation of criticality in asymmetric fluids“. In: *Phys. Rev. E* 63 (5 2001), p. 051507. DOI: 10.1103/PhysRevE.63.051507 (cit. on pp. 15, 64, 65, 67, 77).
- [94]J. Palacci, S. Sacanna, A. P. Steinberg, D. J. Pine, and P. M. Chaikin. „Living Crystals of Light-Activated Colloidal Surfers“. In: *Science* 339.6122 (2013), pp. 936–940. DOI: 10.1126/science.1230020 (cit. on pp. 4, 26).
- [95]J. Palacci, C. Cottin-Bizonne, C. Ybert, and L. Bocquet. „Sedimentation and Effective Temperature of Active Colloidal Suspensions“. In: *Phys. Rev. Lett.* 105 (8 2010), p. 088304. DOI: 10.1103/PhysRevLett.105.088304 (cit. on p. 2).

- [96]A. Panagiotopoulos. „Molecular simulation of phase coexistence: Finite-size effects and determination of critical parameters for two-and three-dimensional Lennard-Jones fluids“. In: *International journal of thermophysics* 15.6 (1994), pp. 1057–1072. DOI: 10.1007/BF01458815 (cit. on p. 77).
- [97]W. F. Paxton, K. C. Kistler, C. C. Olmeda, et al. „Catalytic nanomotors: autonomous movement of striped nanorods“. In: *Journal of the American Chemical Society* 126.41 (2004), pp. 13424–13431. DOI: 10.1021/ja047697z (cit. on p. 2).
- [98]K. Peddireddy, P. Kumar, S. Thutupalli, S. Herminghaus, and C. Bahr. „Solubilization of Thermotropic Liquid Crystal Compounds in Aqueous Surfactant Solutions“. In: *Langmuir* 28.34 (2012), 12426–12431. DOI: 10.1021/la3015817 (cit. on p. 2).
- [99]Persistence of Vision Pty. Ltd. (2004). *Persistence of Vision Raytracer (Version 3.6)*. <http://www.povray.org/> (cit. on p. 20).
- [100]F. Peruani, A. Deutsch, and M. Bär. „Nonequilibrium clustering of self-propelled rods“. In: *Physical Review E* 74.3 (2006), p. 030904. DOI: 10.1103/physreve.74.030904 (cit. on p. 45).
- [101]V. Prymidis, S. Paliwal, M. Dijkstra, and L. Filion. „Vapour-liquid coexistence of an active Lennard-Jones fluid“. In: *The Journal of Chemical Physics* 145.12 (2016), p. 124904. DOI: 10.1063/1.4963191 (cit. on pp. 5, 6, 35, 36, 85).
- [102]S. Ramaswamy, R. A. Simha, and J. Toner. „Active nematics on a substrate: Giant number fluctuations and long-time tails“. In: *Europhysics Letters* 62.2 (2003), 196–202. DOI: 10.1209/ep1/i2003-00346-7 (cit. on p. 2).
- [103]G. S. Redner, C. G. Wagner, A. Baskaran, and M. F. Hagan. „Classical Nucleation Theory Description of Active Colloid Assembly“. In: *Physical review letters* 117.14 (2016), p. 148002. DOI: 10.1103/PhysRevLett.117.148002 (cit. on p. 25).
- [104]G. S. Redner, M. F. Hagan, and A. Baskaran. „Structure and Dynamics of a Phase-Separating Active Colloidal Fluid“. In: *Physical Review Letters* 110 (5 2013), p. 055701. DOI: 10.1103/PhysRevLett.110.055701 (cit. on pp. 3, 4, 21, 25, 26, 31, 53).
- [105]S. Reif-Acherman. „The history of the rectilinear diameter law“. en. In: *Química Nova* 33 (2010), pp. 2003–2010. DOI: 10.1590/S0100-40422010000900033 (cit. on p. 36).
- [106]A. Reinmüller, H. J. Schöpe, and T. Palberg. „Self-organized cooperative swimming at low Reynolds numbers“. In: *Langmuir* 29.6 (2013), pp. 1738–1742. DOI: 10.1021/la3046466 (cit. on pp. 2, 4).
- [107]D. Richard, H. Löwen, and T. Speck. „Nucleation pathway and kinetics of phase-separating active Brownian particles“. In: *Soft Matter* 12.24 (2016), 5257–5264. DOI: 10.1039/c6sm00485g (cit. on p. 25).
- [108]M. Rovere, D. W. Hermann, and K. Binder. „Block Density Distribution Function Analysis of Two-Dimensional Lennard-Jones Fluids“. In: *EPL (Europhysics Letters)* 6.7 (1988), p. 585. DOI: 10.1209/0295-5075/6/7/003 (cit. on pp. 56, 63).
- [109]M. Rovere, P. Nielaba, and K. Binder. „Simulation studies of gas-liquid transitions in two dimensions via a subsystem-block-density distribution analysis“. In: *Z. Physik B - Condensed Matter* 90.2 (1993), pp. 215–228. DOI: 10.1007/bf02198158 (cit. on pp. 17, 55, 56, 58–60, 63, 64, 75–78).



- [110]M Rovere, D. W. Heermann, and K Binder. „The gas-liquid transition of the two-dimensional Lennard-Jones fluid“. In: *Journal of Physics: Condensed Matter* 2.33 (1990), p. 7009. DOI: 10.1088/0953-8984/2/33/013 (cit. on pp. 56, 63).
- [111]S. Roy, S. Dietrich, and F. Höfling. „Structure and dynamics of binary liquid mixtures near their continuous demixing transitions“. In: *The Journal of Chemical Physics* 145.13 (2016), p. 134505. DOI: 10.1063/1.4963771 (cit. on p. 55).
- [112]G. Rushbrooke. „On the thermodynamics of the critical region for the Ising problem“. In: *The Journal of Chemical Physics* 39.3 (1963), pp. 842–843. DOI: 10.1063/1.1734338 (cit. on pp. 15, 16).
- [113]T. Sanchez, D. T. N. Chen, S. J. DeCamp, M. Heymann, and Z. Dogic. „Spontaneous motion in hierarchically assembled active matter“. In: *Nature* 491.7424 (Nov. 2012), pp. 431–434. DOI: 10.1038/nature11591 (cit. on p. 1).
- [114]M. Santra, S. Chakrabarty, and B. Bagchi. „Gas-liquid nucleation in a two dimensional system“. In: *The Journal of chemical physics* 129.23 (2008), p. 234704. DOI: 10.1063/1.3037241 (cit. on p. 44).
- [115]V. Schaller, C. Weber, C. Semmrich, E. Frey, and A. R. Bausch. „Polar patterns of driven filaments“. In: *Nature* 467.7311 (Sept. 2010), pp. 73–77. DOI: 10.1038/nature09312 (cit. on p. 1).
- [116]M. Schrader, P. Virnau, and K. Binder. „Simulation of vapor-liquid coexistence in finite volumes: A method to compute the surface free energy of droplets“. In: *Phys. Rev. E* 79.6 (2009), p. 061104. DOI: 10.1103/physreve.79.061104 (cit. on p. 31).
- [117]F. Schwabl. *Statistische Physik*. 3rd ed. Springer-Verlag Berlin Heidelberg, 2006 (cit. on pp. 1, 7, 15).
- [118]U. Seifert. „Stochastic thermodynamics, fluctuation theorems and molecular machines“. In: *Reports on Progress in Physics* 75.12 (2012), p. 126001. DOI: 10.1088/0034-4885/75/12/126001 (cit. on p. 1).
- [119]W. Selke. „Critical Binder cumulant of two-dimensional Ising models“. English. In: *The European Physical Journal B - Condensed Matter and Complex Systems* 51.2 (2006), pp. 223–228. DOI: 10.1140/epjb/e2006-00209-7 (cit. on p. 93).
- [120]J. T. Siebert, F. Dittrich, F. Schmid, et al. „Critical behavior of active Brownian particles“. In: *Phys. Rev. E* 98 (3 2018), p. 030601. DOI: 10.1103/PhysRevE.98.030601 (cit. on pp. viii, 55, 73–75, 79, 83, 85, 89, 93–95, 97, 99, 104–106).
- [121]J. T. Siebert, J. Letz, T. Speck, and P. Virnau. „Phase behavior of active Brownian disks, spheres, and dimers“. In: *Soft Matter* 13.5 (2017), 1020–1026. DOI: 10.1039/c6sm02622b (cit. on pp. vii, 2, 4, 21, 26, 31, 33, 34, 45–47, 49, 52).
- [122]J. K. Singh, D. A. Kofke, and J. R. Errington. „Surface tension and vapor–liquid phase coexistence of the square-well fluid“. In: *The Journal of chemical physics* 119.6 (2003), pp. 3405–3412. DOI: 10.1063/1.1590313 (cit. on p. 44).
- [123]B Smit and D Frenkel. „Vapor–liquid equilibria of the two-dimensional Lennard-Jones fluid (s)“. In: *The Journal of chemical physics* 94.8 (1991), pp. 5663–5668. DOI: 10.1063/1.460477 (cit. on pp. 76, 77).

- [124]J. Smrek and K. Kremer. „Small activity differences drive phase separation in active-passive polymer mixtures“. In: *Physical review letters* 118.9 (2017), p. 098002. DOI: 10.1103/PhysRevLett.118.098002 (cit. on pp. 4, 45).
- [125]A. P. Solon, J. Stenhammar, R. Wittkowski, et al. „Pressure and Phase Equilibria in Interacting Active Brownian Spheres“. In: *Physical Review Letters* 114 (19 2015), p. 198301. DOI: 10.1103/PhysRevLett.114.198301 (cit. on pp. 3–5, 21, 26, 31, 37, 40, 42–44).
- [126]A. P. Solon, Y Fily, A. Baskaran, et al. „Pressure is not a state function for generic active fluids“. In: *Nature Physics* 11.8 (2015), pp. 673–678. DOI: 10.1038/nphys3377 (cit. on pp. 5, 37, 42–44).
- [127]R. Soto and R. Golestanian. „Run-and-tumble dynamics in a crowded environment: Persistent exclusion process for swimmers“. In: *Physical Review E* 89.1 (2014), p. 012706. DOI: 10.1103/PhysRevE.89.012706 (cit. on p. 3).
- [128]R. Soto and R. Golestanian. „Self-assembly of catalytically active colloidal molecules: tailoring activity through surface chemistry“. In: *Physical review letters* 112.6 (2014), p. 068301. DOI: 10.1103/PhysRevLett.112.068301 (cit. on p. 4).
- [129]T. Speck. „Stochastic thermodynamics for active matter“. In: *Europhys. Lett* 114 (2016), p. 30006. DOI: 10.1209/0295-5075/114/30006 (cit. on pp. 1, 5, 39).
- [130]T. Speck and R. L. Jack. „Ideal bulk pressure of active Brownian particles“. In: *Physical Review E* 93.6 (2016), p. 062605. DOI: 10.1103/physreve.93.062605 (cit. on pp. 37, 42).
- [131]T. Speck, A. M. Menzel, J. Bialké, and H. Löwen. „Dynamical mean-field theory and weakly non-linear analysis for the phase separation of active Brownian particles“. In: *The Journal of Chemical Physics* 142.22, 224109 (2015), pp. –. DOI: 10.1063/1.4922324 (cit. on pp. 5, 96).
- [132]A. Statt, R. Pinchaipat, F. Turci, R. Evans, and C. P. Royall. „Direct observation in 3d of structural crossover in binary hard sphere mixtures“. In: *The Journal of chemical physics* 144.14 (2016), p. 144506. DOI: 10.1063/1.4945808 (cit. on p. 91).
- [133]J. Stenhammar, A. Tiribocchi, R. J. Allen, D. Marenduzzo, and M. E. Cates. „Continuum Theory of Phase Separation Kinetics for Active Brownian Particles“. In: *Physical Review Letters* 111 (14 2013), p. 145702. DOI: 10.1103/PhysRevLett.111.145702 (cit. on pp. 5, 25, 26, 31, 53).
- [134]J. Stenhammar, D. Marenduzzo, R. J. Allen, and M. E. Cates. „Phase behaviour of active Brownian particles: the role of dimensionality“. In: *Soft Matter* 10 (10 2014), pp. 1489–1499. DOI: 10.1039/C3SM52813H (cit. on pp. 4, 9, 21, 26, 27, 31, 45, 52).
- [135]F. H. Stillinger Jr. „Rigorous Basis of the Frenkel-Band Theory of Association Equilibrium“. In: *The Journal of Chemical Physics* 38.7 (1963), pp. 1486–1494. DOI: 10.1063/1.1776907 (cit. on p. 86).
- [136]A. Suma, G. Gonnella, D. Marenduzzo, and E. Orlandini. „Motility-induced phase separation in an active dumbbell fluid“. In: *EPL (Europhysics Letters)* 108.5 (2014), p. 56004. DOI: 10.1209/0295-5075/108/56004 (cit. on pp. 4, 45).
- [137]J. Tailleur and M. E. Cates. „Statistical Mechanics of Interacting Run-and-Tumble Bacteria“. In: *Physical Review Letters* 100 (21 2008), p. 218103. DOI: 10.1103/PhysRevLett.100.218103 (cit. on pp. 3, 99, 102).

- [138]S. C. Takatori and J. F. Brady. „Towards a thermodynamics of active matter“. In: *Phys. Rev. E* 91 (3 2015), p. 032117. DOI: 10.1103/PhysRevE.91.032117 (cit. on pp. 5, 25, 26, 42).
- [139]S. C. Takatori, W. Yan, and J. F. Brady. „Swim Pressure: Stress Generation in Active Matter“. In: *Physical Review Letters* 113 (2 2014), p. 028103. DOI: 10.1103/PhysRevLett.113.028103 (cit. on pp. 5, 37, 39, 42–44, 101).
- [140]B ten Hagen, S van Teeffelen, and H Löwen. „Brownian motion of a self-propelled particle“. In: *Journal of Physics: Condensed Matter* 23.19 (2011), p. 194119. DOI: 10.1088/0953-8984/23/19/194119 (cit. on p. 21).
- [141]B. Trefz. „Computer simulations of the statistical behaviour of active particles“. Available at: [https://publications.uni-mainz.de/theses/frontdoor.php?source\\_opus=100000793](https://publications.uni-mainz.de/theses/frontdoor.php?source_opus=100000793). PhD thesis. Johannes Gutenberg-Universität Mainz, 2016 (cit. on pp. 5, 35, 36, 55, 56, 58, 59, 69, 85, 98).
- [142]B. Trefz, S. K. Das, S. A. Egorov, P. Virnau, and K. Binder. „Activity mediated phase separation: Can we understand phase behavior of the nonequilibrium problem from an equilibrium approach?“ In: *J. Chem. Phys.* 144.14 (2016), p. 144902. DOI: 10.1063/1.4945365 (cit. on pp. 2, 32).
- [143]B. Trefz, J. T. Siebert, T. Speck, K. Binder, and P. Virnau. „Estimation of the critical behavior in an active colloidal system with Vicsek-like interactions“. In: *The Journal of Chemical Physics* 146.7 (2017), p. 074901. DOI: 10.1063/1.4975812 (cit. on pp. vii, 5, 35, 36, 55, 56, 58, 59, 69, 80, 85, 98).
- [144]C. Tung, J. Harder, C. Valeriani, and A. Cacciuto. „Micro-phase separation in two dimensional suspensions of self-propelled spheres and dumbbells“. In: *Soft Matter* 12 (2 2016), pp. 555–561. DOI: 10.1039/C5SM02350E (cit. on p. 45).
- [145]T. Vicsek and A. Zafeiris. „Collective motion“. In: *Physics Reports* 517.3-4 (2012), pp. 71–140. DOI: 10.1016/j.physrep.2012.03.004 (cit. on p. 1).
- [146]T. Vicsek, A. Czirók, E. Ben-Jacob, I. Cohen, and O. Shochet. „Novel Type of Phase Transition in a System of Self-Driven Particles“. In: *Physical Review Letters* 75 (6 1995), pp. 1226–1229. DOI: 10.1103/PhysRevLett.75.1226 (cit. on p. 3).
- [147]R. L. C. Vink, K. Binder, and J. Horbach. „Critical behavior of a colloid-polymer mixture confined between walls“. In: *Phys. Rev. E* 73 (5 2006), p. 056118. DOI: 10.1103/PhysRevE.73.056118 (cit. on pp. 55, 61).
- [148]G. Volpe, I. Buttinoni, D. Vogt, H.-J. Kümmerer, and C. Bechinger. „Microswimmers in patterned environments“. In: *Soft Matter* 7.19 (2011), pp. 8810–8815. DOI: 10.1039/c1sm05960b (cit. on pp. 2–4).
- [149]S. v. d. Walt, S. C. Colbert, and G. Varoquaux. „The NumPy array: a structure for efficient numerical computation“. In: *Computing in Science & Engineering* 13.2 (2011), pp. 22–30. DOI: 10.1109/MCSE.2011.37 (cit. on p. 20).
- [150]J. Walton, D. Tildesley, J. Rowlinson, and J. Henderson. „The pressure tensor at the planar surface of a liquid“. In: *Molecular Physics* 48.6 (1983), pp. 1357–1368. DOI: 10.1080/00268978300100971 (cit. on pp. 38, 40).
- [151]W. Wang, L. A. Castro, M. Hoyos, and T. E. Mallouk. „Autonomous motion of metallic microrods propelled by ultrasound“. In: *ACS nano* 6.7 (2012), pp. 6122–6132. DOI: 10.1021/nm301312z (cit. on p. 2).

- [152]H. Watanabe, N. Ito, and C.-K. Hu. „Phase diagram and universality of the Lennard-Jones gas-liquid system“. In: *The Journal of Chemical Physics* 136.20, 204102 (2012), pp. –. DOI: 10.1063/1.4720089 (cit. on pp. 19, 32, 34, 36, 55, 58, 59, 64).
- [153]J. D. Weeks, D. Chandler, and H. C. Andersen. „Role of repulsive forces in determining the equilibrium structure of simple liquids“. In: *The Journal of chemical physics* 54.12 (1971), pp. 5237–5247. DOI: 10.1063/1.1674820 (cit. on pp. 26, 27).
- [154]F. J. Wegner. „Corrections to scaling laws“. In: *Physical Review B* 5.11 (1972), p. 4529. DOI: 10.1103/PhysRevB.5.4529 (cit. on p. 58).
- [155]J. Weiner, K. H. Langley, and N. Ford Jr. „Experimental evidence for a departure from the law of the rectilinear diameter“. In: *Physical Review Letters* 32.16 (1974), p. 879. DOI: 10.1103/PhysRevLett.32.879 (cit. on p. 36).
- [156]H. H. Wensink and H. Löwen. „Emergent states in dense systems of active rods: from swarming to turbulence“. In: *Journal of Physics: Condensed Matter* 24.46 (2012), p. 464130. DOI: 10.1088/0953-8984/24/46/464130 (cit. on pp. 2, 45).
- [157]S. Whitelam, K. Klymko, and D. Mandal. „Phase separation and large deviations of lattice active matter“. In: *The Journal of Chemical Physics* 148.15 (2018), p. 154902. DOI: 10.1063/1.5023403 (cit. on pp. 3, 99, 102).
- [158]B. Widom. „Equation of state in the neighborhood of the critical point“. In: *The Journal of Chemical Physics* 43.11 (1965), pp. 3898–3905. DOI: 10.1063/1.1696618 (cit. on p. 16).
- [159]N. Wilding and A. Bruce. „Density fluctuations and field mixing in the critical fluid“. In: *Journal of Physics: Condensed Matter* 4.12 (1992), p. 3087. DOI: 10.1088/0953-8984 (cit. on p. 77).
- [160]N. B. Wilding. „Critical-point and coexistence-curve properties of the Lennard-Jones fluid: a finite-size scaling study“. In: *Physical Review E* 52.1 (1995), p. 602. DOI: 10.1103/PhysRevE.52.602 (cit. on pp. 15, 55, 58, 70, 77).
- [161]N. B. Wilding. „Simulation studies of fluid critical behaviour“. In: *Journal of Physics: Condensed Matter* 9.3 (1997), p. 585. DOI: 10.1088/0953-8984/9/3/002 (cit. on p. 55).
- [162]N. B. Wilding and M. Müller. „Liquid–vapor asymmetry in pure fluids: A Monte Carlo simulation study“. In: *The Journal of chemical physics* 102.6 (1995), pp. 2562–2573. DOI: 10.1063/1.468686 (cit. on p. 55).
- [163]R. G. Winkler, A. Wysocki, and G. Gompper. „Virial pressure in systems of spherical active Brownian particles“. In: *Soft Matter* 11 (33 2015), pp. 6680–6691. DOI: 10.1039/C5SM01412C (cit. on pp. 5, 37).
- [164]D. Winter, P. Virnau, J. Horbach, and K. Binder. „Finite-size scaling analysis of the anisotropic critical behavior of the two-dimensional Ising model under shear“. In: *EPL (Europhysics Letters)* 91.6 (2010), p. 60002. DOI: 10.1209/0295-5075/91/60002 (cit. on p. 5).
- [165]D. Winter, P. Virnau, and K. Binder. „Heterogeneous nucleation at a wall near a wetting transition: a Monte Carlo test of the classical theory“. In: *Journal of Physics: Condensed Matter* 21.46 (2009), p. 464118. DOI: 10.1088/0953-8984/21/46/464118 (cit. on p. 31).

- [166]R. Wittkowski, A. Tiribocchi, J. Stenhammar, et al. „Scalar  $\varphi^4$  field theory for active-particle phase separation“. In: *Nature communications* 5 (2014), p. 4351. DOI: 10.1038/ncomms5351 (cit. on pp. 5, 37).
- [167]A. Wysocki, R. G. Winkler, and G. Gompper. „Cooperative motion of active Brownian spheres in three-dimensional dense suspensions“. In: *EPL (Europhysics Letters)* 105.4 (2014), p. 48004. DOI: 10.1209/0295-5075/105/48004 (cit. on pp. 4, 21, 26, 45, 52).
- [168]C. N. Yang. „The spontaneous magnetization of a two-dimensional Ising model“. In: *Physical Review* 85.5 (1952), p. 808. DOI: 10.1103/PhysRev.85.808 (cit. on p. 15).
- [169]X. Yang, M. L. Manning, and M. C. Marchetti. „Aggregation and segregation of confined active particles“. In: *Soft matter* 10.34 (2014), pp. 6477–6484. DOI: 10.1039/c4sm00927d (cit. on pp. 5, 37, 39, 42–44).
- [170]Y. Yang, V. Marceau, and G. Gompper. „Swarm behavior of self-propelled rods and swimming flagella“. In: *Phys. Rev. E* 82.3 (2010), p. 031904. DOI: 10.1103/physreve.82.031904 (cit. on p. 45).
- [171]H. P. Zhang, A. Be'er, E.-L. Florin, and H. L. Swinney. „Collective motion and density fluctuations in bacterial colonies“. In: *Proceedings of the National Academy of Sciences* 107.31 (2010), 13626–13630. DOI: 10.1073/pnas.1001651107 (cit. on p. 1).
- [172]J. A. Zollweg and G. W. Mulholland. „On the law of the rectilinear diameter“. In: *The Journal of Chemical Physics* 57.3 (1972), pp. 1021–1025. DOI: 10.1063/1.1678352 (cit. on p. 36).
- [173]A. Zöttl and H. Stark. „Hydrodynamics Determines Collective Motion and Phase Behavior of Active Colloids in Quasi-Two-Dimensional Confinement“. In: *Physical Review Letters* 112.11 (2014), p. 118101. DOI: 10.1103/physrevlett.112.118101 (cit. on p. 4).



## Colophon

This thesis was typeset with  $\text{\LaTeX}2_{\epsilon}$ . It uses the *Clean Thesis* style developed by Ricardo Langner. The design of the *Clean Thesis* style is inspired by user guide documents from Apple Inc.

Download the *Clean Thesis* style at <http://cleanthesis.der-ric.de/>.





